Palaeomagnetic Estimation of Pyroclastic Flow Deposit Emplacement Temperatures at Volcán de Colima, Mexico

Shoshana Weider
Worcester College

4th-Year Research Project
Department of Earth Sciences
Trinity Term, 2007

ABSTRACT

Volcán de Colima is an active volcano that makes up part of the Colima Volcanic Complex, in the western Trans-Mexican Volcanic Belt. Pyroclastic deposits formed from eruptions in July 2005, which made up part of the ongoing current cycle of activity that began in 1997. Lithic clasts were sampled from 11 sites within these deposits. Step-wise thermal demagnetisation was carried out on a selection of these clasts from each site in order to calculate their temperatures of emplacement. High-temperature susceptibility and IRM analyses were undertaken on a number of samples in order to identify the major magnetic-remanence carrying minerals in the clasts, and to help constrain the emplacement temperatures in some cases where non-ideal behaviour was exhibited in the demagnetisation procedure. Sensible equilibrium temperatures for each site are acquired (190°C to 340°C) that fall within the expected range, however the associated directions of the low- and high-T_B components of magnetic remanence do not meet the criteria required by the methodology. Various aspects of pyroclastic flow dynamics are discussed in the context of their evolving temperatures, and possible reasons for the peculiar remanence directions are suggested.

DECLARATION / WORD COUNT

I declare that this work is entirely my own with all references cited as appropriate.

………………………………………………….. Date: ………………………..

The total word count for this project is 7,991. This figure excludes the abstract, headings, figure captions, tables, acknowledgements, references and appendices.

CONTENTS

1. INTRODUCTION

The history of volcanology is a long one, extending back to the report of Plinius the Younger who witnessed the famous eruption of Vesuvius in 79 AD. This study uses rock magnetic theory to enhance the understanding of volcanoes, their mechanics, and their deposits. By analysing the different components of thermomagnetic remanence in lithic clasts of pyroclastic rocks, the emplacement temperatures of those deposits can be estimated. Being able to calculate the emplacement temperatures of deposits from explosive volcanic eruptions is important in assessing the risks posed to people living in dangerous regions. So immense are the velocity and energy involved in pyroclastic flows, that they will always pose serious risks to human activities, but depending on external factors (such as atmospheric conditions, and the amount of water) their actual temperatures will vary, and the specific hazards will evolve. For example: the ignition temperature of wood is 246°C (Macdonald, 1972); if a pyroclastic flow is hotter than this, trees and wooden objects along its path should be set alight, with the potential to cause large fires in inhabited areas.

There are two main reasons for predicting the activity of volcanoes: first of all it is desirable to know the products which will be erupted over different time scales and the effects these will have over the surrounding areas, this is known as *general prediction* and is defined as the study of "the past behaviour record of a volcano so as to determine the frequency, magnitude and style of eruptions, and to delineate high risk areas" (Walker, 1974). This style of prediction normally includes the production of a hazard map and can also be utilised for planning purposes (eg development of evacuation procedures, or civil-defence measures). The second type of prediction is known as *specific prediction* and is based on observations of the volcano and monitoring its changes (eg in seismic activity or tilt), so as to forecast the time, place and magnitude of an eruption. Volcán de Colima lies about 30 km northeast of the city of Colima (population ~125,000). This is outside the extent of recent pyroclastic flows (radius of about 12km), but there are smaller towns within, or close to this limit (a total of about

1

30,000 live within 40km of the volcano). Conclusions drawn from this work should be useful in making general predictions for Volcán de Colima, but also provide complementary data for making specific predictions.

2. BACKGROUND

2.1 Geology of Volcán de Colima

Volcán de Colima (also known as Volcán de Fuego or Fuego de Colima) is an active stratovolcano lying in the western part of the Trans-Mexican Volcanic Belt (TMVB), which is a calc-alkaline continental volcanic arc that runs almost 1000km across the centre of Mexico (Figure 2A). It contains at least eleven large volcanic centres that have been active for about 20,000 years. The western section of the TMVB has been created by the subduction of the Cocos and Rivera (oceanic) plates beneath the North American Plate (continental); a situation that has been active since the Pliocene (Figure 1). The western TMVB consists of three regional structures: the Colima Graben, the Zacoalco right lateral fault zone, and the Chapala Graben (known collectively as CZC) (Luhr *et al*. 1985). The Colima Graben is the southern arm of the CZC triple junction; it is bordered to the north by north-south running normal faults, and to the south by the Pacific coast. The superposition of the two tectonic regimes (subduction of the Rivera Plate and rifting along the Colima Graben) has generated coeval alkaline and calc-alkaline volcanism since 4.6Ma (Allan, 1986).

Within the Colima Graben is the andesitic Volcán de Colima complex (CVC). It consists of several composite cones which have been active since about 1.5Ma. The locus of volcanism has shifted southwards over time, building (from north to south) Cantaro Volcano (2900m), Nevado de Colima (4240m), and the active Volcán de Colima (3860m) (Figure 2B). Volcán de Colima was built in the late Pleistocene on the southern slopes of Nevado de Colima. This volcano is the most active in Mexico in historic times (more than 43 eruptions since 1576) and is one of the most active in North

2

America (at least 25 explosive eruptions in last 427 years) (Luhr, 1981; Medina *et al.*, 1983; De la Cruz-Reyna, 1993). (Table 1)
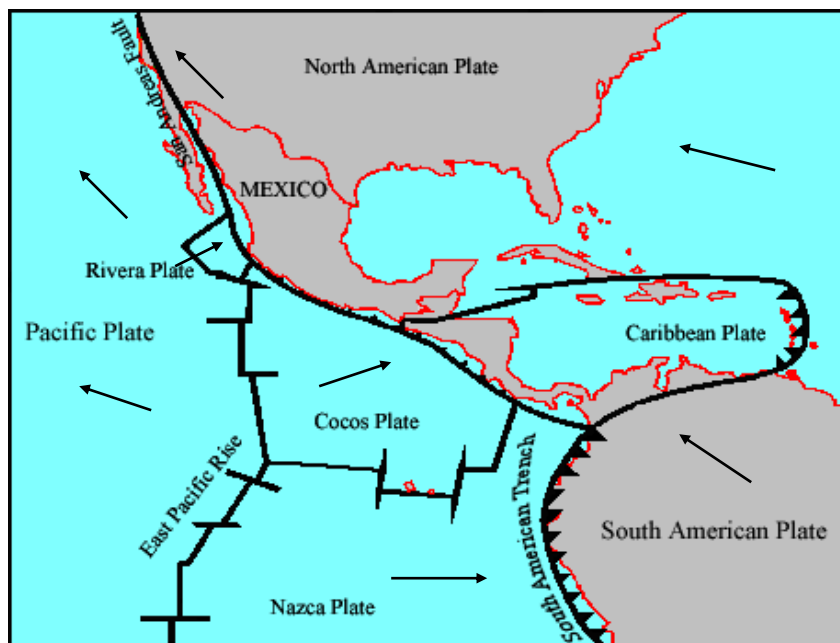
Figure 1: Map showing the tectonic plates of the region.

(http://mceer.buffalo.edu/publications/bulletin/96/10-01/jan96f1.html)
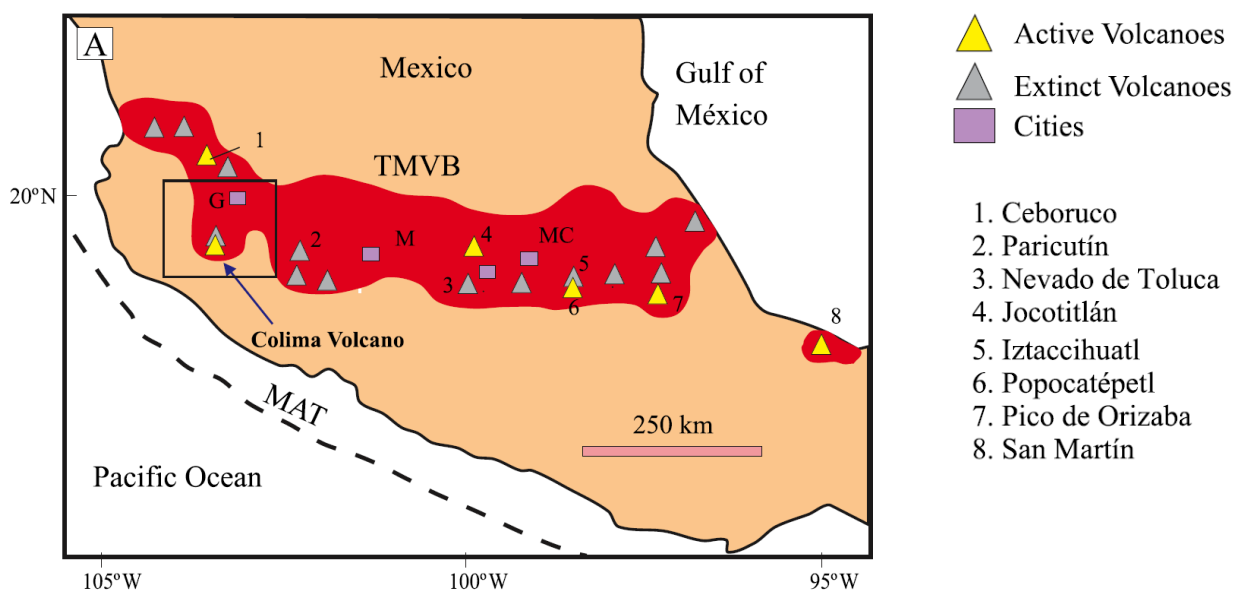

Figure 2A: Location of Volcán de Colima in the western portion of the Trans-Mexican Volcanic Belt. (MC=Mexico City, T=Toluca, G=Guadalajara, M=Morelia, MAT=Middle American Trench.
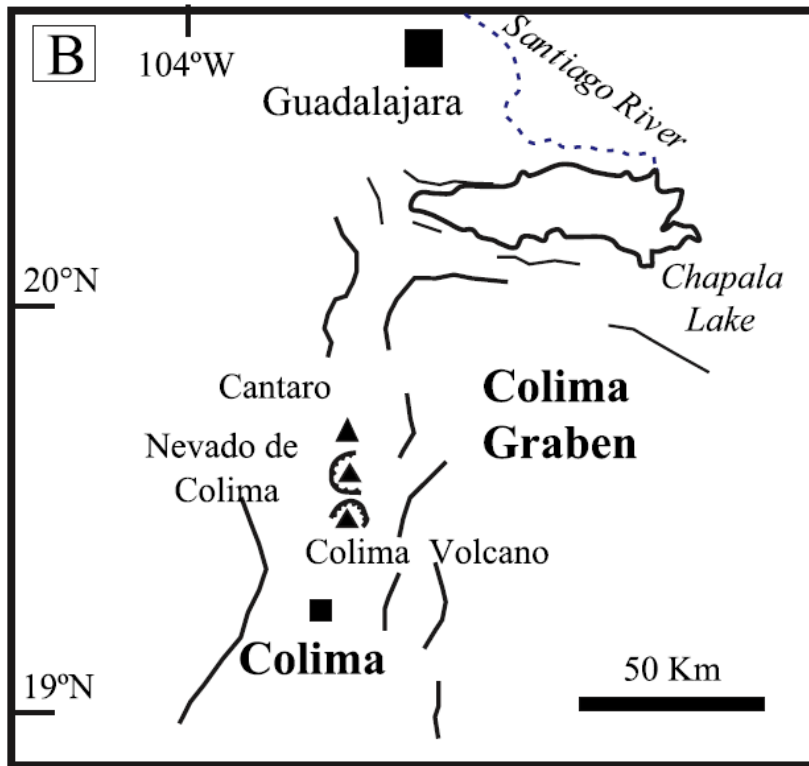
Figure 2B: Sketch map of the Colima Graben showing the location of the Canataro, Nevado de Colima and Volcán de Colima volcanoes. (Saucedo et al., 2005).

2.2 History of eruptions at Volcán de Colima

The volcanic products of Volcán de Colima can be grouped into four eruptive cycles, each beginning with the formation of a lava dome and ending with a major pyroclastic eruption. The last two cycles are broadly similar, both lasting about a century (Luhr & Carmichael, 1980; 1990). The third cycle (1818 – 1913) was characterised by several different eruption styles, ending with an event that produced pyroclastic flows and a 21km-high Plinian eruptive column that deposited fine ash as far as 725km to the northeast (Luhr & Carmichael, 1990; Saucedo et al., 1997). The current cycle of activity began with lava emissions (1961 – 1962) and continued with lava eruptions in 1975 – 1976, 1981 – 1982, and 1991. The most recent unrest began in November 1997 with a sharp decrease in seismic activity, it continues to the present day.

YEAR	ERUPTION TYPE	REFERENCES	OBSERVATIONS
1576	Possibly Plinian	Bárcena (1887)	Generation of block-and-ash flows (bafs).
1590	Explosion	Waitz (1935)	Important area covered by ash fall and likely generation of Soufrière-type bafs.
1606	Possibly Plinian	Tello (1651); Arreola (1915)	The ash fall reached to Michoacan State and possible generation of Soufrière-type bafs.
1611	Explosion	Bárcena (1887)	Important area was covered for ash fall and Soufrière-type bafs.
1690	Possibly Plinian	Luhr & Carmichael(1990)	Possible generation of bafs.
1771	Explosion	Bárcena (1887)	The ash fall reached the City of Guadalajara and possible generation of Soufrière-type bafs.
1818	Plinian	Sartorious (1869); Bárcena (1887); Arreola (1915)	Bafs and ash fall that reach Mexico City.
1869-1872	Adventitious cone	Bárcena (1887)	Lava flow and Merapi-type bafs accompanied by ash fall.
1880	Lava flow & Merapi-type bafs	Kerber 1882	Lava flows and Merapi-type bafs on the SW flank.
1885-1886	Lava flow on the flank SW-W	Bárcena (1887)	Lava flow and Merapi-type bafs.
1885-1886	Explosion	Bárcena (1887)	Soufrière-type bafs?
1890	Explosion	Arreola (1915)	The ash fall reached the City of Guanajuato and likely produced Soufrière-type bafs.
1891-1892	Explosion	De la Cruz-Reyna (1993)	The ash fall reached the city of Colima and possible Soufrière-type bafs.
1903	Explosion	Arreola (1915); Waitz (1935)	Ash fall and Soufrière-type bafs.
1908	Explosion	Arreola (1915); Waitz (1935)	Ash fall and Soufrière-type bafs.
1909	Explosion	Arreola (1915); Waitz (1935)	Ash fall and Soufrière-type bafs.
1913	Plinian	Waitz (1915, 1935); Arreola (1915)	Merapi and Soufrière-types bafs derived from a Plinian column and ash fall that reached 725km toward NE.
1961-1962	Lava flow & Merapi-type bafs	Mooser (1961)	Merapi-type bafs on the southeast flank, runout 4.5km.
1975-1979	Lava flow & Merapi-type bafs	Thorpe et al. (1977)	Merapi-type bafs on the south flank, runout 1km.
1981-1982	Lava flow & Merapi-type bafs	Luhr & Carmichael(1991)	Merapi-type bafs on the north flank, runout 2km.
1987	Explosion	Luhr & Carmichael(1991)	Explosion crater and Soufrière-type bafs.
1991	Lava flow & Merapi-type bafs	Rodríguez-Elizarrarás et al. (1991); Saucedo (2001)	Merapi-type bafs, 4km runout and lava flow 2km runout on south-western flank.
1994	Explosion	Saucedo et al. (1995)	Soufrière-type bafs, 3.5km runout.
1998-1999	Three lava flows & Merapi and Soufrière-type bafs	Saucedo (2001)	Merapi-type bafs, 4.5km runout, Soufrière-type bafs, 3.3km runout and lava flow 3km runout.
2001	Explosion & Soufrière-type bafs	Gavilanes (2001)	Soufrière-type bafs, 2-3km runout.

Table 1: Summary of the historic reports and modern studies of volcanic activity at Volcán de Colima, Mexico (Saucedo et al., 2005).

The activity which led to the deposition of the pyroclastic flows sampled in this study (July 2005) was part of stage 4 in the cycle of activity (Figure 3). We await the termination of the cycle. Further insight into the future termination requires a better understanding of the degassing mechanisms beneath the volcano and the cause of the distinct behaviours of magmas with ~61% SiO_2 and those with ~58% SiO_2. This range marks a critical viscosity and ascent-rate threshold. Magmas erupted from Volcán de Colima with ~58% SiO_2 ascend rapidly through the upper crust without significant degassing and erupt explosively from the crater. In contrast, magmas with ~61% SiO_2 have higher viscosities and appear to rise much more slowly, so that they lose most of their volatiles before reaching the crater and erupt as block-lava flows (Luhr, 2002).
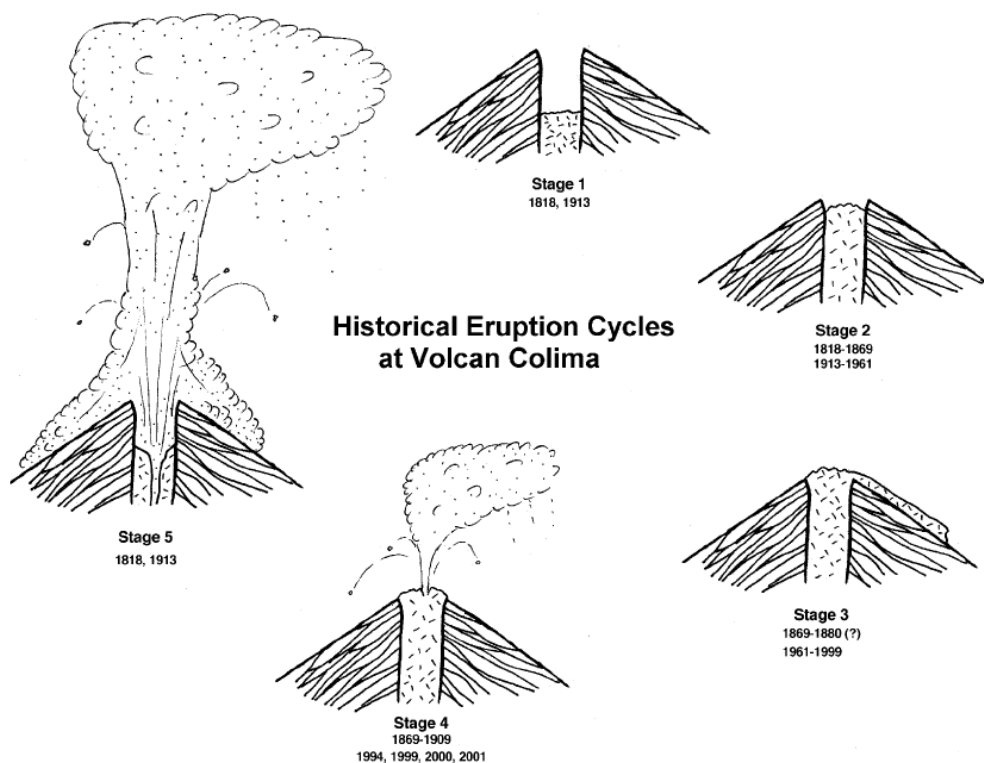

Figure 3:
A schematic depiction of the five major stages in the last two historical eruption cycles of Volcán de Colima. Stage 1: Open crater following cycle-ending explosive eruptions. Stage 2: Lava dome slowly ascends in open crater, probably through a combination of endogenous growth and extrusions on the crater floor. Stage 3: Crater dome reaches the rim (or magma leaks out a flank vent as in 1869) and block-lava flows down the upper flanks of the cone, sometimes reaching 3 – 4 km distance. Block-and-ash flows precede and accompany emplacement of lava flows. Stage 4: Intermittent minor-to-major explosive activity from the summit crater (or parasitic vent as in 1869) alternates with the stage-3 lava emissions. Stage 5: Major explosive eruptions terminate the cycle. These involve tephra falls that extend many hundreds of km downwind and local pyroclastic flows that reach beyond 10km from the vent, especially on the southern flanks. The crater is reamed out to leave an open cylinder (stage 1). (Luhr, 2002)

Start Date	Finish Date	Style of activity	Lava flows	Pyroclastic Flows	Plumes	Deposit Volume (m^3)	Notes
Feb 02	Feb 03	Effusive	Yes - 8	Yes		~8.3 x 10^6	Deposit volume includes lava dome and flows as well as pyroclastic flow and rockfall deposits.
May 03	July 03	Explosive		5 with runout distances <2km on WSW slopes.	**2 May**: small eruption. Ash cloud rose not higher than 500m above crater. **17 July**: more significant eruptions. Incandescent material reached 500m and ash column >3km.		Small forest fires 2.5–4km SW of crater.
2 Aug 03	2 Aug 03	Explosive			Altitude of ~7.6km.		
28 Aug 03	28 Aug 03	Explosive		Out to 2.5km.	Ash column at least 3km high.	~ 244,000	Ashfall up to 60km WNW of volcano. New crater (200m across, 30m deep) at summit.
12 Jun 04	12 Jun 04	Explosive			Column did not exceed 2km.		
28 Sept 04	28 Sept 04	Intensive fumarolic			500m high column of white gas.		
30 Sept 04	30 Sept 04	Effusive / explosive	Yes	Rockfalls and pyroclastic flows.			Swarm of seismic events indicated overflow of lava from crater and formation of two andesitic block-lava flows.
10 Mar 05	13 Mar 05	Explosive		Down S flank, lengths did not exceed 2.8km.	Eruptive columns with heights ~5km above crater.		Two discrete explosions on 10 & 13 Mar. Another relatively large explosion occurred on 26 Mar.
24 May 05	5 Jun 05	Explosive (Vulcanian)		Run out distances up to ~5.1km.	Gas and ash explosion, some material reached as high as altitude of ~10km.		Mar-Jun explosive sequence removed the 2004 lava dome and left a crater ~260m across & ~30m deep. (See Figures 6 & 7 and Table 3)
29 Jun 05	5 Jul 05	Explosive		**5 Jul**: travelled down E flank.	Several plumes rose to altitudes of 9-10km.		**30 Jun**: lahars travelled SW down La Lumbre Ravine and SSE down Montegrande Ravine (max. length ~10km).
6 Jul 05	19 Jul 05	Explosive					Several explosions triggered small landslides down flanks of volcano.
21 Jul 05	21 Jul 05	Explosive					Small ash emissions and lahar travelled SSE down Monte Grande Ravine. Ash emissions and lahars also occurred on 23 Jul.

Table 2: Summary of the eruptive characteristics of Volcán de Colima between February 2002 and July 2005

(http://www.volcano.si.edu/world/volcano.cfm?vnum=1401-04=&volpage=var&VErupt=Y&VRep=Y&VSources=Y&VVWeekly=Y#bgvn_3103)

Figure 4: A typical view of a small explosion at Colima (1st February 2004). Courtesy of Colima Volcano Observatory.

Figure 5: A view of Volcán de Colima's crater floor from the south (27th February 2004). Courtesy of Colima Volcano Observatory.

Figure 6: The crater of Volcán de Colima filled nearly to the rim with considerable dome and unconsolidated material (25th May 2005). Courtesy of Colima Volcano Observatory.

Figure 7: Crater of Volcán de Colima after the comparatively large explosions that began in March 2005 (16th June 2005, from the south). The eruptions removed much of the crater fill and a small dome from the upper crater, but the crater walls are still intact and without evidence of fractures. Courtesy of Colima Volcano Observatory

9

DATE OF EXPLOSION	ALTITUDE OF COLUMN (km)	DIRECTION & AVERAGE HORIZONTAL VELOCITY OF ASH CLOUD	LENGTH OF ASH CLOUD (km)	LENGTH OF PYROCLASTIC FLOWS (km)
24 May 2005	9.7	W (7.7 m/s)	204	3.5
30 May 2005	8.5	SE (15 m/s)	102	4
02 June 2005	6.0	S (5.1 m/s)	74	4.5
05 June 2005	7.6	W-SE (7.7 m/s)	222	5.1

Table 3: Main characteristics of the largest explosions at Volcán de Colima during May-June 2005. Column heights and ash cloud velocities come from remote-sensing data and reports of the Washington VAAC. Courtesy of Colima Volcano Observatory.

2.3 Pyroclastic flows

Volcanism is most common where oceanic lithosphere is subducted beneath continental lithosphere (as is the case at the TMVB). Such volcanic arcs are made up of lava flows and pyroclastic debris. The rocks normally have compositions within the andesite suite (basalt-andesite-dacite-rhyolite) and are more abundant as pyroclastic deposits than as lava flows.

Pyroclastic density currents are rapidly moving mixtures of hot volcanic particles and gas, with or without free water, they flow across the ground under the influence of gravity (Druitt, 1998). They may form by the gravitational collapse of lava domes, by fallback or continuous fountaining of vertical eruption columns; or by lateral blasts. Based on the textural characteristics of their deposits, two end-members are recognised: pyroclastic surges and pyroclastic flows (Fisher & Schmincke 1984; Cas & Wright 1987). The latter type concerns us in this study.

During explosive volcanic eruptions Plinian columns may form if the pressure and density conditions are correct. The erupted material has a high temperature and so it rises through the atmosphere as a jet (leaving the vent at $100 - 500$ ms^{-1}), entraining the ambient air in the process. A buoyant plume will be maintained until the density of the plume is more than that of the surrounding atmosphere. If

the mixture is denser than air when the jet's velocity falls to 0, the plume will collapse and form density currents.   This is known as column collapse, it creates expanded, but density-stratified currents, in which particles are suspended by turbulence. Pyroclastic flows that are formed by column collapse are rich in vesicular components.

During such explosive volcanic eruptions the pyroclastic mixture of lava and gas exits the vent at high velocities and with high levels of energy. As the eruption proceeds, material from the conduit walls, or the existing edifice is ripped away and incorporated into the fast moving flow. The deposits formed by this process are made of the solid fragments torn from the vent walls, known as accidental or lithic clasts, and fragments of new lava (juvenile magmatic material) that are erupted while still molten.

Deposits from pyroclastic flows which are associated with calc-alkaline stratovolcanoes typically have small volumes ($<1km^3$), with basaltic, andesitic, or dacitic compositions. The runout distances typically range from a few hundred metres to a few kilometres. The deposits tend to be poorly sorted, massive and thicken markedly into depressions.

Studies such as this one can provide some real clues for the origin of volcanic deposits. Pyroclastic flows, lahars, rock avalanches and glaciers on stratovolcanoes can often produce strikingly similar surficial deposits of unstratified, unsorted volcanic rock debris.   Rock avalanches and glaciers emplace deposits at or near ambient temperatures; pyroclastic flows always emplace debris at temperatures which are significantly above ambient; and lahars may emplace debris at ambient or significantly higher temperatures.

The term lahar (Indonesian for volcanic breccia transported by water) (van Bemmelen, 1949) has

become synonymous with that of volcanic debris flow, a mass of flowing volcanic debris intimately mixed with water. Macdonald (1972) proposed ten different ways that lahars can originate and these can be further grouped into three categories (Crandell, 1971):

1) Direct and immediate result of eruptions: eruptions through lakes, snow or ice; heavy rains falling during or immediately after an eruption; flowage of pyroclastic flows into rivers, or onto snow or ice.

2) Indirectly related to an eruption or occur shortly after an eruption: triggering of lahars by earthquake or expansion of a volcano causing the rapid drainage of lakes or the avalanching of loose debris or altered rock.

3) Not related in any way to contemporaneous volcanic activity: mobilization of loose tephra by heavy rain or meltwater; collapse of unstable slopes; bursting of dams due to overloading; lahars that originate on the steep slopes of volcanoes of other volcanic terranes undergoing active weathering and erosion; sudden collapse of frozen ground during the spring thaw.

During the 2005 eruptions of Volcán de Colima (whose deposits were sampled in this study) lahars were observed flowing down the southern flanks of the volcano. If these lahars formed due to the interaction of pyroclastic flows with water and were emplaced with significantly higher than ambient temperatures, the palaeomagnetic analysis of their magnetic remanence may be unable to distinguish such deposits with others of pure pyroclastic origin.

2.4 Palaeomagnetic theory

2.4.1 Origins of magnetic behaviour

Faraday's Law of Induction links the phenomena of electric and magnetic fields. Movement of any electrically charged particle produces a magnetic field in a perpendicular direction to the motion of the particle (the current) (Figure 8).
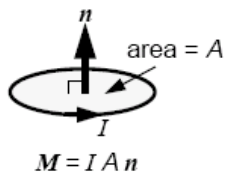
Figure 8: A magnetic dipole constructed from a circular loop of electrical current. The magnetic moment is M, the electrical current is *I*; the area of the loop is *A*; the unit normal vector *n* is perpendicular to the plane of the loop. (Butler, 1992)

It is the spin of electrons that gives rise to the magnetic field. Up (↑) electrons have a spin of +½ and down (↓) electrons have a spin of - ½. These individual spins sum within any atom, therefore atoms with full outer-electron shells have total spins of 0. Atoms with unpaired electrons (such as the transition metals, with their unfilled 3d orbitals) have total spins that do not equal 0, giving rise to a spin angular momentum. When materials contain atoms with spin angular momentums (eg minerals containing iron or titanium) they can display magnetic behaviour. The net magnetic moment of an atom (*J*) is the sum of its orbital angular momentum and its spin angular momentum, the latter being dominant. When $J = 0$ an atom is non-magnetic and when $J \neq 0$ an atom is magnetic.

All materials, when placed within in an applied magnetic field, are acted on by an aligning torque which causes the electron orbits to rotate and become parallel or anti-parallel to the field. There are three possible responses, dependent on the susceptibility (the ease with which the material is magnetised): paramagnetism, diamagnetism and ferro/ferrimagnetism (Figure 9).
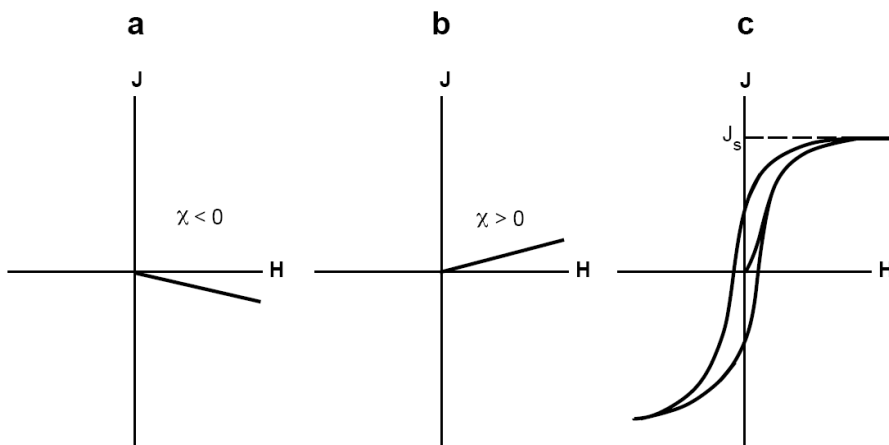

Figure 9: Magnetisation, *J*, versus magnetising field, *H*, for (a) a diamagnetic substance; (b) a paramagnetic substance; (c) a ferromagnetic substance. J_S is the saturation magnetisation. (Butler, 1992)

Paramagnetism: susceptibility (χ) is positive. Magnetism (***J***) is induced parallel to the applied field. There is no interaction between adjacent magnetic moments and so ***J*** decays to 0 when the field is removed.

Diamagnetism: χ is negative. ***J*** is induced in the opposite position to the applied field and decays to 0 when the field is removed. This is 10 - 100 times weaker than the paramagnetic response and is a property of all matter, but it is completely dominated in materials with atomic magnetic moments.

Ferromagnetism: χ is not linear. This is a property of solids where the atomic magnetic moments interact strongly. The overlapping of adjacent orbitals (more eccentric orbitals extend further from the nucleus) causes strong parallel coupling of electron spins and gives rise to permanent magnetisation. The general term *ferromagnetism* applies to all solids with such coupling of atomic magnetic moments, but it strictly applies to solids with **parallel** coupling of adjacent atomic magnetic moments. If layers have equal magnetic moments, opposing layers will cancel and ***J*** = 0 (antiferromagnetic behaviour). If the layers have unequal magnetic moments and are anti-parallel, ***J*** will point in the direction of the dominant layer (ferrimagnetic behaviour). Many of the important magnetic minerals are ferrimagnetic (Figure 10).
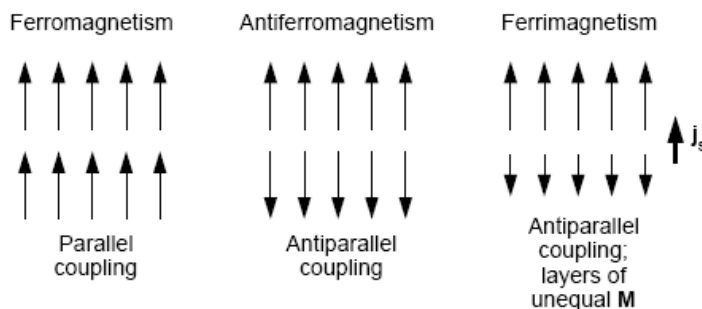

Figure 10: Exchange coupling for ferromagnetic, antiferromagnetic and ferrimagnetic materials. j_s is the net magnetisation for the ferrimagnetic material. The net magnetisation of the antiferromagnetic material is 0. (Butler, 1992)

When a ferromagnetic material is removed from an applied magnetic field the magnetisation is retained, this is known as a remanent magnetisation. The maximum magnetisation or saturation

magnetisation (J_S) of a material decreases with temperature and becomes zero at its Curie temperature (T_C). At this point the material can display only paramagnetic behaviour. Each material has its own characteristic T_C.

2.4.2 Magnetic domains

Magnetic charges of adjacent atoms cancel within a particle, but create a magnetic charge distribution at the surface of the particle (Figure 11a). The repulsion of like charges on adjacent atoms creates a magnetostatic energy. A state where this energy is minimised, is favoured and sought by the magnetic grains in a rock. This energy can sometimes be reduced by the formation of magnetic domains within a single grain. In such a case, the proportion of the surface covered by magnetic charges is smaller, and charges of opposite polarity are adjacent rather than separated, as would happen if the particle were single domain. Each domain has its own magnetisation, but for the entire grain the net magnetisation is less than that of any one of its constituent domains (Figure 11b).
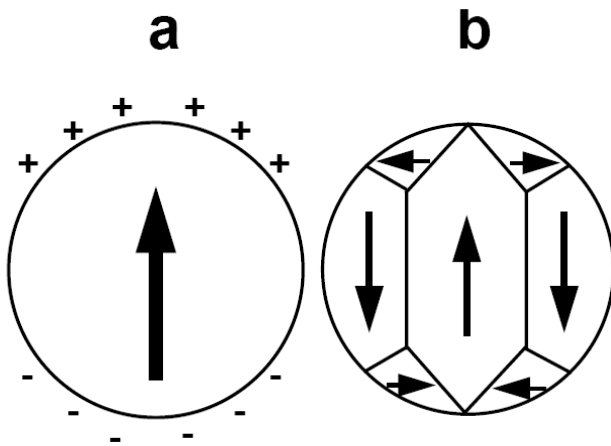

Figure 11:

(a) Uniformly magnetised sphere of ferromagnetic material. The direction of J_S is shown by the arrow; surface magnetic charges are shown by + and – signs.

(b) Sphere of ferromagnetic material subdivided into magnetic domains. Arrows show the directions of j_s within individual magnetic domains; planes separating adjacent magnetic domains are domain walls. (Butler, 1992)

The number of magnetic domains is dependent on the size and shape of the grain (Figure 12). At some threshold size, the energy required to make a domain wall (separates adjacent domains) is greater than the decrease in energy that results from the creation of domains, and so the grain will be single-domain (SD). The magnetic properties of SD grains are different to those of multi-domain (MD) grains.

Thermal activation of a grain can cause energy barriers to be broken and J_S may rotate to align with a new magnetising field. If the new field is removed, J_S decays with time to reach equilibrium with the ambient field. This period is the relaxation time (τ) and is dependent on the volume of the grain, the coercivity (magnetic field required to reduce J to 0), J_S, and temperature (Figure 13).

SD grains with short relaxation times are superparamagnetic (SP), such grains have strong ferromagnetic magnetisations. Good palaeomagnetic recorders must have suitable relaxation timescales (Figure 12). The temperature (affects τ) at which a grain changes from being superparamagnetic to stable SD is the blocking temperature (T_B). Between the T_C and the T_B a grain will be ferromagnetic, but the remanent magnetisation will be short lived. Remanent magnetism acquired at or below T_B is stable. Rocks contain a range of ferromagnetic grain sizes and shapes that give rise to spectra of T_B between ambient and Curie temperatures.
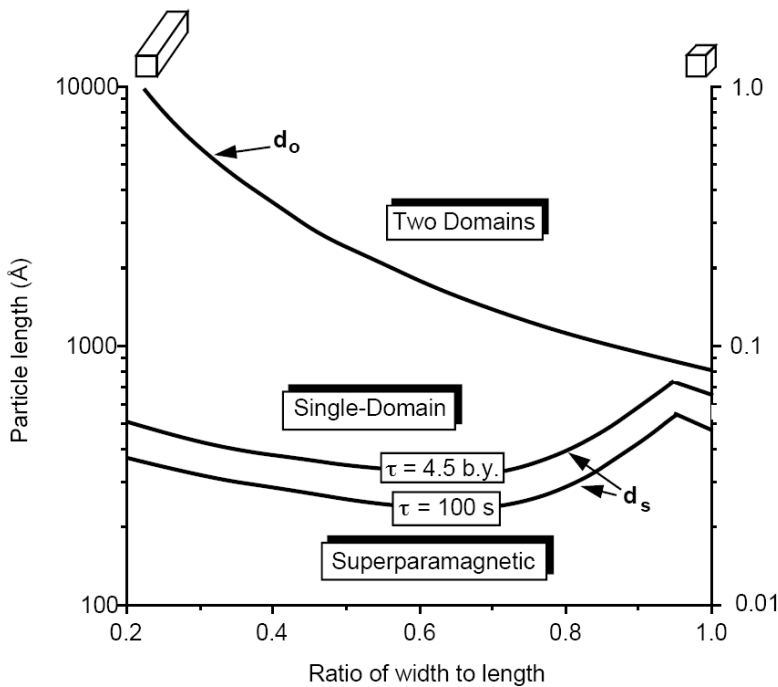

Figure 12: Size and shape ranges of single-domain, superparamagnetic, and two-domain configurations for parallelepipeds of magnetite at 290°K. Particle shape is indicated by the ratio of width to length; the curve labelled d_0 separates the single-domain size and shape field from the size and shape distribution of grains that contain two domains; curves labelled d_S are size and shape distribution of grains that have τ = 4.5 b.y and τ = 100s; grains with sizes below d_S curves are superparamagnetic. (Butler, 1992)

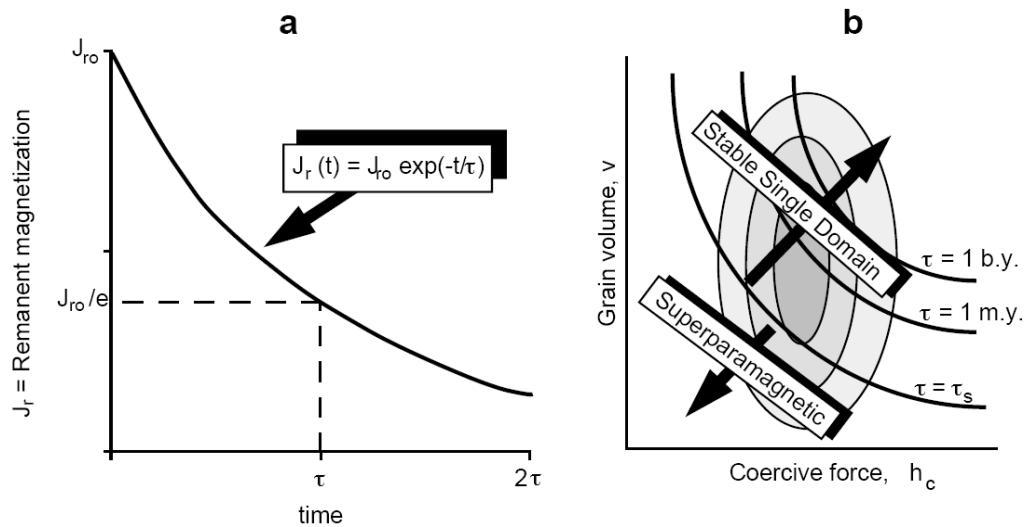**Figure 13: (a) Magnetic relaxation in an assemblage of SD ferromagnetic grains. Initial magnetisation J_{ro} decays to J_{ro}/e in time τ. (b) Relaxation times of SD grains on diagram plotting SD grain volume, v, against SD grain microscopic coercive force, h_C (τ_s = short relaxation time). (Butler, 1992)**

2.4.3 NRM

The natural remanent magnetisation (NRM) of a rock is that which is present before any laboratory work is undertaken. It is gained during rock formation and any subsequent activity that may have changed the physical properties of the rock (such as changes in temperature, mineralogy, grain size distribution, grain alignment). It can have more than one component, illustrative of its various stages of development. The primary NRM is acquired during initial rock formation, any subsequent components are referred to as secondary NRM (these may obscure the primary signal). All components of NRM add vectorially. The three most common types of NRM are thermoremanent magnetisation (TRM), chemical remanent magnetisation (CRM) and detrital remanent magnetisation (DRM).

When a rock containing ferromagnetic minerals cools from above their T_C, in the presence of a magnetic field (eg the geomagnetic field), the grains of the magnetic minerals will record and 'lock in' the direction and intensity of the field at the moment when the temperature falls below T_C. This is the

17

TRM. CRM arises from changes to the mineralogy of the ferromagnetic minerals in a rock. Alteration can cause precipitation of a new magnetic phase, or cause the loss of an existing one. This is most commonly encountered in sedimentary rocks. DRM is acquired during deposition and lithification of sedimentary rocks, caused by the magnetic minerals gaining alignment from external physical forces. In this study TRM is the component of NRM that is of most interest.

2.5 IRM

An isothermal remanent magnetisation (IRM) is that produced at constant temperature over short timescales from exposure to a strong magnetising field. They can be both natural and laboratory-induced. The latter is usually imparted to a sample by exposure to an electromagnet-generated magnetising field. The IRM is acquired by ferromagnetic grains whose coercive force is smaller than the applied field.

2.6 Emplacement temperature determination

The emplacement temperatures of pyroclastic deposits were first estimated using thermomagnetic techniques by Aramaki & Akimoto (1957). Subsequent studies have developed the understanding and refined this procedure. When lithic clasts contained in pyroclastic deposits originally form (by cooling of magma) they acquire a TRM that records the intensity and direction of the Earth's magnetic field at the time. After being incorporated into a pyroclastic flow they are considerably displaced and re-deposited in new, random orientations. Three possible situations may arise (McClelland & Druitt 1989):

1. The emplacement temperature (T_{empl}) of the deposit is greater than the T_C of the major magnetic carrier in the clast. Ferromagnetic grains have uniformly oriented remanence parallel to the ambient field direction at the time of deposition.

2. T_{empl} of the deposit is the same as the ambient temperature. Ferromagnetic grains retain their

18

original remanence, which appears as a randomly oriented direction.

3. T_{empl} of the deposit is less than T_C of the major remanence carrier in the clast (but above the ambient temperature). Ferromagnetic grains with $T_B > T_{empl}$ retain their original remanence (with random directions) and grains with $T_B < T_{empl}$ remagnetise and acquire a TRM with the ambient field direction. The upper limit of the low-T_B component provides an estimate of the clast's emplacement temperature.

Thermal demagnetisation involves heating rock specimens to temperatures (T_{demag}) below T_C of their constituent ferromagnetic minerals, and then cooling to room temperature in the presence of 0 magnetic field. All grains that have $T_B \leq T_{demag}$ will acquire a new TRM ($\mathbf{H} = 0$) which erases the NRM carried by those grains. The intensity and direction (inclination and declination) of the NRM are measured after each heating step. By heating to progressively higher and higher temperatures the different components of NRM carried by grains of different coercivities and blocking temperatures are revealed.

3. METHODOLOGY

Field work was conducted in August 2006 by Dr Conall Mac Niocaill, Dr Adrian Muxworthy and Mr Grieg Paterson. Ten or eleven lithic clasts of cm-size (113 clasts in total) were collected from eleven sites (sites 1 and 2 were at the same locality) within the July 2005 deposits (coordinates of the sites are shown in Table 4). The strike and dip of each clast was measured using a sun compass, marked clearly and recorded along with its depth within the deposit.

SITE NUMBER	N COORDINATE	W COORDINATE	ALTITUDE (m)	RELATIVE POSITION	FIELD NOTES
1	19° 28' 77.4"	103° 37' 52.3"	2305		Roots do not look very burnt.
2	19° 28' 77.4"	103° 37' 52.3"	2305		
3	19° 28' 73.6"	103° 37' 53.4"	2297	South from site 1 & 2	Uppermost part of July 2005 flows.
4	19° 28' 88.7"	103° 37' 44.9"	2345	North from site 1 & 2	Blackened tree stump. Some hints of stratification.
5	19° 29' 13.8"	103° 34' 43.8"	1833		
6	19° 29' 15.9"	103° 34' 45.8"	1854		
7	19° 29' 16.3"	103° 34' 48.5"	1852	80m up canyon from site 6	
8	19° 29' 07.9"	103° 39' 70.6"	1786	In Zarco River valley	Deposit about 3m thick. Predominantly coarse granules with lithic clasts. Does not appear particularly hot.
9	19° 29' 02.3"	103° 39' 74.5"	1791	~100m down river valley from site 8	
10	19° 28' 98.0"	103° 39' 76.1"	1820	~150m down valley from site 9	
11	19° 28' 68.5"	103° 39' 93.4"	1840	Further along river valley from site 10	

Table 4: Summary of field notes. Sites 1 – 4: deposit is ~8m thick, consists of coarse ash granules with lithics and is confined to a canyon. It had a measured temperature of >200°C one week after the eruption in July 2005 (south from vent). Sites 5 – 7 had measured temperatures of >300°C one week after eruption (south east from vent). Sites 8 – 11: The deposit is about 3m thick in the Zarco river valley (south west from vent). See Appendix A for field sketches and photographs.

In Oxford each clast was set in plaster so that its orientation marks were horizontal and flat. 19mm cores were drilled vertically so that core lengths were perpendicular to the marked strikes and dips. Each core was named firstly according to its site number, then clast. When multiple cores from a clast were obtained they have an additional number, some longer cores were cut into two halves (indicated by a final letter). For example: VC4B2A is one half of the second core taken from clast B of site 4.

A total of 112 cores were selected to undergo stepwise thermal demagnetisation. The NRM of each sample was measured using the 2G Longcore Cryogenic magnetometer in the "field-free" (double-layer transformer steel) room of the palaeomagnetic laboratory in Oxford, which has an internal field of less than 200nT. Two measurement runs were made:

1. Measurements were made at 50°C intervals (up to 600°C) on sixty-four samples from sites 1 - 11. Two thermal demagnetising furnaces (MMTD60 and MMTD18) were used.

2. Forty-eight samples from sites 1 - 11 were measured. Measurements were made at 50°C and 100°C and then at 30°C intervals up until 500°C, where 50°C intervals were reinstated until the samples were demagnetised (to 600°C or 650°C). Both furnaces were used.

High-temperature susceptibility measurements were carried out on powders from selected clasts on a KLY2 Kappabridge.

A group of eight samples (VC1K1, VC3A2, VC3K4A, VC4B3B, VC4D1, VC5A6, VC9D3A, VC11A2) were selected to undergo laboratory acquisition and demagnetisation of IRM in order to help confirm the nature of the major ferromagnetic minerals in the clasts. The samples were first demagnetised at a field of 100mT using a DTECH D2000 AF Demagnetiser. They were then exposed to an applied field in a Pulse Magnetiser in steps up to a maximum applied field of 800mT. After each step their magnetisation was measured in a Molspin Spinner magnetometer. The steps were

repeated in a reverse field of the same magnitude.

4. RESULTS

4.1. TRM Analysis

Thermal demagnetisation results were analysed using the Super IAPD2000 program (Torsvik *et al.*, 2000), which uses the LINEFIND algorithm (Kent *et al.*, 1983). For each measured sample, lines of best-fit were manually sought for each individual Zijderveld diagram ("z-plot"). These diagrams display directional and intensity information on a single diagram by projecting the vector onto two orthogonal planes (Zijderveld, 1967). Inclinations are represented by open squares; declinations by closed squares (Figures 14 – 22). Satisfactory lines must have a mean angular deviation (MAD) that does not exceed 15.

Four different "types" of behaviour are identified from the z-plots:

Type 1: one component of magnetisation is identified (VC2E2: Figure 14). T_{empl} must have been hotter than the T_C of the main remanence carrier in the clast (one sample).

Type 2: two components are identified. One is the low-T_B component and one the high-T_B component of TRM (eg VC5K2, VC6F, VC8G2, VC8L: Figures 15 - 18). The upper limit of the low-T_B component provides an estimate of the T_{empl} of the clast (seventy samples).

Type 3: two components, as for type 2, are identified, but the high-T_B component is noisy (the MAD lies above the acceptable level) (eg VC3K5A: Figure 19). T_{empl} can be constrained as above the highest point of the low-T_B component (seventeen samples).

Type 4: two components, as for type 2, are identified, but the low-T_B component is noisy (the MAD lies above the acceptable level) (eg VC3H2 & VC6C: Figures 20 & 21). The T_{empl} can be constrained as below the lowest point of the high-T_B component (fifteen samples).

Nine samples (eg VC8D3: Figure 22) are magnetically stable until high temperatures, and so their components of remanence cannot be identified, they do not provide an estimate of their T_{empl}.
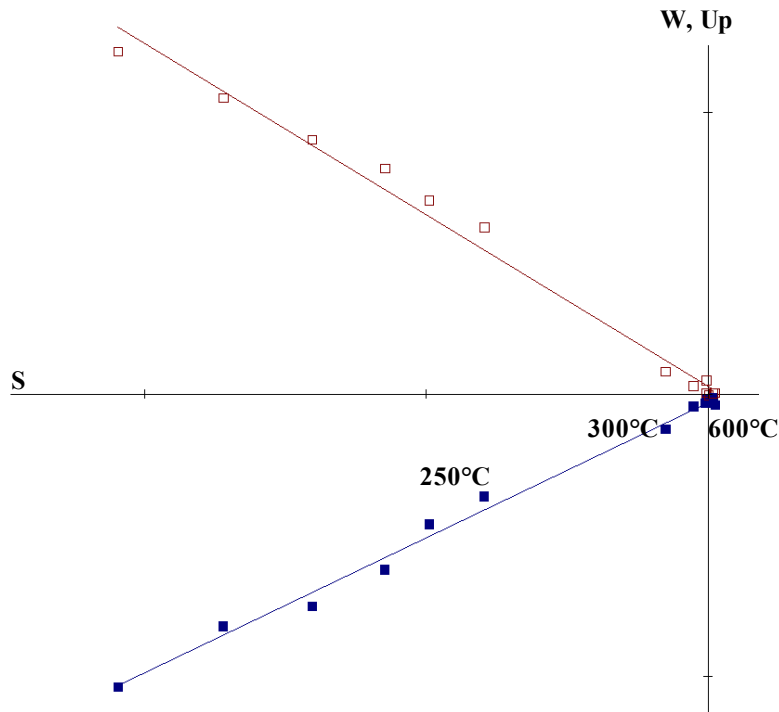

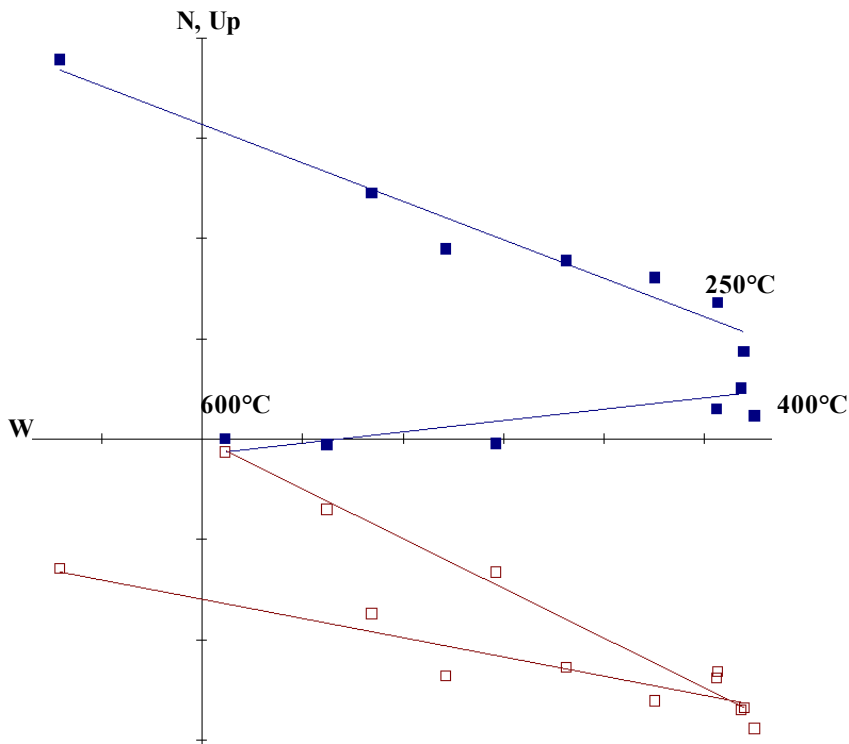**Figure 14: VC2E2 – type 1 behaviour. One component of magnetisation: SE, up.**

Figure 15: VC5K2 – type 2 behaviour. Two components of magnetisation: 1) high-T_B: E, down; 2) low-T_B: WNW, up.
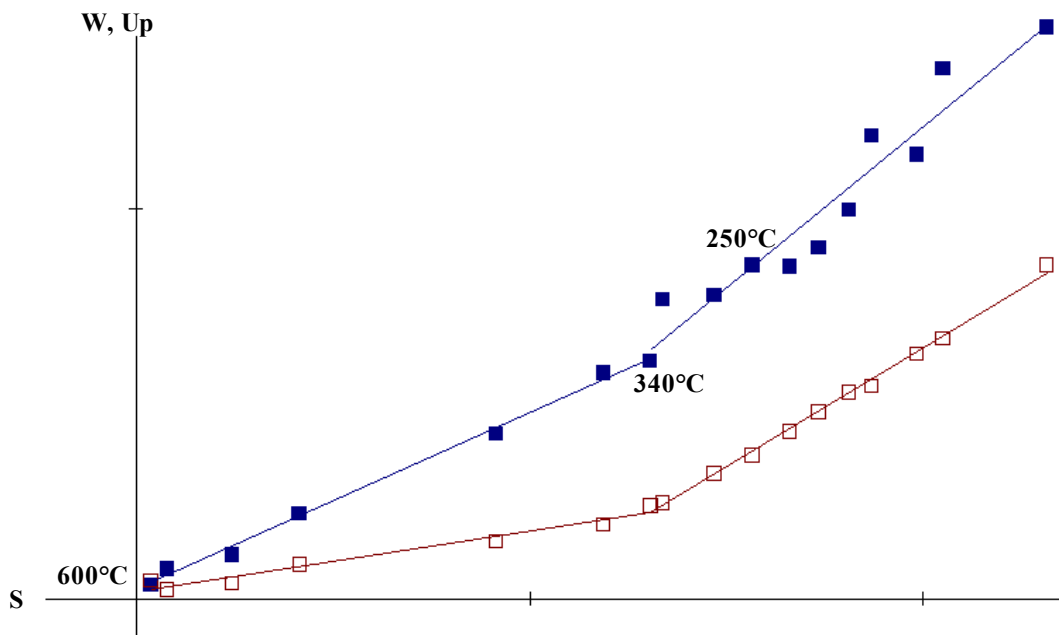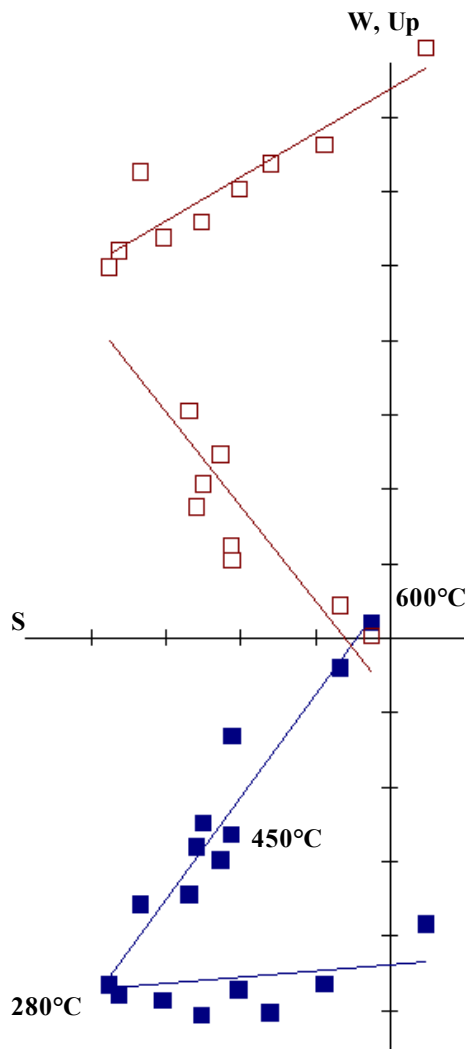
Figure 16: VC6F – type 2 behaviour. Two components of magnetisation: 1) high-T_B: NNW, up; 2) low-T_B: NW, up.

Figure 17: VC8G2 – type 2 behaviour. Two components of magnetisation: 1) high-T_B: NNW, up; 2) low-T_B: NW, up.
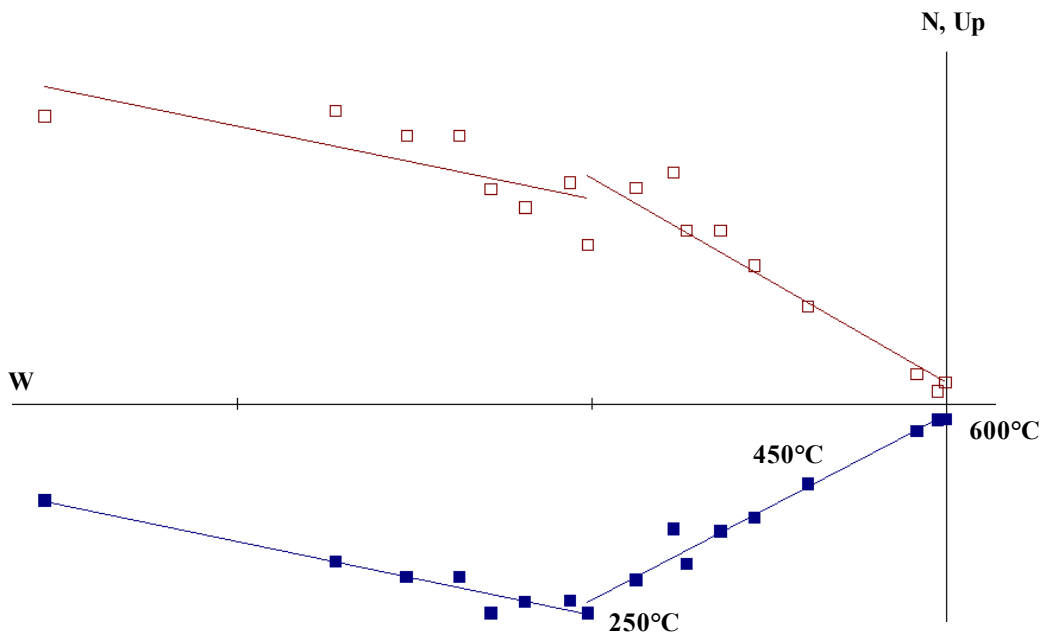
24

Figure 18: VC8L – type 2 behaviour. Two components of magnetisation: 1) high-T$_B$: SW, up; 2) low-T$_B$: W, up.
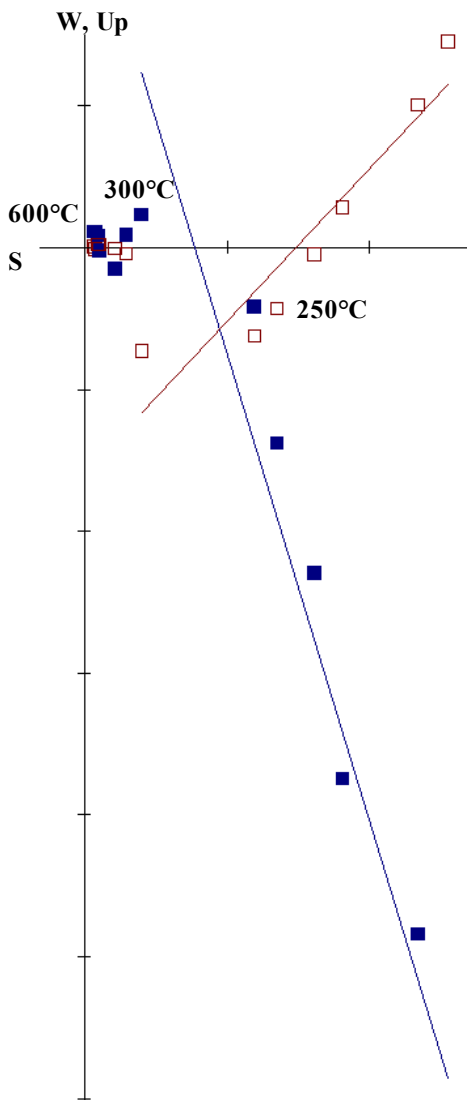

Figure 19: VC3K5A – type 3 behaviour. Two components of magnetisation: 1) high-T$_B$: noisy; 2) low-T$_B$: ENE, up.
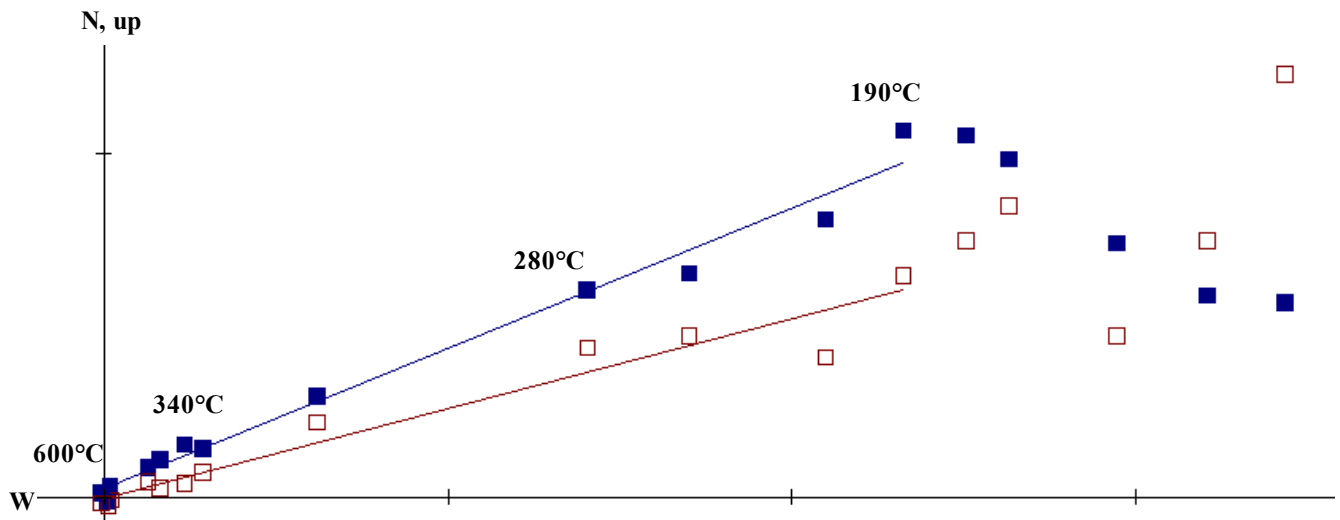
Figure 20: VC3H2 – type 4 behaviour. Two components of magnetisation: 1) high-T_B: NE, up; 2) low-T_B: noisy.
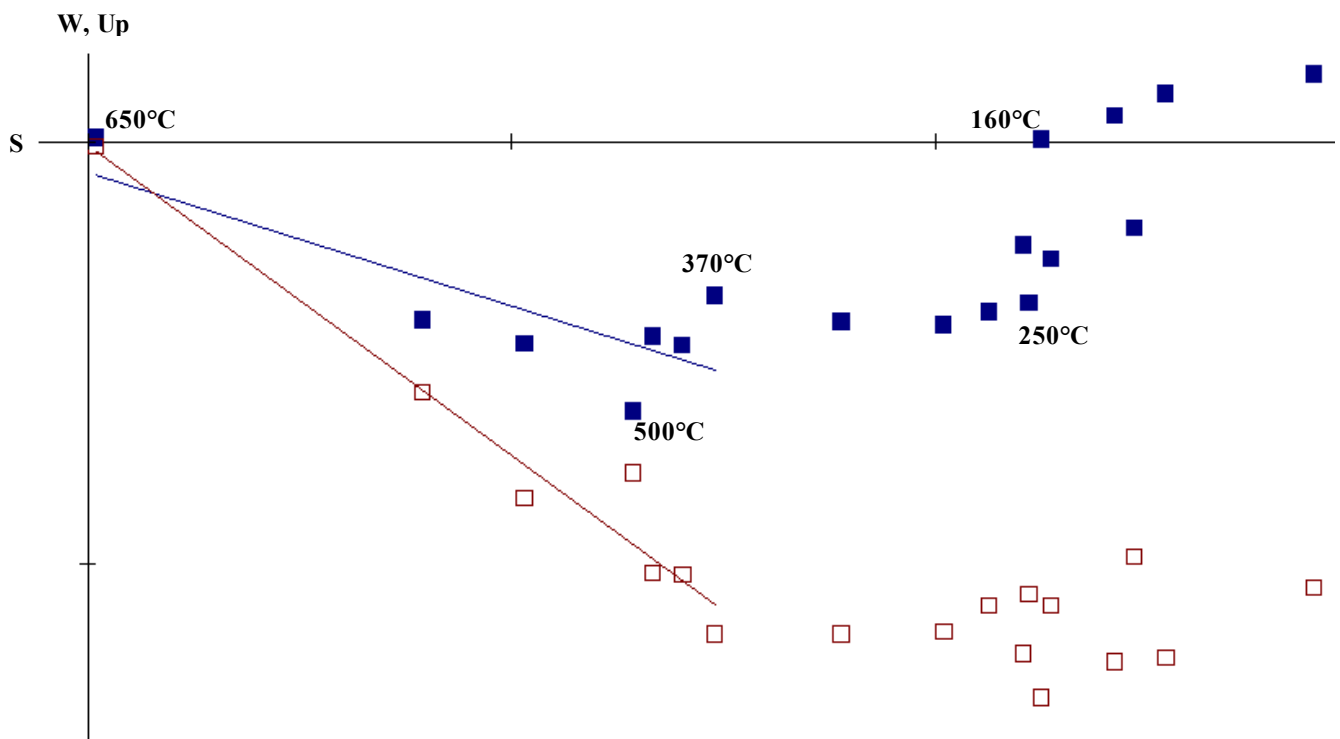

Figure 21: VC6C – type 4 behaviour. Two components of magnetisation: 1) high-T_B: ENE, down; 2) low-T_B: noisy.
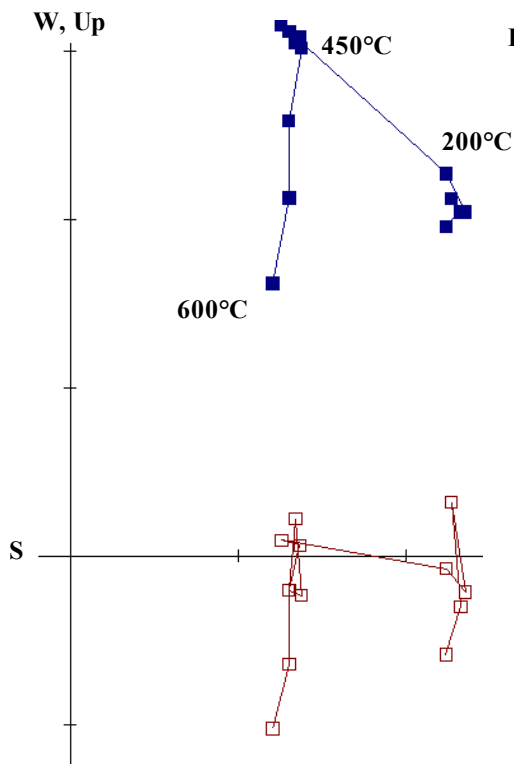
Figure 22: VC9B1 – not fully demagnetised sample.

The results of the TRM analysis can only be used to estimate the deposits' T_{empl} if the directions of the different components of NRM are correctly and statistically grouped. Ideally, for clasts which show two components of remanent magnetisation, the low-T_B components should cluster and show directions that are similar to the Earth's magnetic field at the time of their deposition. The high-T_B components should be unclustered, with random magnetic orientations. Stereograms can be used to illustrate the directions shown by each measured clast. Figures 23 – 27 are a selection of stereograms that show the low-T_B components for sites 1, 3, 6, 8 and 10; Figures 28 & 29 show the high-T_B components for sites 4 and 10. Open squares show directions in the upper hemisphere; closed squares show directions in the lower hemisphere. Table 6 shows the average directions of the low- and high-T_B components of remanence at each site.
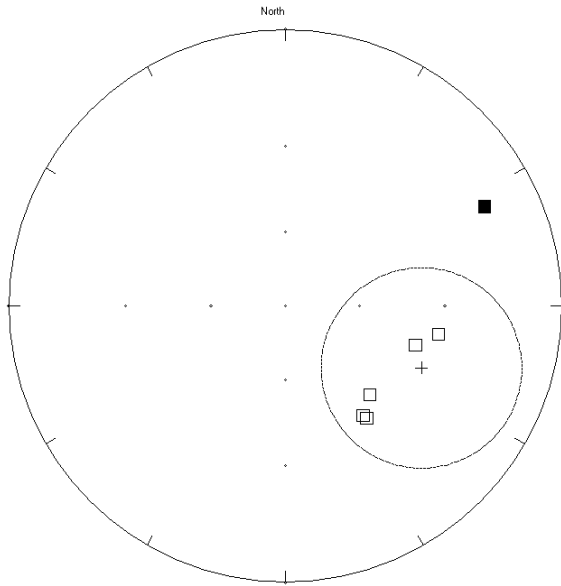
Figure 23: Site 1 low-T$_B$ components – grouped in the direction ESE, up (sites 2, 4 & 11 have similar directions).
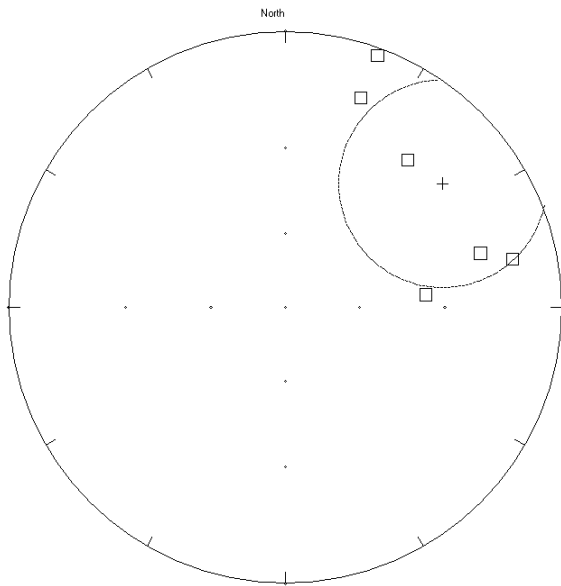

Figure 24: Site 3 low-T$_B$ components – grouped in the direction NE, up.

Figure 25: Site 6 low-T$_B$ components – grouped in the direction N, up (site 7 has a similar direction).

Figure 26: Site 8 low-T_B components – grouped in the direction NW, up.

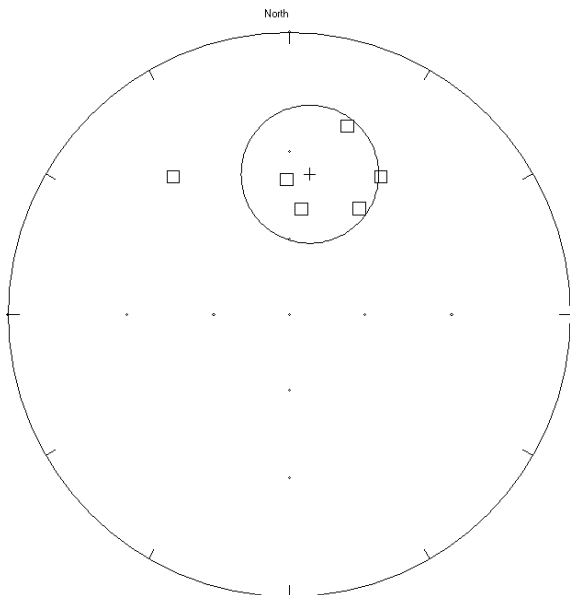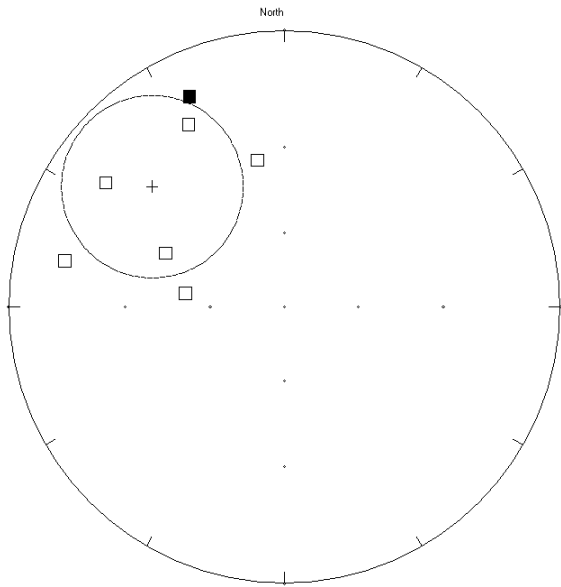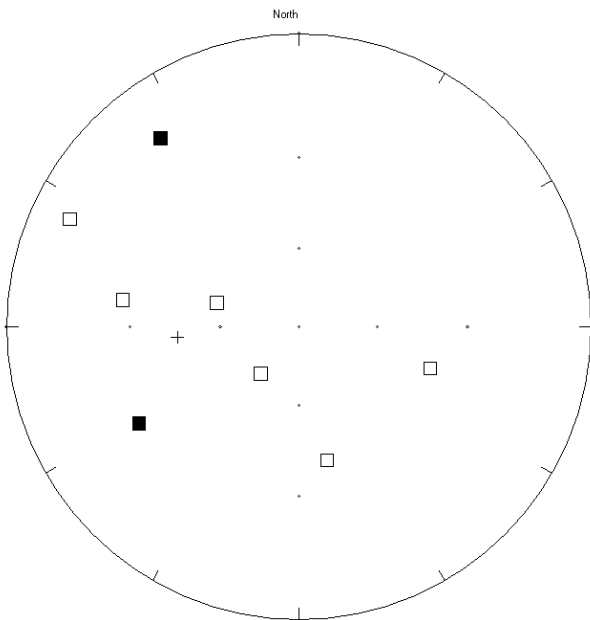 **Figure 26: Site 8 low-T_B components – grouped in the direction NW, up.**

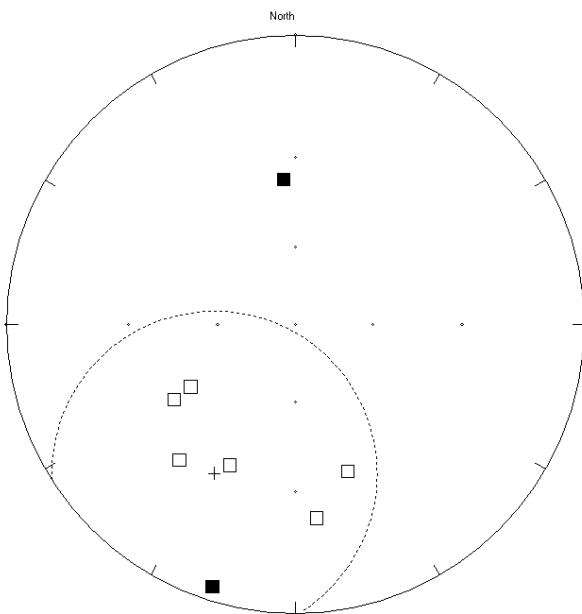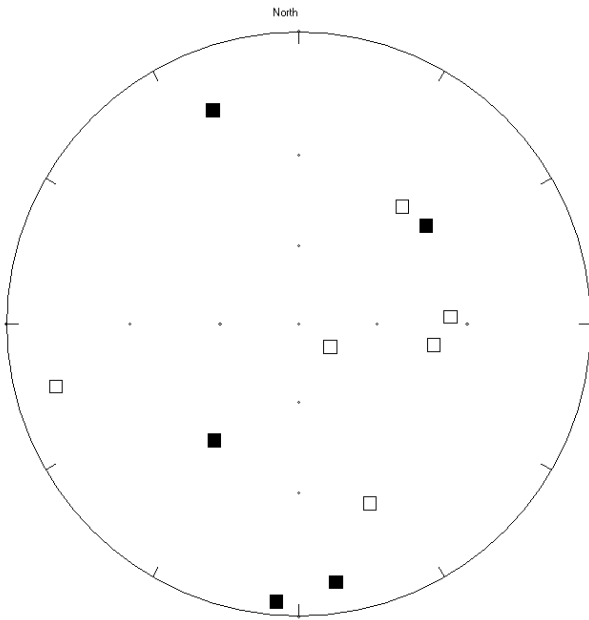**Figure 27: Site 10 low-T_B components – not grouped.**

Figure 28: Site 4 high-T_B components – grouped in the direction SSW, up.

29

Figure 29: Site 10 high-T$_B$ components – not grouped.

Fisher (1953) statistics can be used to find the dispersion of data around a mean for spherical coordinates. This method assumes a geocentric axial dipole model (GAD) for the Earth's magnetic field (ie. it can be approximated by a single magnetic dipole at the centre of the Earth, aligned with the rotation axis). The statistical results for each site are shown in Table 5. **R** illustrates whether the grouping of components is random, when **R** is greater than a critical value (**R$_0$**), which is dependent on the number of samples (N) the grouping is statistically not random. α$_{95}$ and *k* both assess the amount of dispersion of the data around the mean direction. α$_{95}$ is the semi-angle of the cone of 95% confidence about the mean and *k* is the dispersion of the vector directions. Lower values for α$_{95}$ and higher values for *k* are indicative of better quality data. Appendix F shows how these parameters are calculated.

The stereograms in Figures 23 – 27 show that there are certain low-T$_B$ components that have inclinations which are obviously different to the others at their site. When these particular samples are removed from the analysis, the accuracy of the data can be improved. Table 6 shows the adjusted statistical results when lines for the following samples are removed: VC1L, VC2G1, VC4H1, VC5F2, VC7H, VC8C2, VC9M4, VC10F1, VC10L3, VC11F1, VC11H1.

Site No.	Component	Average Declination (°)	Average Inclination (°)	Average direction of magnetisation	$N_{lines}/N_{samples}$	R	R_0	Random?	α_{95}	k
1	Low	114.5	-33.1	ESE, up	6/9	5.13	3.85	No	30.6	5.73
1	High	94.6	16.8	E, down	7/9	4.30	4.18	No	53.7	2.22
2	Low	135.5	-23.6	SE, up	5/11	4.71	3.50	No	21.3	13.89
2	High	110.0	44.2	ESE, down	7/11	4.88	4.18	No	44.1	2.83
3	Low	51.8	-18.2	NE, up	6/10	5.3	3.85	No	26.9	7.15
3	High	25.3	10.1	NNE, down	8/10	4.21	4.25	Yes	58.7	1.85
4	Low	162.4	-34.2	SSE, up	7/9	6.16	4.18	No	24.3	7.10
4	High	208.4	-29.2	SSW, up	8/9	5.31	4.48	No	43.2	2.60
5	Low	58.4	-85.1	NE, up	11/13	5.64	5.28	No	48.1	1.86
5	High	81.1	-30.6	E, up	5/13	3.68	3.50	No	53.2	3.03
6	Low	8.4	-36.7	N, up	6/9	5.52	3.85	No	21.9	10.33
6	High	4.0	37.1	N, down	7/9	1.67	4.18	Yes	-	1.13
7	Low	16.2	-20.2	NNE, up	9/11	6.68	4.76	No	32.6	3.46
7	High	27.8	9.7	NNE, down	10/11	5.64	5.03	No	46.0	2.07
8	Low	312.2	-24.3	NW, up	7/9	6.08	4.18	No	25.6	6.49
8	High	8.9	-79.0	N, up	7/9	3.77	4.18	Yes	63.5	1.86
9	Low	160.2	-12.4	SSE, up	6/11	3.82	3.85	Yes	57.8	2.30
9	High	195.0	18.7	SSW, down	9/11	5.11	4.76	No	49.2	2.06
10	Low	264.9	-44.9	W, up	8/11	4.25	4.48	Yes	58.1	1.87
10	High	139.7	-34.7	SE, up	11/11	3.05	5.28	Yes	84.8	1.26
11	Low	123.9	-47.3	ESE, up	7/9	4.82	3.85	No	45.0	2.76
11	High	81.3	-10.1	E, up	5/9	0.86	3.85	Yes	-	0.97

Table 5: Results of Fisher statistics for low- and high-T_B components of each site.

Site No.	Component	Average Declination (°)	Average Inclination (°)	Average direction of magnetisation	N_lines/N_samples	R	R_0	Random?	α_95	k
1	Low	126.2	-38.7	ESE, up	5/9	4.82	3.50	No	16.7	21.85
1	High	94.6	16.8	E, down	7/9	4.30	4.18	No	53.7	2.22
2	Low	138.7	-31.2	SE, up	4/11	3.92	3.10	No	15.6	35.76
2	High	110.0	44.2	ESE, down	7/11	4.88	4.18	No	44.1	2.83
3	Low	51.8	-18.2	NE, up	6/10	5.30	3.85	No	26.9	7.15
3	High	25.3	10.1	NNE, down	8/10	4.21	4.25	Yes	58.7	1.85
4	Low	170.4	-40.0	S, up	6/9	5.70	3.85	No	16.9	16.67
4	High	208.4	-29.2	SSW, up	8/9	5.31	4.48	No	43.2	2.60
5	Low	342.0	-83.9	NNW, up	10/13	6.33	5.03	No	39.5	2.45
5	High	81.1	-30.6	E, up	5/13	3.68	3.50	No	53.2	3.03
6	Low	8.4	-36.7	N, up	6/9	5.52	3.85	No	21.9	10.33
6	High	4.0	37.1	N, down	7/9	1.67	4.18	Yes	-	1.13
7	Low	11.7	-20.2	N, up	8/11	7.53	4.48	No	14.8	15.00
7	High	27.8	9.7	NNE, down	10/11	5.64	5.03	No	46.0	2.07
8	Low	307.4	-29.9	WNW, up	6/9	5.37	3.85	No	25.4	7.90
8	High	21.7	-88.7	NNE, up	6/9	2.94	3.85	Yes	81.5	1.64
9	Low	172.5	-19.9	S, up	5/11	3.33	3.50	Yes	63.8	2.4
9	High	195.0	18.7	S, down	9/11	5.11	4.76	No	49.2	2.06
10	Low	250.5	-64.4	WSW, up	6/11	4.04	3.85	No	53.0	2.55
10	High	139.7	-34.7	SE, up	11/11	3.05	5.28	Yes	84.8	1.26
11	Low	131.2	-66.0	SE, up	5/9	4.50	3.50	No	28.9	7.94
11	High	81.3	-10.1	E, up	5/9	0.86	3.85	Yes	-	0.97

Table 6: Results of Fisher statistics with selected low-T_B components removed.

4.2 High-temperature susceptibility & IRM

Figures 30 – 32 show the results for a selection of samples that underwent high-temperature susceptibility measurements (others can be found in Appendix D). The main magnetic mineral in the sample can be identified by its T_C. This is the point where the steepest part of the heating (red) curve (approximated by the dashed green line) intercepts the *x*-axis. The difference in the shape of the heating and cooling (blue) curves is due to the alteration of minerals on heating.
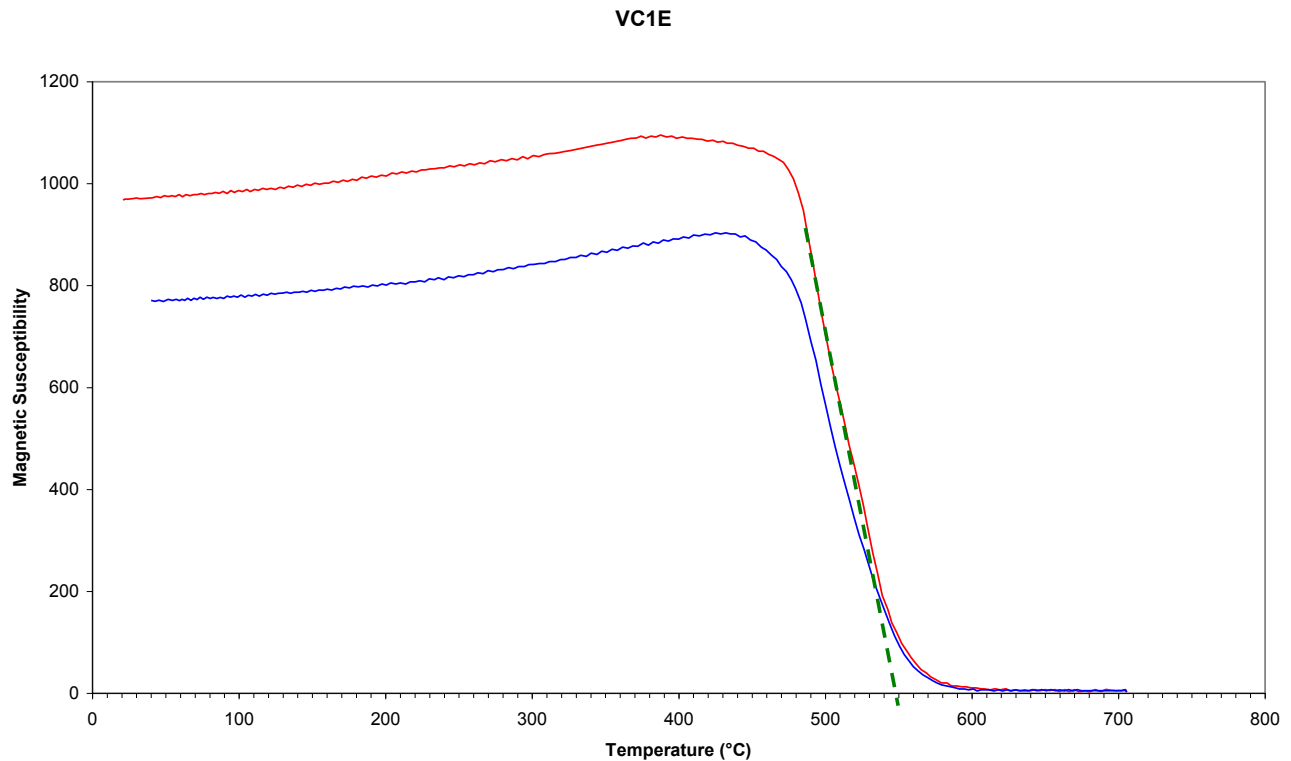
VC1E

Figure 30: High-temperature susceptibility of VC1E. This sample has a T_C of ~550°C, indicative of a titanomagnetite with composition very close to that of magnetite (TM0).

VC4D

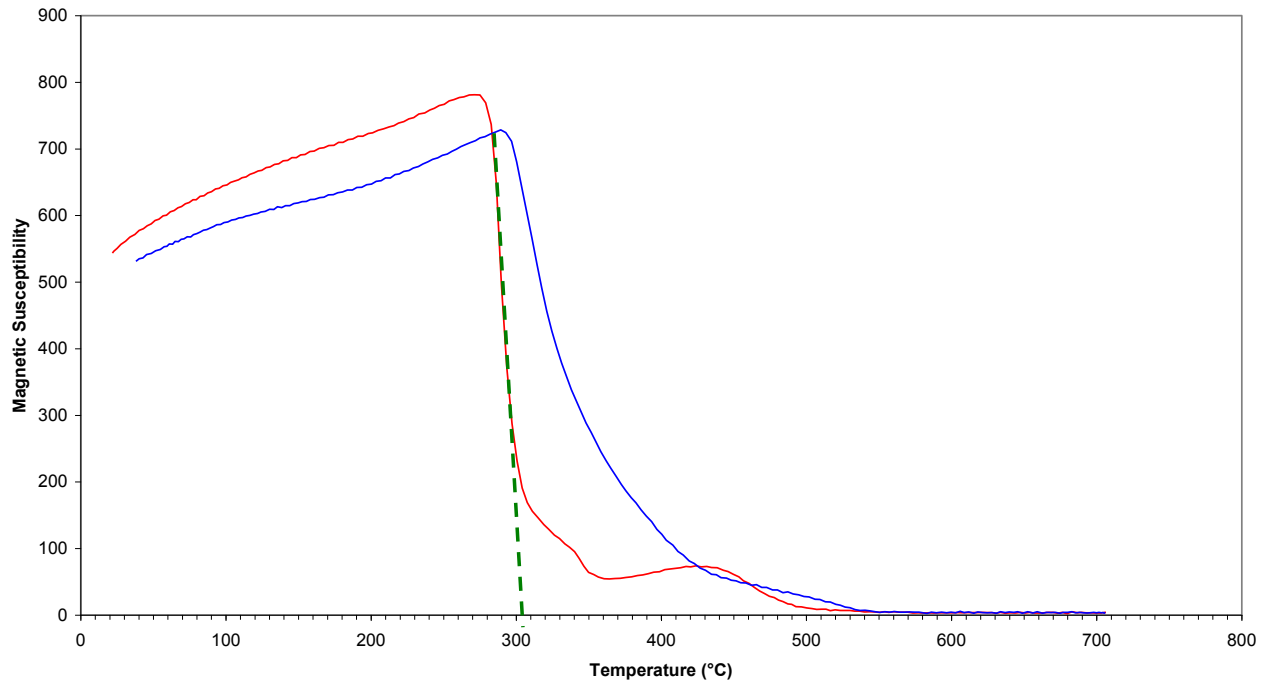**Figure 31: High-temperature susceptibility of VC4D. This sample has a T_C of ~300°C, which could be indicative of either a titanomagnetite with composition TM45 or a sulphide mineral such as pyrrhotite.**

VC9F

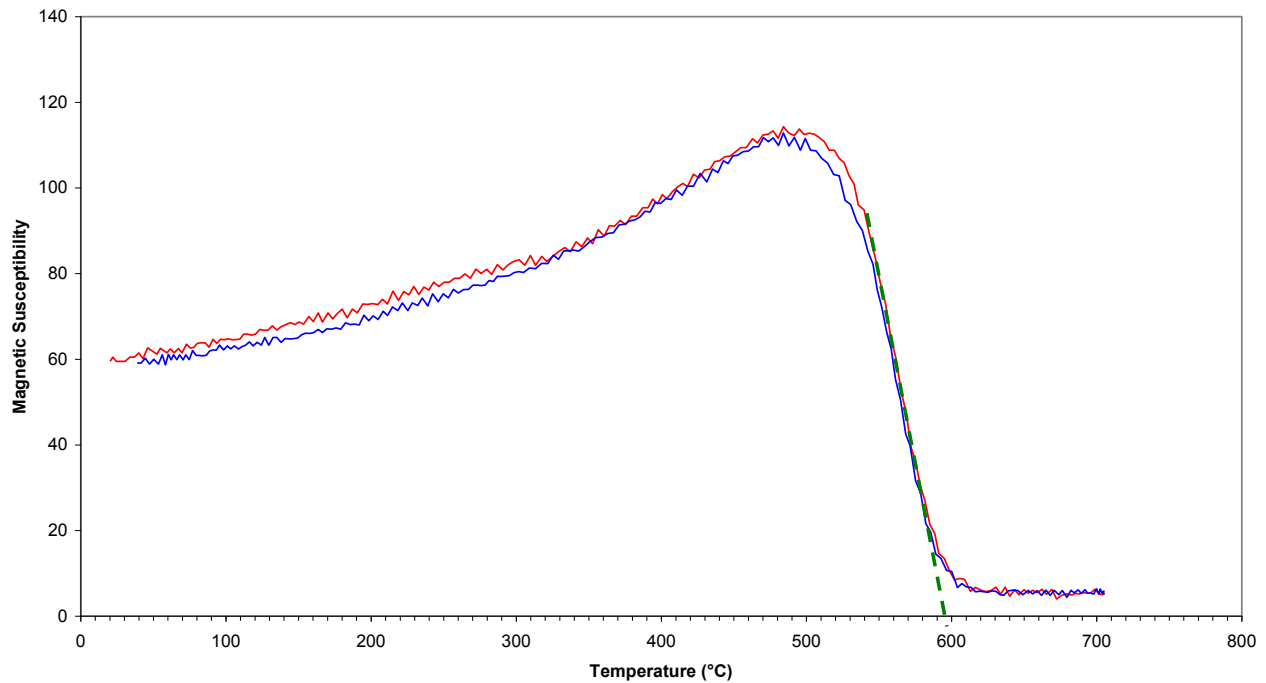**Figure 32: High-temperature susceptibility of VC9F. This sample has a T_C of ~600°C, indicative of maghaemite (a common oxidation product of magnetite during weathering at ambient surface temperatures or hydrothermal alteration at temperatures < 200°C).**

Sample	T$_C$ (°C)	Magnetic mineral	Sample	T$_C$ (°C)	Magnetic mineral
VC1A	370	Titanomagnetite	VC5B	540	Titanomagnetite
VC1B	565	Magnetite	VC5D	575	Magnetite
VC1C	540	Titanomagnetite	VC5E	550	Titanomagnetite
VC1D	390	Titanomagnetite	VC5F	560	Titanomagnetite
VC1E	550	Titanomagnetite	VC5H	480 / 590	Titanomagnetite / maghaemite
VC1F	530	Titanomagnetite	VC5L	310	Titanomagnetite
VC1G	485	Titanomagnetite	VC6A	545	Titanomagnetite
VC1H	565	Magnetite	VC6C	390 / 530	Titanomagnetite
VC1K*	470	Titanomagnetite	VC7B	365 / 510	Titanomagnetite
VC1L	530	Titanomagnetite	VC7G	410	Titanomagnetite
VC2E	295	Titanomagnetite	VC8B	500	Titanomagnetite
VC2L	570	Magnetite	VC8C	560	Titanomagnetite
VC3A*	310	Titanomagnetite	VC8F	340	Titanomagnetite
VC3D	- (altered?)	-	VC8M	380	Titanomagnetite
VC3E	325	Sulphide? Titanomagnetite?	VC9A	370	Titanomagnetite
VC3G	560	Titanomagnetite	VC9D*	540	Titanomagnetite
VC3H	330	Sulphide? Titanomagnetite?	VC9F	595	Maghaemite
VC3K*	330	Sulphide? Titanomagnetite?	VC9M	570	Magnetite
VC3L	280	Titanomagnetite	VC10E	560	Titanomagnetite
VC4A	310	Titanomagnetite	VC11A*	460	Titanomagnetite
VC4B*	325	Sulphide? Titanomagnetite?	VC11F	570	Magnetite
VC4C	350	Titanomagnetite	VC11K	530	Titanomagnetite
VC4D*	305	Titanomagnetite			
VC4E	370 / 500	Titanomagnetite			
VC4F	550	Titanomagnetite			
VC4G	285	Titanomagnetite			
VC4H	485	Titanomagnetite			
VC4K	550	Titanomagnetite			
VC5A*	570	Magnetite			

Table 7 Results from high-temperature susceptibility measurements. Those marked with * underwent IRM analysis.

Table 7 shows that for the majority of the clasts, the remanence carrying mineral is part of the titanomagnetite series. The series has magnetite (Fe_3O_4) and ulvöspinel (Fe_2TiO_4) as end-members (T_C of 575-585°C and -153°C respectively). Single-phase titanomagnetites ($Fe_{3-x}Ti_xO_4$) are inverse spinels. With increasing substitution of Ti^{4+}, the exchange coupling in the mineral is weakened and the T_C falls almost linearly with increasing x. Natural intermediate titanomagnetites may also contain up to 10% Mg and Al, which further lowers the T_C values. Some clasts have a T_C that could be representative of either sulphides or simply titanomagnetites with compositions that yield these temperatures (~300°C). The most magnetic of the iron sulphides is pyrrhotite (found in various types of igneous rocks), its T_C is dependent on its composition, ranging from 320°C for Fe_7S_8 to 290°C for Fe_9S_{10}.

In order to distinguish between these two possibilities further analysis was undertaken on eight samples (those marked * in Table 7). The results of this procedure are shown in Figures 33 & 34 (also Appendix E) and Table 8. If an iron sulphide such as pyrrhotite is present as the main remanence carrying mineral in any of these samples, its coercive force (point of intercept on the x-axis) should be greater than that for magnetite and its saturation remanence (maximum / minimum intensity) should be smaller (Dekkers, 1988); both these properties are grain-size dependent. By comparing the values for those samples suspected of containing sulphides and those that clearly contain titanomagnetites, it is shown that these samples do not contain a significant proportion of non-titanomagnetite minerals.

Sample	Coercive Force (mT)	Saturation Magnetisation (A/m)
VC1K1	10	~145
VC3A2*	10	~155
VC3K4A*	10	~145
VC4B3B*	15	~220
VC4D1*	10	~120
VC5A6	30	~550
VC9D3A	20	~140
VC11A2	20	~280

Table 8: Results from IRM analysis. Samples marked with * are those that may have been interpreted to contain sulphide minerals based on their T_C alone.
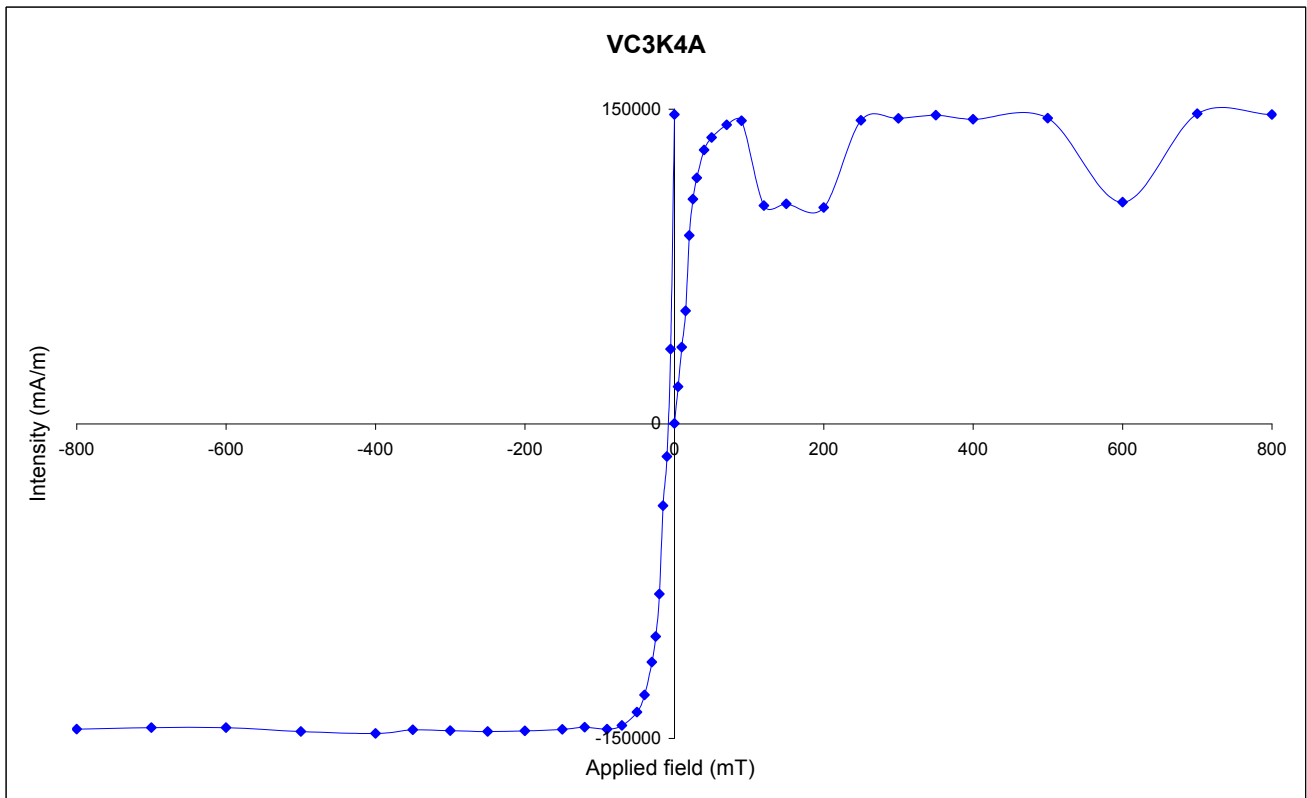
Figure 33: IRM curve for sample VC3K4A whose T_C suggested the presence of sulphide minerals. Noise in the positive curves may be due to range switching during acquisition.
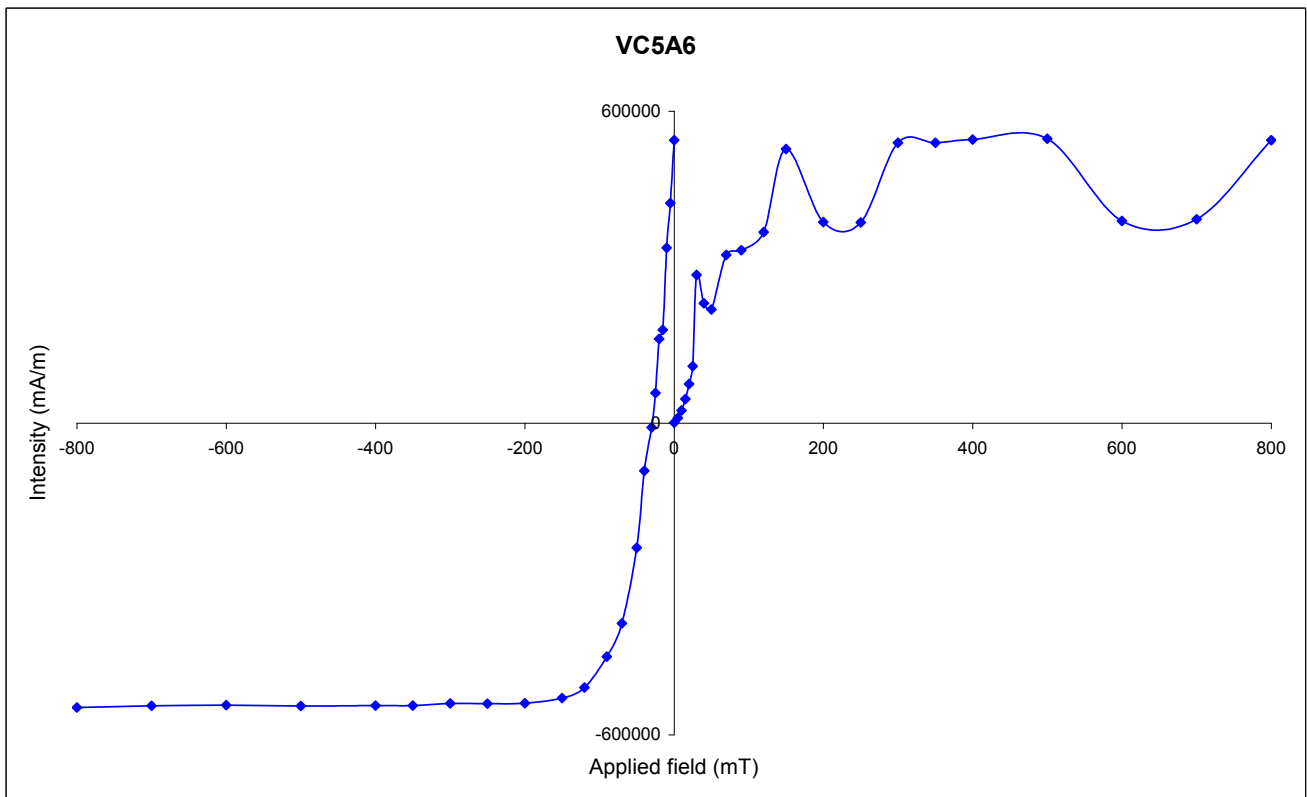

Figure 34: IRM curve for sample VC5A6 whose T_C indicated magnetite is the major remanence carrying mineral.
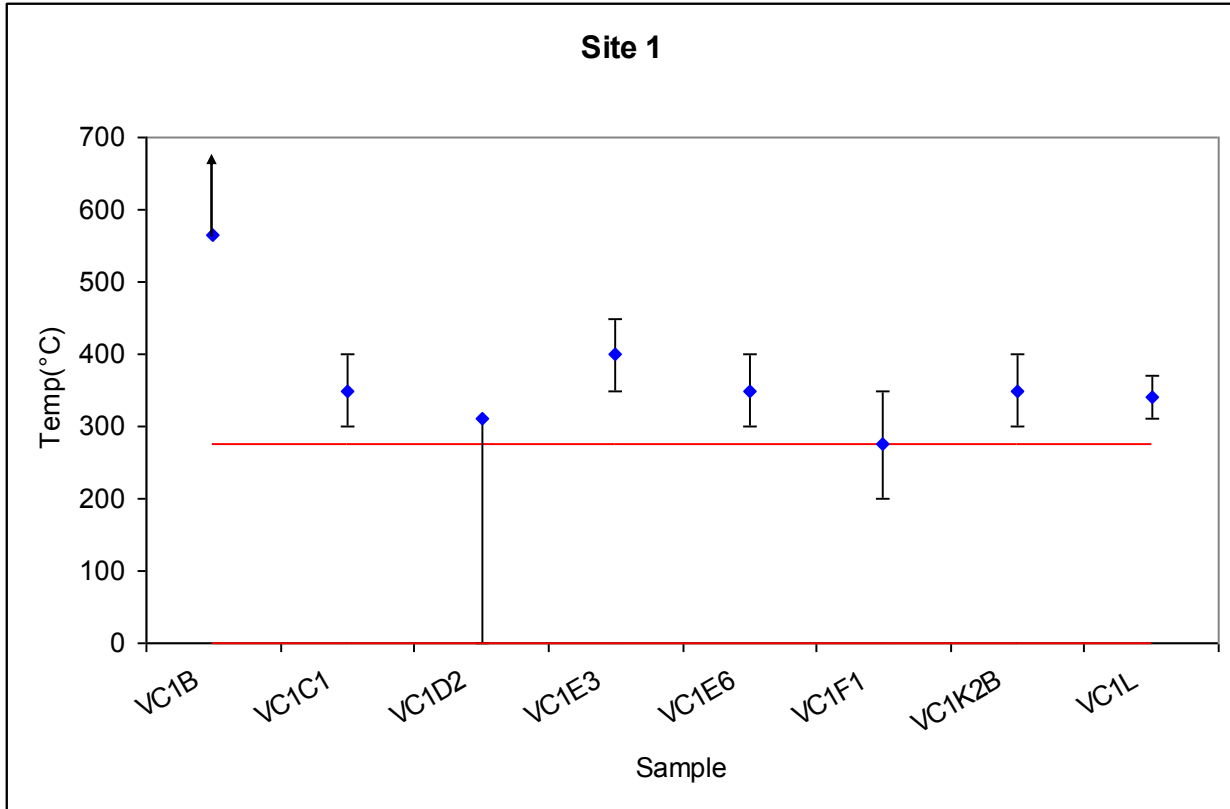
5. DISCUSSION

Figure 35: Estimated emplacement temperatures for clasts and equilibrium temperature of site 1.
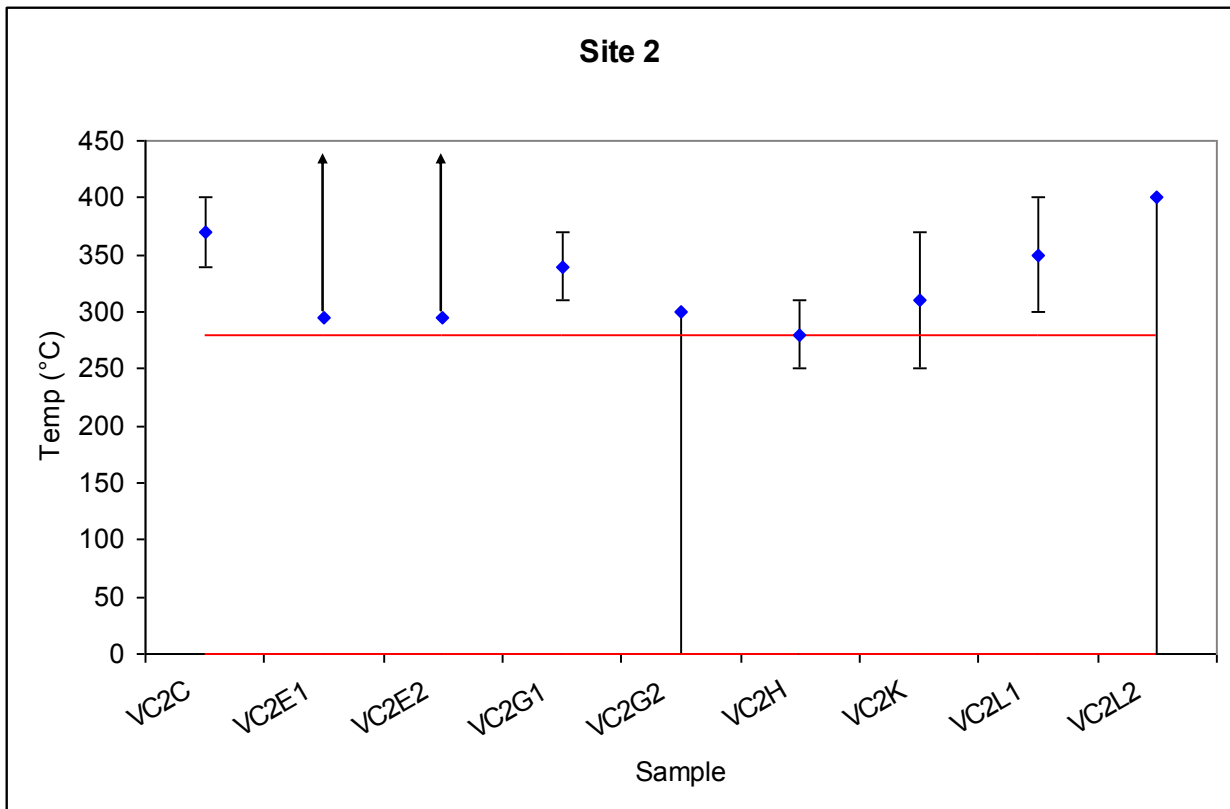

Figure 36: Estimated emplacement temperatures for clasts and equilibrium temperature of site 2.
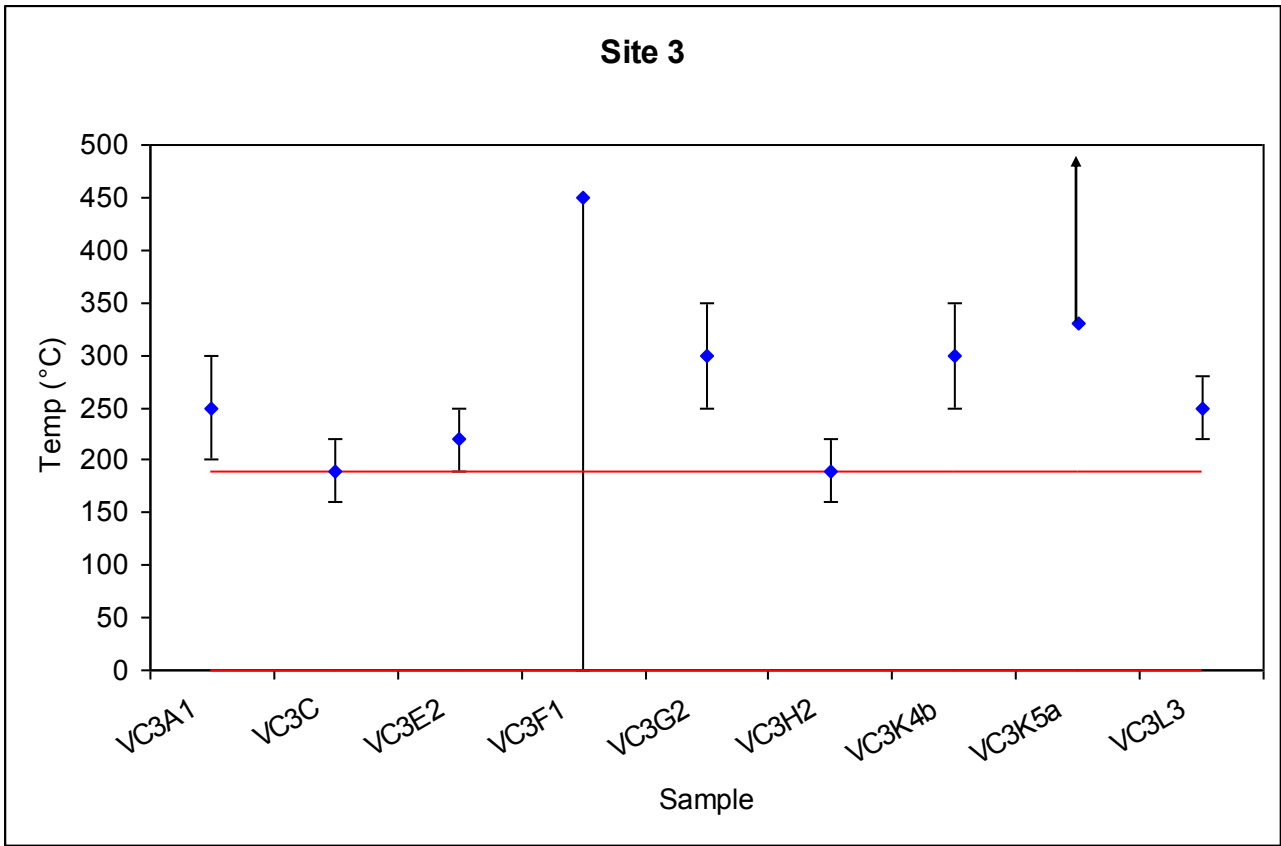
Figure 37: Estimated emplacement temperatures for clasts and equilibrium temperature of site 3.
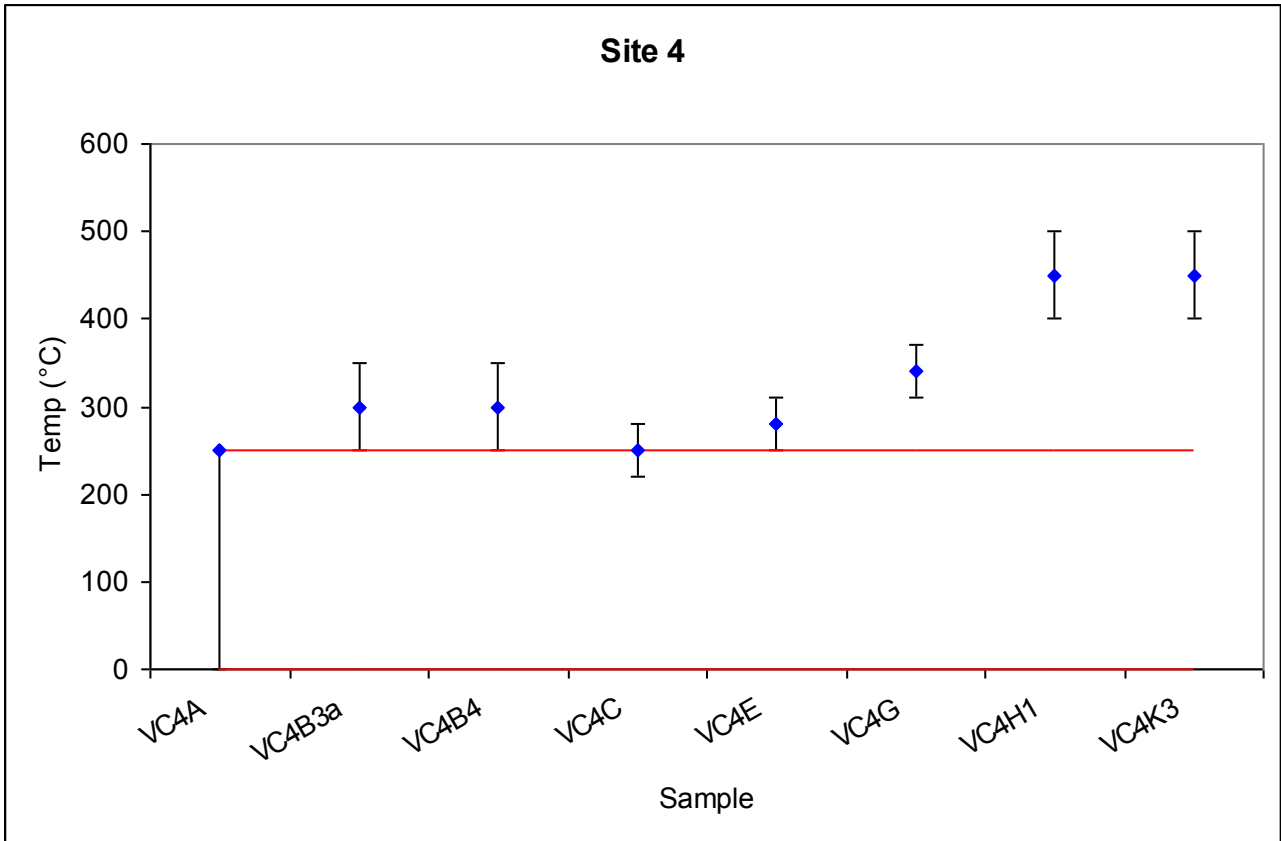

Figure 38: Estimated emplacement temperatures for clasts and equilibrium temperature of site 4.

Figure 39: Estimated emplacement temperatures for clasts and equilibrium temperature of site 5.

Figure 40: Estimated emplacement temperatures for clasts and equilibrium temperature of site 6.
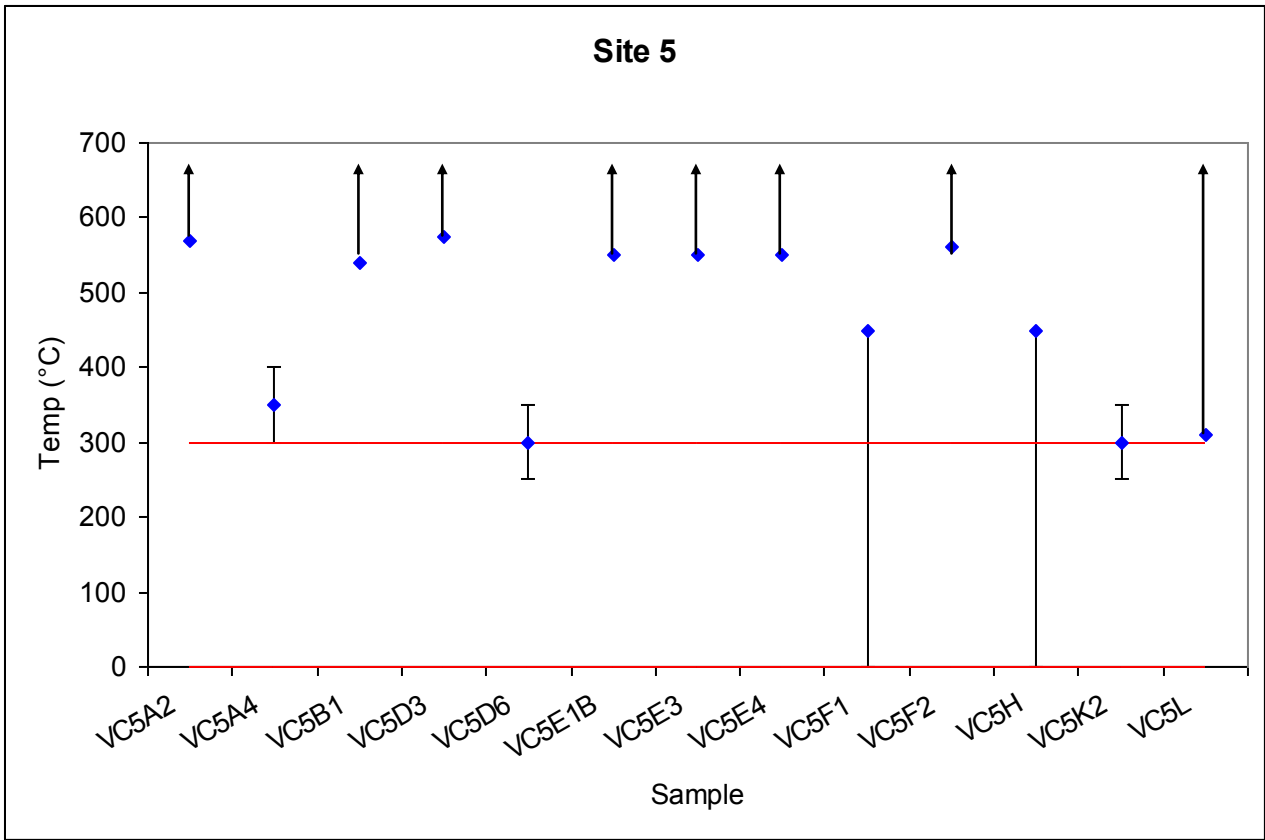
Figure 41: Estimated emplacement temperatures for clasts and equilibrium temperature of site 7.

Figure 42: Estimated emplacement temperatures for clasts and equilibrium temperature of site 8.

Figure 43: Estimated emplacement temperatures for clasts and equilibrium temperature of site 9.
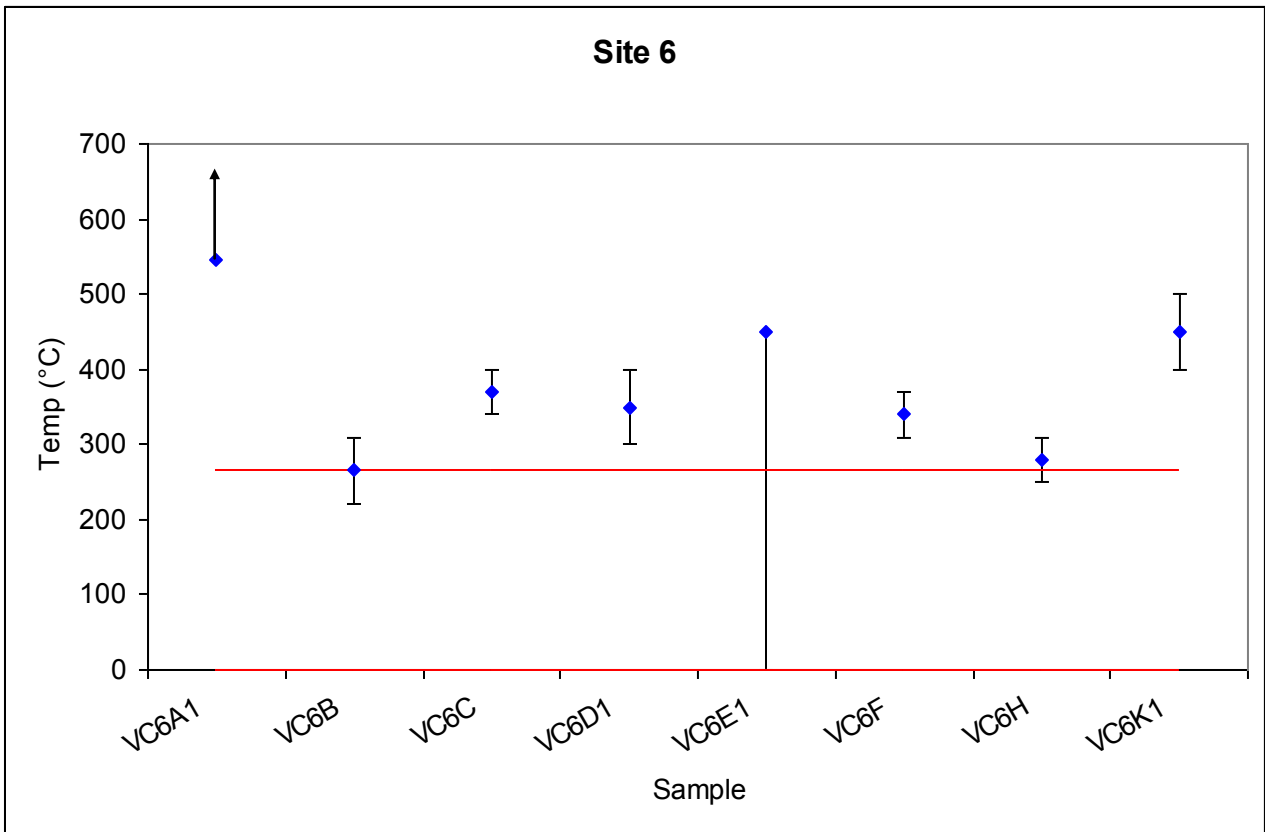

Figure 44: Estimated emplacement temperatures for clasts and equilibrium temperature of site 10.
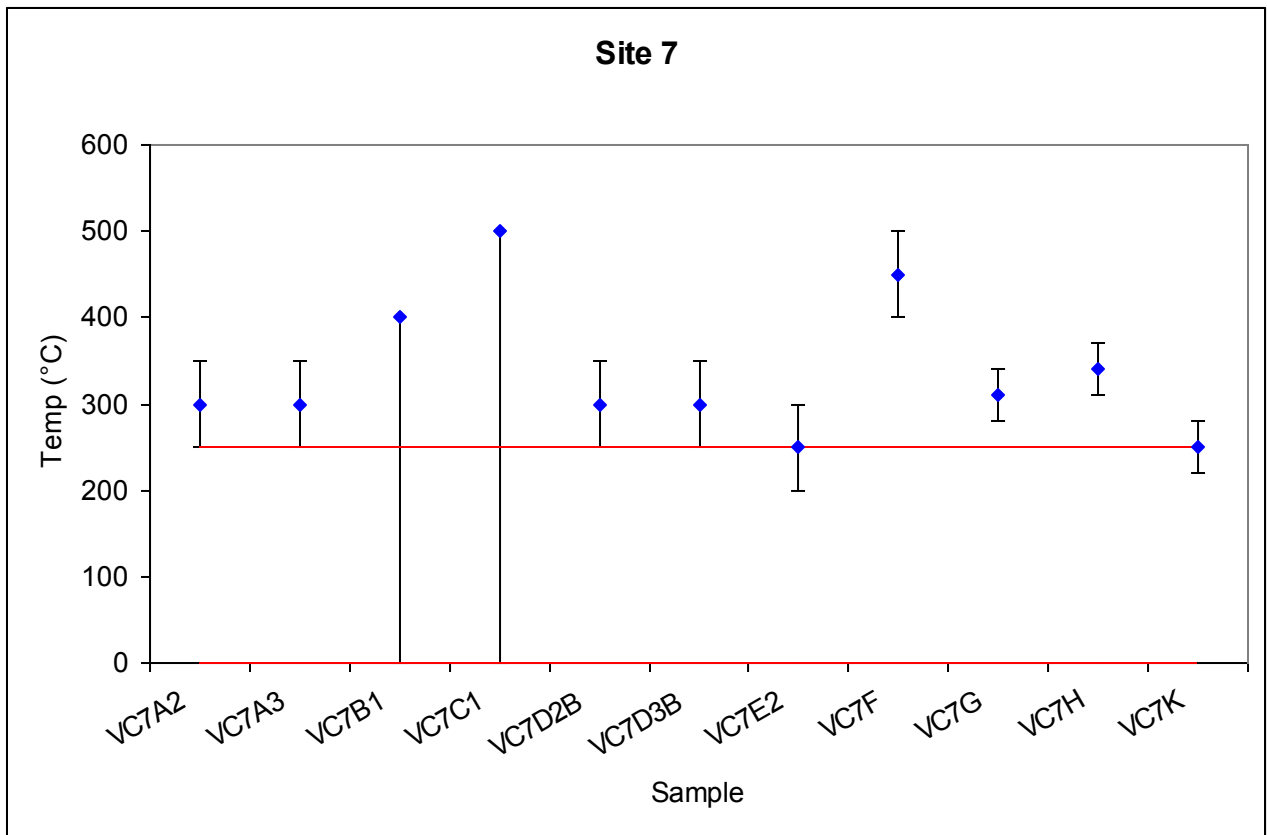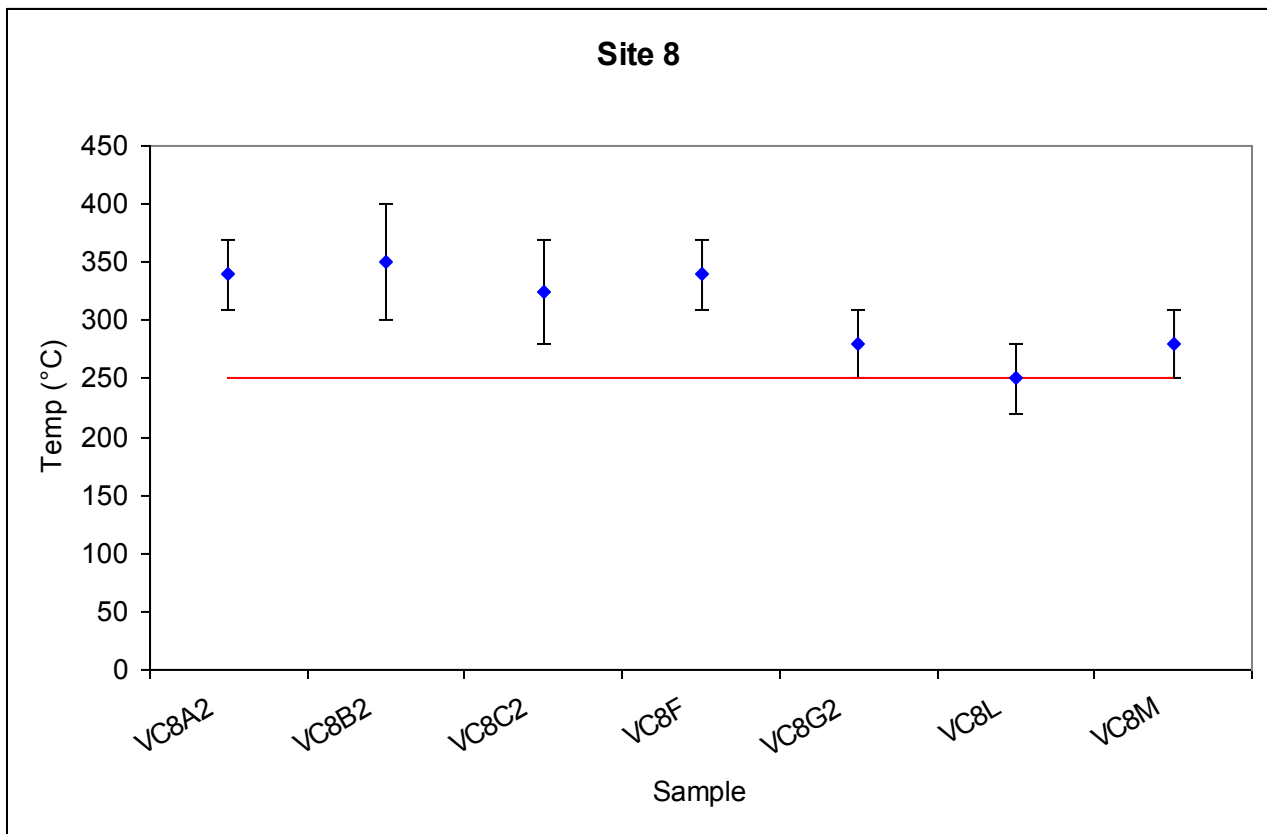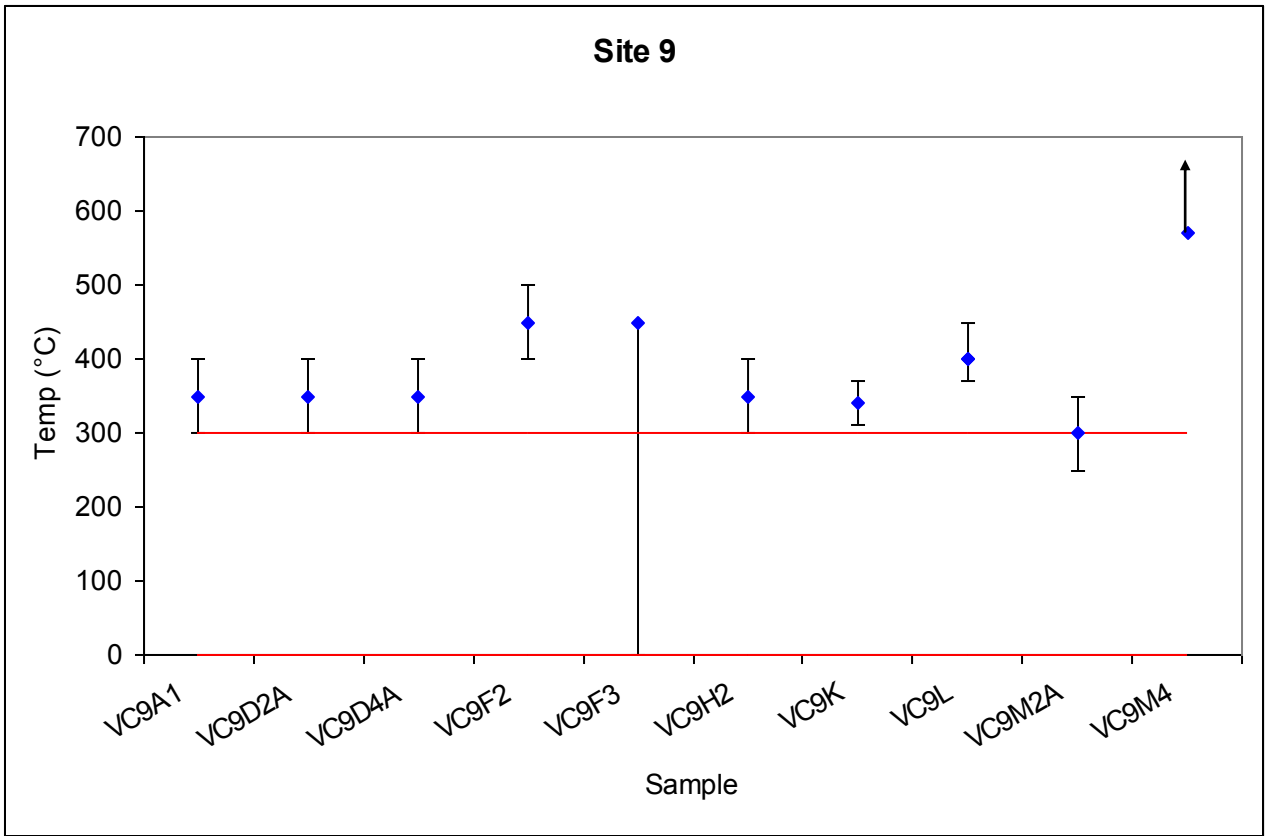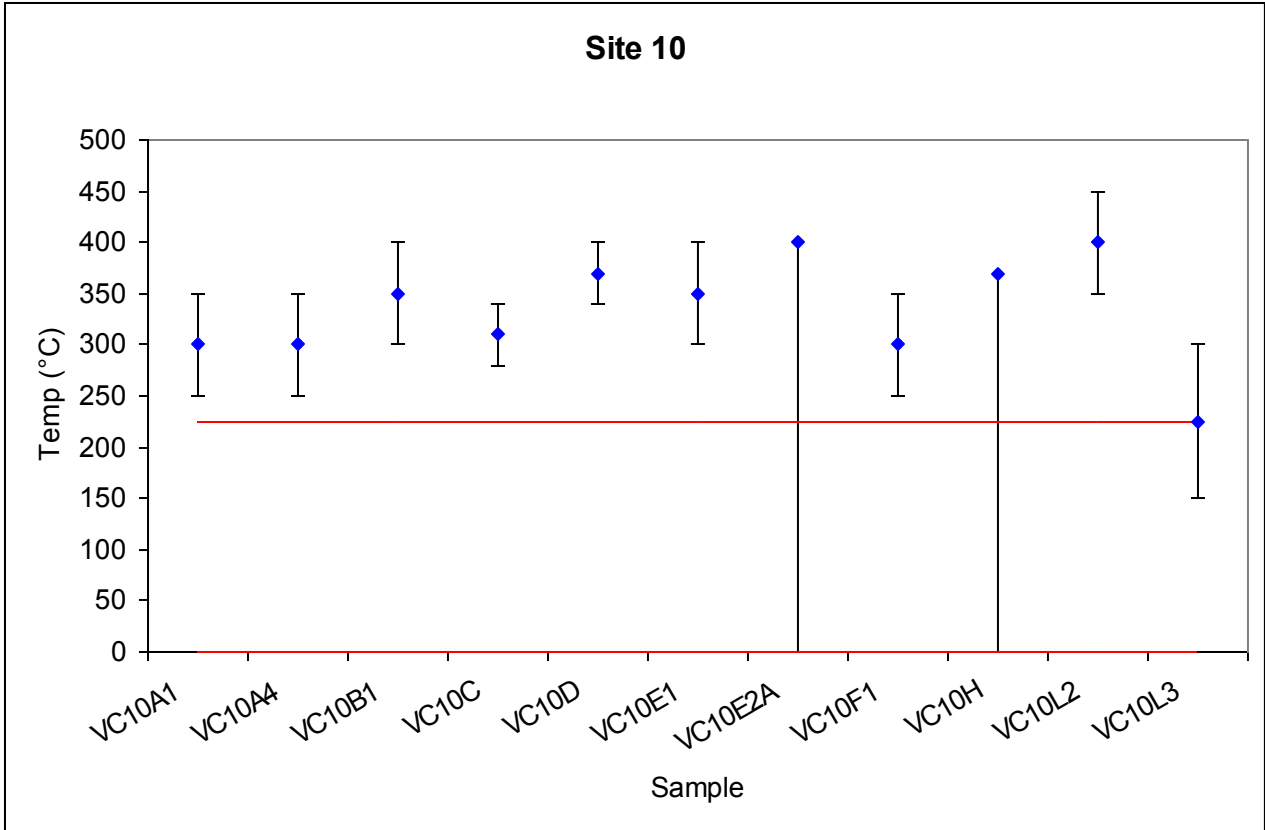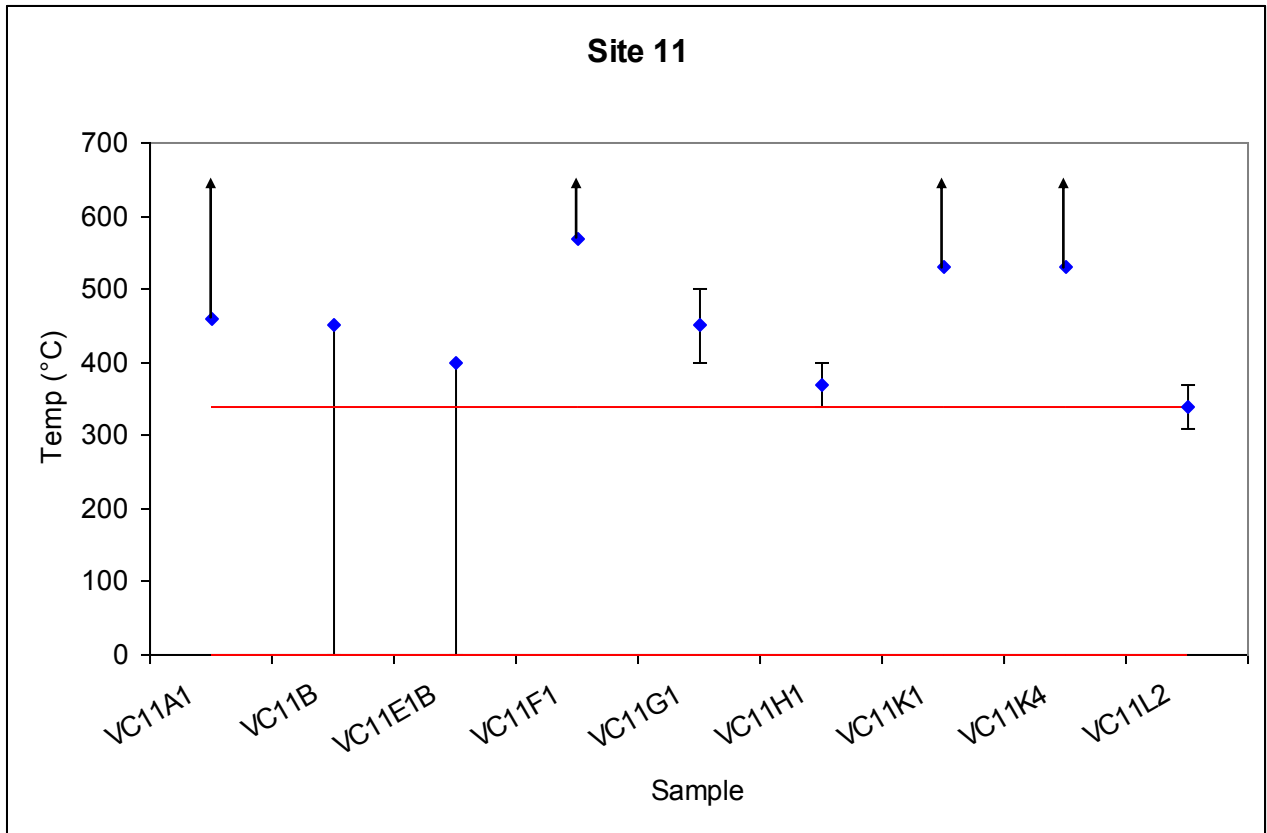
Figure 45: Estimated emplacement temperatures for clasts and equilibrium temperature of site 11.

Figures 35 – 45 show the estimated T_{empl} of clasts at each site. Samples that display type 2 behaviour are represented by points with error bars above and below. The length of the bars corresponds to the magnitude of the preceding and subsequent temperature steps in the demagnetisation sequence. Where an arrow extends above the point, the sample displays either type 1 or type 3 behaviour. T_{empl} can only be constrained to lie above the T_C of the main magnetic mineral in the clast (found in the high-temperature susceptibility measurements). Samples where there is a single error bar that extends down to 0°C, display type 4 behaviour. T_{empl} for these clasts lies somewhere below the lower-limit of the high-T_B component.

5.1. Uncertainties

Uncertainties can arise in a number of places during TRM analyses. Errors in sample orientation or

sample alignment produce some uncertainty, as does instrument noise. For calculating the magnetic declinations and inclinations of the different components of remanence, a GAD model is assumed, even though secular variation of the Earth's magnetic field can be relatively important on short timescales. Overprinting by secondary components of remanence, and imperfections in the recording mechanism of ferromagnetic grains may also give rise to a certain level of uncertainty.

5.2. Equilibrium temperature

The T_{empl} of a pyroclastic flow deposit is dependent on a number of factors: the size, nature and origin of its constituent components, the extent of cooling during transport, and the rate of sedimentation. The simple model upon which TRM determinations of T_{empl} are based is that, during cooling after deposition, a new low-T_B component of magnetisation is acquired by the lithic fragments within the deposit. However, this model is too simple. Different constituents of the deposit take different times to reach thermal equilibrium. This time depends on their relative mass, the extent of time that they reside in the flow, their thermodynamic properties and the size of the fragments. At any time during transport, the temperature of the flow should be thought of as an average temperature of all the components weighted according to their abundance (Cioni *et al.*, 2004).

It is easy to envisage that soon after deposition heat transfer will act to redistribute and equilibrate the heat of each component of the deposit. It is assumed that heat transfer occurs by conduction alone (Riehle, 1973). The redistribution of heat between the hotter and colder lithics will lead to clasts being heated or cooled as they tend towards some equilibrium temperature. The total deposit will also cool as a whole, as its heat is lost to the surroundings. The timescale for the whole deposit to cool is normally much longer than for the redistribution of heat between components, except if immediate cooling occurs, as can be induced by heavy rainfall (Hoblitt *et al.*, 1985).

Those clasts that have an initial temperature (T_{init}) which is greater than the average temperature (T_{av}) of the deposit will cool with time, and thus all ferromagnetic grains with $T_B < T_{init}$ will be remagnetized. The T_{empl} deduced for these clasts with be their T_{init}. For cold clasts, $T_{init} < T_{av}$, so they are heated until they reach the T_{av} of the deposit, before eventually cooling to the ambient temperature. The T_{empl} recorded in these clasts is T_{av}. Lithic clasts in such deposits therefore record T_{empl} that range from T_{av} to the maximum T_{init}. The T_{av} of the deposit is most closely approximated by the lowest value of T_{empl} (McClelland & Druitt, 1989; Bardot, 2000). The T_{av} (or equilibrium temperature, T_{eq}) is represented for each site on Figures 35 - 45 by the area between the two red lines (site 8, Figure 41, has only one red line because its T_{eq} can be constrained with greater confidence). Figure 46 which shows a summary of T_{eq} (the upper limit) for all the sites. Estimated T_{eq} range from a minimum of 190°C at site 3 to a maximum of 340°C at site 11 (within 2σ).

These values seem reasonable and are consistent with results from previous palaeomagnetic determinations of pyroclastic flow emplacement temperatures as well as with the temperatures recorded *in situ* shortly after the eruptions. However, the Fisher statistics (Table 6) show that for six out of the eleven sites, non-ideal behaviour is exhibited. Either the directions of the low-T_B components have a random distribution (site 9), or the high-T_B components are not randomly distributed (sites 1, 2, 4, 5, 7, 9). Furthermore, none of the sites that do display randomly orientated high-T_B components and significantly grouped low-T_B components have low-T_B components in-line with the ambient field. This suggests that the results are not as reliable as the temperature data alone imply.
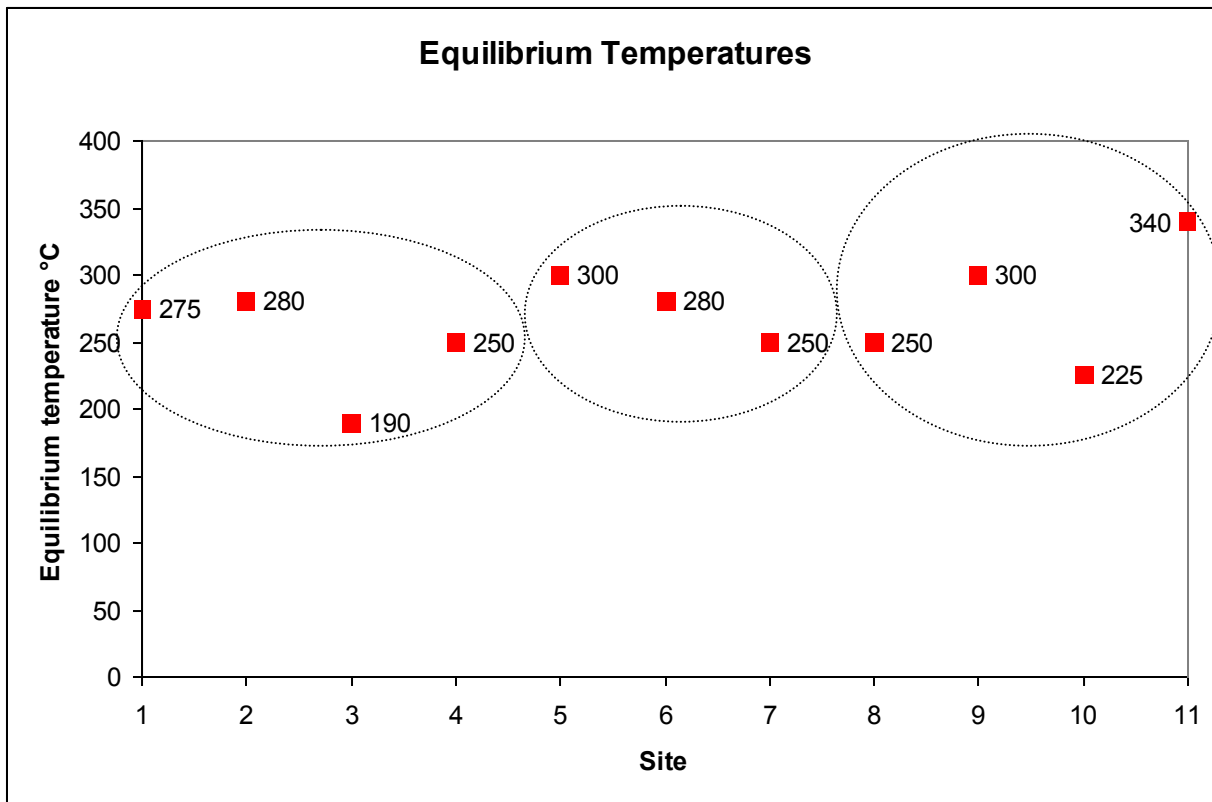
Figure 46: Summary of equilibrium temperatures. Circles indicate the sites that were close spatially.

5.3 Heat transfer in flow and deposit

The temperature within a pyroclastic flow is not homogeneous when its duration is short, because the different components (lithic and juvenile fragments; magmatic gases and external fluids) are incorporated at different times and temperatures, and thus do not have time to equilibrate. The T_{av} of such a flow is dependent on the proportions of each component. To a first approximation, ash-grade juvenile fragments represent the largest mass fraction of a pyroclastic density current (>80 wt %) and can be considered to be thermally and mechanically coupled with the carrying gas. Therefore, it can be assumed that the T_{av} of a flow is approximated by the temperature of the gas-ash mixture (Sparks, 1976; Druitt, 1998). The T_{init} of a gas-ash mixture is the temperature of the magma at the time of eruption, because the coarse and fine-grained juvenile fragments are considered to be in thermal equilibrium (Dobran & Papale, 1993).

Marti *et al.* (1991) stated that determining the proportion of lithic fragments within in a pyroclastic flow is fundamental in determining its final temperature. However, because the heat capacities of lithic and juvenile material are comparable, only a very large fraction of lithics would have a noticeable affect in decreasing the temperature of the flow (Cioni *et al.*, 2004). Lithic clasts with radius <1cm are able to reach thermal equilibrium within the flow before their deposition, and it is these clasts which usually make up the majority of lithic fragments carried by an erupting mixture (Barberi *et al.*, 1989; Gurioli, 2000). However, clasts that are larger than 1cm in radius are used for TRM analyses, and it is these coarser fragments whose thermal evolutions following deposition are important. Therefore, the estimated T_{empl} represent those reached in the deposit rather than those in the flow before emplacement.

It is possible that lithic fragments are partially heated before they enter the magmatic, erupting mixture. This could be the case if they are eroded from the conduit walls, at depth in the volcano rather than from around the vent area. The incorporation of these 'preheated' lithic fragments should cause only a minor thermal perturbation to the carrying mixture. Most sample (large) clasts do not reach thermal equilibrium within the flow and should therefore display thermal gradients across their radius. If this is not the case, then it may be that these clasts were 'preheated', indicating deep provenance or the presence of abundant hot clasts near, or at the surface at the time of the eruption (Cioni *et al.*, 2004; Bardot, 2000).

Figure 47 shows how T_{eq} of the deposits varies with distance from the volcanic vent. It would be logical for T_{eq} to decrease away from the vent because more heat loss will occur as flow durations increase (flows that are longer temporally, are longer spatially). This is due to air ingestion and heat transfer from the hot continuous phase (lava and gas) to the colder lithics. The correlation is weak and opposite to the expected sense. McClelland *et al.* (2004) reported a negative correlation between

distance and temperature for the non-welded Taupo (New Zealand) ignimbrite (1.8ka). The earlier erupted portions of the flow were cooler (by ~200°C) than the later-erupted portions which travelled further. They attribute this cooling of the early material, primarily to the mixing with lake water while mixing with air was of only secondary importance. No bodies of water could have caused such cooling in this case, but perhaps with more data points, over a larger transect, a stronger correlation may become apparent.
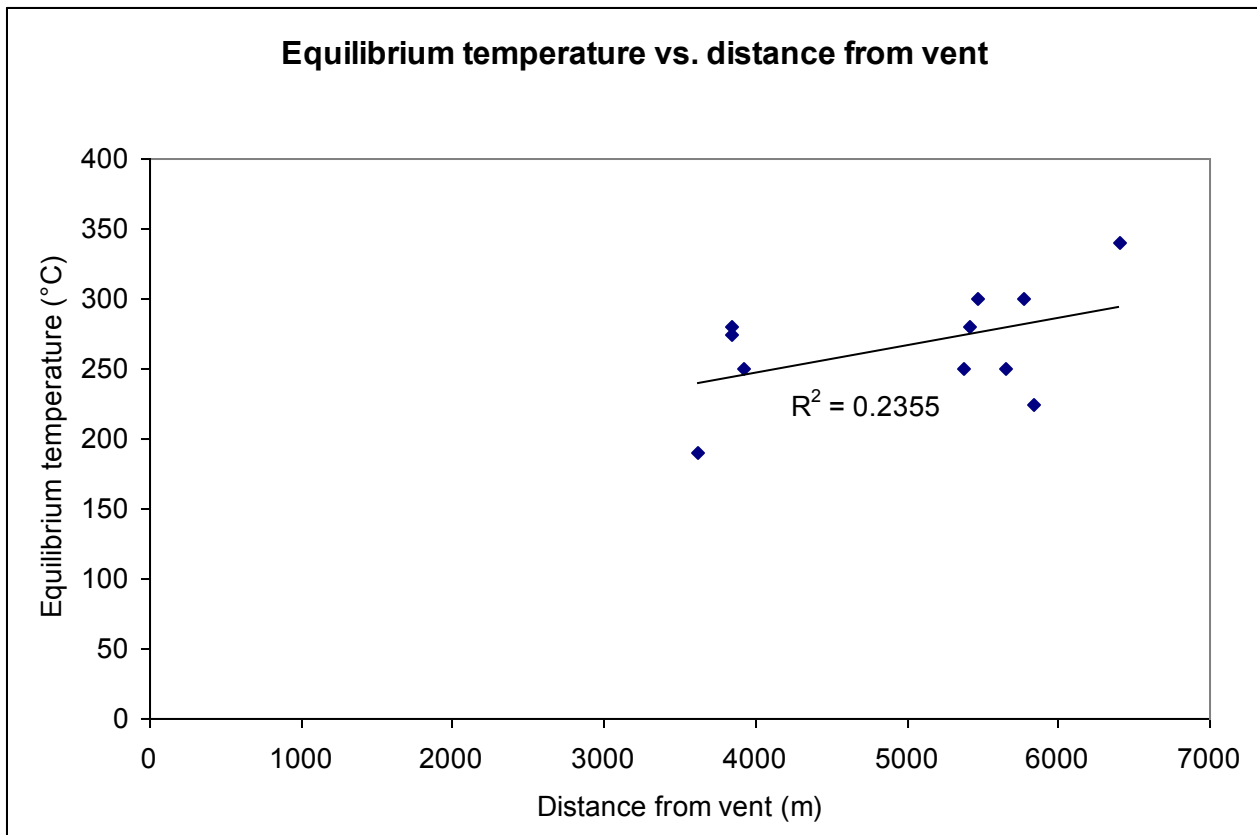

Figure 47: Estimated equilibrium temperatures of each site plotted as a function of distance of the site from the vent.

5.4 Flow regimes

During the ascent of a gas-pyroclast mixture, substantial air ingestion occurs at the top of the gas thrust region (Sparks *et al.*, 1997). The entrainment of air within collapsing columns is not fully understood, but an upper limit to the amount of air that can be ingested can be calculated from the model of Dobran *et al.* (1993). Air ingestion during a pyroclastic flow is described by the Richardson

number (R_i), which is the ratio between the buoyancy and the kinetic energy of the flow. Air ingestion is highly effective during supercritical flows, which are characterised by high velocities and $R_i < 1$. From such currents there is progressive deposition of material from the cloud, and continuous turbulent engulfment of air, which causes the cloud's density to decrease. A supercritical current is thus maintained. Supercritical ash flows show a temperature decrease with run-out distance, whereas subcritical currents do not (or to a lesser extent) (Bursik & Woods, 1996). In subcritical currents, R_i >1 and there is negligible entrainment of air, thus temperature and volume flux remain approximately constant along the length of the flow. The fact that Figure 47 does not show a strong, or even expected correlation could mean that these deposits were formed from subcritical flows, or the distances involved are too small to show a marked decrease (over a flow of 10km, a decrease of 150°C can be observed). The total mass of ingested air can be on the same order of magnitude as the transported solids in a pyroclastic flow (Bursik & Woods, 1996) and so should play an important role in the thermal history of an eruption cloud.

5.5 The role of external water

The involvement of external water during pyroclastic flows can be the most important factor that controls the thermal evolution of the flow. The specific heat capacity of water (both liquid and vapour) is much larger than that of magma, and coupled with its very high latent heat of vaporisation, water-magma interactions are the most efficient method of reducing the temperature of an erupting cloud (Koyaguchi & Woods, 1996). Complete vaporisation of only a few weight percent of liquid water can cool a pyroclastic density current by hundreds of degrees. External water can also interact with a deposit that is still hot, either as rainfall or as moisture released by a heated substrate. In these cases, it will be the main factor controlling the cooling rate of the deposit. If significant amounts of water are involved, the deposits may be reworked to form mudflows and lahars, which are essentially cold deposits.

5.6 Deposit thickness

In the absence of water, the cooling history after deposition will depend on the thickness of the deposit, which is a measure of the accumulation rate (Sparks & Wright, 1979; Riehle *et al.*, 1995; Miller, 1990). Rapid accumulation inhibits the cooling of clasts during fallout and promotes fast burial and therefore insulation. Riehle *et al.* (1995) explain that the time a thick deposit takes to cool (generally days – months, but near-emplacement temperatures can persist for tens of years in the interiors of very thick deposits) is much longer than for a thin deposit (hours). The timescale for experimental thermal demagnetisation (a supposed analogue of the natural magnetisation process, in reverse) is generally minutes or hours, and so the estimated values of T_{empl} that are obtained should be more accurate for clasts within thin deposits.

The deposits sampled in this study were less than 10m thick and so would be classed as thin deposits. However, measured surface temperatures one week after the eruptions were in excess of 200°C and so cannot have cooled on a timescale of hours. It is possible that clasts from different levels record variations in temperatures through the deposits. Heat loss to the surroundings is greater closer to the surface, but this depth dependent effect may only be noticeable in thicker deposits. Figure 48 plots emplacement temperature against the depth of the clast within the deposit. No gradation is found, however, the range of data is skewed towards the shallowest clasts. It may be more accurate to plot temperature against the depth, as a function of the total thickness of the deposit, but it seems likely that any variation in T_{empl} of clasts with depth will only be seen in thicker deposits with greater volumes.
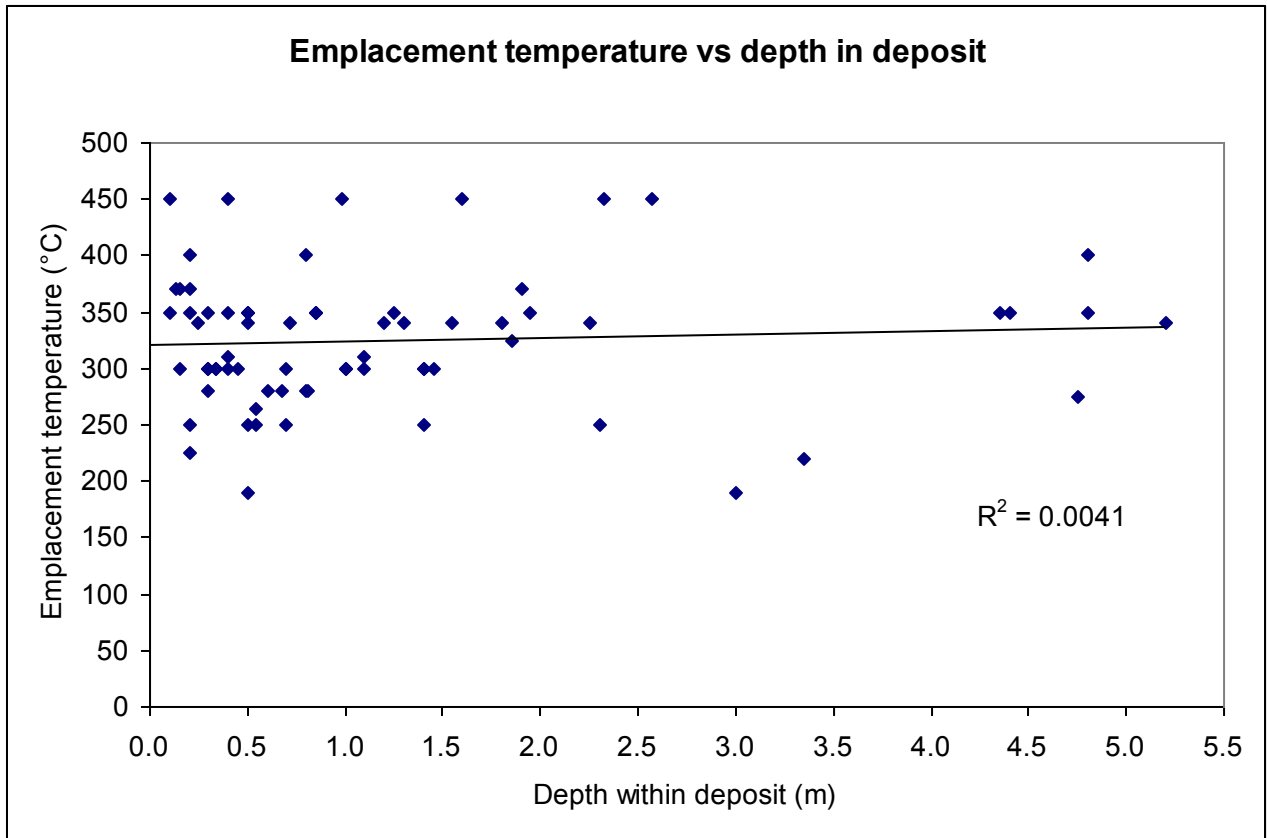
Figure 48: Estimated emplacement temperature of clasts plotted as a function of their depth in the deposit.

5.7 Low-T_B directions

Ideally, the low-T_B components of TRM carried by lithic clasts should have directions that approximate that of the Earth's magnetic field at the locality, at the time of deposition. It is therefore expected that these clasts show low-T_B components that cluster significantly around a direction of north and down. The results do not fulfil these expectations. The low-T_B components consistently group in directions that are not the same as that of the locality's magnetic field. Normally, in cases where low-T_B directions are not parallel to the geomagnetic field, one may assume that the deposits have moved (eg in a landslide), but then even the low-T_B vectors do not group, which is not the case here.

5.8 Self-reversal

A possible explanation for this problem is that these lithic fragments possess a rare trait, known as self-reversal of TRM. A phase of intermediate composition preserved in rapidly chilled dacitic pyroclastic rocks can have the property of acquiring self-reversed thermoremanent magnetisation (Uyeda, 1958; Heller *et al.* 1986; Hoffman, 1992). This phase is thought to be a titanohaematite ($Fe_y^{2+}Fe_{2-2y}^{3+}Ti_y^{4+}O_3^{2-}$) with a relatively low value of *y* (Carmichael, 1961). However, this phenomenon has only been documented in a very small number of cases, eg: andesitic pumices from the 1985 eruption of Nevado del Ruiz, Columbia (Heller *et al.*, 1986), and the original case of dacites from Mount Haruna in Japan (Nagata, 1952).

The mineral responsible for this self-reversal is a member of the ilmenite-haematite solid solution series [$xFeTiO_3$-$(1-x)Fe_2O_3$] and is intrinsic to members with a range of composition near the centre of the series ($0.60 > x > 0.45$) (Uyeda, 1955; Uyeda, 1958). The phenomenon is thought to result from some form of antiparallel spin coupling between coexisting cation-ordered and cation-disordered phases, where the T_C of the disordered phase is higher than that of the ordered phase. During cooling, the weakly-magnetic, disordered phase is the first to be magnetically ordered. After further cooling through the T_C of the strongly-magnetic, ordered phase, the ferromagnetic moment is forced (by superexchange) to align in the opposite direction (Hoffman, 1992). If this phenomenon were to be the reason for the odd directions exhibited by the low-T_B components in this study, they should have directions of approximately south and up (180° difference from north and down). Such directions, however, are shown by only five out of the eleven sites (sites 2, 4, 9, 10, 11). If these minerals are the major remanence carriers, the results from the high-temperature susceptibility measurements should suggest their presence, but it has already been seen that titanomagnetites rather than titanohaematites are the magnetic minerals within these clasts, this explanation therefore seems unlikely.

5.9 Remobilisation

Another, perhaps more likely explanation of the low-T_B directions can be proposed. Once the deposits cooled, it is possible that the flows were remobilised and moved as a coherent mass so that all the low-T_B vectors of the lithic clasts at a particular site were transformed equally to produce their clustering. This remobilisation may have been caused by settling of the deposits, or by landslides induced by heavy rainfall or movement of the land during subsequent eruptions.

5.10 Pre-eruptive conditions

Emplacement temperatures of clasts within pyroclastic deposits help constrain models of their flows, and other studies can help model other aspects of a volcano's development and activity. For instance, the geochemical signature of rocks and minerals in the juvenile component of deposits can be used to reconstruct the pre-eruptive conditions of magma and thus better understand the causes of an eruption. Mora *et al.* (2002) studied samples from the 1998 - 2000 pyroclastic flow deposits and an eastern lava flow front at Volcán de Colima. These samples were two-pyroxene andesites dominated by a mineral assemblage of: plagioclase, clinopyroxene, orthopyroxene, titanomagnetite, ilmenite, reacted amphibole and resorbed quartz. They conclude that the magma that contained these mineral phases was at a temperature of ~900°C, an oxygen fugacity of $10^{-11.1}$ and was water-undersaturated prior to the eruption. The magma originated from the mixing of two andesitic magmas with different silica contents, degrees of evolution and crystal contents.

5.11 Future work

These results can help model the characteristics of both eruptions at Volcán de Colima and volcanoes which undergo similar cycles and processes. These data come from modern deposits and therefore many of the processes (alteration, movement, tectonic disturbances) that cause secondary overprinting or obscuring of magnetic remanences should be less important than in ancient deposits and the results

should thus have greater fidelity. Temperature data collected shortly after the eruptions allows the results gained from the TRM procedure to be compared, or indeed further constrained. If modern eruptions can be more fully understood and modelled, similar work for older deposits should become ever more accurate.

During the fieldwork, an additional two sites were visited, from where more lithic clasts were sampled. Unforeseen circumstances meant that these samples have not yet been thermally demagnetised and analysed. These sites were within the deposits of an earlier eruption, in 2004, and so the results should provide a good opportunity to draw comparisons, perhaps finding similarities and differences in the characteristics of the two eruptions.

Something that was not carried out here, but might be interesting to investigate is the influence of the size of lithic clast on the estimated T_{empl}. It is expected that larger clasts are harder to heat than smaller ones of otherwise similar characteristics. If clasts of similar mineralogy, but with varying sizes were gathered at each site, this could perhaps be determined. Any thermal gradients across the larger clasts may also be observed, helping understand the dynamics of heat flow before and after emplacement.

6. CONCLUSION

The results of this study show that the T_{eq} of the July 2005 deposits at Volcán de Colima range from between 190°C and 340°C. These estimates are in good agreement with temperatures measured at the deposits, shortly after their emplacement and with results gained from previous work on similar deposits. However, the method of estimating emplacement temperatures of pyroclastic deposits by palaeomagnetic means, dictates that the low-T_B components of magnetic remanence are statistically grouped parallel to the ambient field, whilst the high-T_B components should be randomly orientated.

This behaviour is not displayed by the clasts analysed. Most sites have low-T_B components that cluster, but not in the direction of the current geomagnetic field and many sites have high-T_B components that appear to be grouped. Normally, if low-T_B components do not display the direction of the geomagnetic field, it can be assumed that the deposit has shifted since it cooled, but in such a case, even the low-T_B components should be ungrouped.

There is a small possibility that these clasts are displaying a rare characteristic of self-reversal, but only two of the sites have the correct grouping and non-grouping of the relevant components of remanence, and have low-T_B directions that are 180° away from that of the ambient field. The chance that these rocks fall into the correct compositional range that this rarely documented phenomenon requires, seems to be slim, and is not suggested by high-temperature susceptibility results.

The only satisfactory explanation of these spurious directions that can be proposed is post-cooling remobilisation of the deposits as coherent masses. However, the non-ideal behaviour of the remanence components does raise the question of how reliable these temperature estimates really are. Could it be just coincidence that these estimates fall in the expected range? Their sensible values, consistency between sites and the grouping of low-T_B directions suggest not.

Whether or not, these actual results provide any real and useful conclusions, this style of work does provide a greater understanding of Volcán de Colima, and other volcanoes with the same general characteristics. The flows on which this work focuses, erupted recently and so there is no published literature which deals with the particular eruptions, however in time the information illustrated by their equilibrium temperatures will constitute part of the body of work that helps to constrain the style of the volcano's activity. This will in turn help to monitor and predict future eruptions, and help the authorities in providing accurate, informed decisions about planning and development in areas close

to the volcano, and for the formulation of well-planned and executed evacuation procedures, when necessary.

7. ACKNOWLEDGEMENTS

The author would like to thank her supervisor, Conall Mac Niocaill for all his help, support and guidance. Thanks are extended to Dr Mac Niocaill, Dr Muxworthy and Mr Paterson for undertaking the fieldwork.

8. REFERENCES

Allan, J.F., 1986. *Geology of the Northern Colima and Zacoalco Grabens, southwest Mexico: Late Cenozoic rifting in the Mexican volcanic belt.* Geological Society of America Bulletin **97**: 473-485.

Aramaki, S. & Akimoto, S., 1957. *Temperature estimation of pyroclastic deposits by natural remanent magnetism.* American Journal of Science **255**: 619-627

Barberi, F., Cioni, R., Rosi, M., Santacroce, R., Sbrana, A. & Vecci, R., 1989. *Magmatic and phreatomagmatic phases in explosive eruptions of Vesuvius as deduced by grain-size and component analysis of the pyroclastic deposits.* Journal of Volcanology and Geothermal Research **38**: 287-307.

Bardot, L., 2000. *Emplacement temperature determinations of proximal pyroclastic deposits on Santorini, Greece, and their implications.* Bulletin of Volcanology **61**: 450-467.

Bursik, M.I. & Woods, A.W., 1996. *The dynamics and thermodynamics of large ash flows.* Bulletin of Volcanology **58**: 175-193.

Butler, R.F., 1992. *Paleomagnetism: magnetic domains to geologic terranes*. Blackwell Scientific

Carmichael, C.M., 1961. *The magnetic properties of ilmenite-haematite crystals.* Proceedings of the Royal Society of London. Series A, Mathematical and Physical Sciences **263**: 508-530.

Cas, R.A.F. & Wright, J.V., 1987. *Volcanic Successions. Modern and Ancient.* Allen & Unwin, London.

Cioni, R., Gurioli, L., Lanza, R. & Zanella, E., 2004. *Temperatures of the A.D. 79 pyroclastic density current deposits (Vesuvius, Italy).* Journal of Geophysical Research **109**: B02207.

Crandell, D.R., 1971. *Postglacial lahars from Mount Rainier volcano, Washington.* U.S. Geological Survey Prof. Paper **677**: 1-75.

De la Cruz-Reyna, S., 1993. *Random patterns of occurrence of explosive eruptions at Colima Volcano, Mexico.* Journal of Volcanology and Geothermal Research **55**: 51-68.

Dekkers, M.J., 1988. *Magnetic properties of natural pyrrhotite Part I: Behaviour of initial susceptibility and saturation-magnetization-related rock-magnetic parameters in a grain-size dependent framework.* Physics of the Earth and Planetary Interiors **52**: 376-393.

Dobran, F., Neri, A. & Macedonio, G., 1993. *Numerical simulations of collapsing eruption columns.* Journal of Geophysical Research **98**: 4231-4259.

Dobran, F. & Papale, P., 1993. *Magma-water interaction in closed systems and application to lava tunnels and volcanic conduits.* Journal of Geophysical Research **98**:14, 041-14,058.

Druitt, T.H., 1998. *Pyroclastic density currents.* In: The *physics of explosive volcanic eruptions.* (Eds. Gilbert, J.S. & Sparks, R.S.J.) Geological Society, London, Special Publications **145**: 145-182.

Fisher, R., 1953. *Dispersion on a sphere.* Proceedings of the Royal Society of London. Series A, Mathematical and Physical Sciences **217**: 295-305.

Fisher, R.V. & Schmincke, H.-U., 1984. *Pyroclastic Rocks.* Springer, Berlin.

Global Volcanism Program: www.volcano.si.edu

Gurioli, L., 2000. *Pyroclastic flow: classification, transport and emplacement mechanisms.* Plinius **23**: 84-89.

Heller, F., Carracedo, J.C. & Soler, V., 1986. *Reversed magnetisation in pyroclastics from the 1985 eruption of Nevado del Ruiz, Colombia.* Nature **324**: 241-242.

Hoblitt, R.P., Reynolds, R.L. & Larson, E.E., 1985. *Suitability of nonwelded pyroclastic-flow deposits for studies of magnetic secular variation: A test based on deposits emplaced at Mount St. Helens, Washington, in 1980.* Geology **13**: 242-245

Hoffman, K.A., 1992. *Self-reversal of thermoremanent magnetisation in the ilmenite-hematite system:order-disorder, symmetry, and spin alignment.* Journal of Geophysical Research **97**: B10,883-B10,895.

http://mceer.buffalo.edu/publications/bulletin/96/10-01/jan96f1.html

Kent, J.T., Briden, J.C. & Mardia, K.V., 1983. *Linear and planar structure in ordered multivariate data as applied to progressive demagnetisation of palaeomagnetic remanence.* Geophysical Journal of the Royal Astronomical Society **75**: 593-621.

Koyaguchi, T. & Woods, A.W., 1996. *On the formation of eruption columns following explosive mixing of magma and surface-water.* Journal of Geophysical research **101**: B5561-B5574.

Luhr, J.F., 2002. *Petrology and geochemistry of the 1991 and 1998-1999 lava flows from Volcán de Colima, Mexico: implications for the end of the current eruptive cycle.* Journal of Volcanology and Geothermal Research **117**: 169-194.

Luhr, J.F. & Carmichael, I.S.E., 1980. *The Colima volcanic complex Mexico I. Post-caldera andesites from Volcán Colima.* Contributions to Mineralogy and Petrology **71**:343-372.

Luhr, J.F., 1981. *Colima: history and cyclicity of eruptions.* Volcano News **7**:1-3.

Luhr, J.F. & Carmichael, I.S.E., 1990. *Petrological monitoring of cyclical eruptive activity at Volcán Colima, Mexico.* Geology of Volcán de Colima. Journal of Volcanology and Geothermal Research **42**: 235-260.

Luhr, J.F., Nelson, S.A. & Carmichael, I.S.E., 1985. *Active rifting in southwestern Mexico - manifestations of an incipient eastward spreading ridge jump.* Geology **13**: 54-57.

Macdonald, G.A., 1972. *Volcanoes.* Prentice-Hall, Inc., Englewood Cliffs, N.J., 1-510.

Marti, J., Diezgil, J.L. & Ortiz, R., 1991. *Conduction model for the thermal influence of lithic clasts in mixtures of hot gases and ejecta.* Journal of Geophysical Research **96**: 21,879-21,885.

Medina, F., De la Cruz, S. & Mena, M., 1983. *El Volcán de Colima.* Instituto de Geofisica, UNAM, reporte: 11-18.

McClelland, E. & Druitt, T.H., 1989. *Palaeomagnetic estimation of emplacement temperatures of pyroclastic deposits on Santorini, Greece.* Bulletin of Volcanology **51**: 16-27.

McClelland, E., Wilson, C.J.N. & Bardot, L., 2004. *Palaeotemperature determinations for the 1.8-ka Taupo ignimbrite, New Zealand, and implications for the emplacement history of a high-velocity pyroclastic flow.* Bulletin of Volcanology **66**: 492-513.

Miller, T.F., 1990. *A numerical model of volatile behaviour in non-welded cooling pyroclastic deposits.* Journal of Geophysical Research **95**: 19,349-19,364.

Mora, J.C., Macías, J.L., Saucedo, R., Orlando, A., Manetti, P. & Vaselli, O., 2002. *Petrology of the 1998-2000 products of Volcán de Colima, Mexico.* Journal of Volcanology and Geothermal Research **117**: 195-212.

Nagata, T., 1952. *Reverse thermo-remanent magnetism.* Nature **169**: 704-705.

Riehle, J.R., 1973. *Calculated compaction profiles of rhyolitic ash-flow tuffs.* Geological Society of America Bulletin **84**: 2193-2216.

Riehle, J.R., Miller, T.F. & Bailey, R.A., 1995. *Cooling, degassing and compaction of rhyolitic ash flow tuffs: a computational model.* Bulletin of Volcanology **57**: 319-336.

Saucedo, R., Komorowski, J.C., Macías, J.L. & Sheridan, M.F., 1997. *Modeling of pyroclastic flows generated during the 1913 eruption of Colima Volcano, Mexico.* American Geophysical Union Fall Meeting, San Francisco, CA. EOS Transactions of the American Geophysical Union, p. 823.

Saucedo, R., Macías, J.L., Sheridan, M.F., Bursik, M.I. & Komorowski, J.C., 2005. *Modeling of pyroclastic flows of Colima Volcano, Mexico: implications for hazard assessment.* Journal of Volcanology and Geothermal Research **139**: 103-115. (And references therein)

Sparks, R.S.J., 1976. *Grain size variation in ignimbrites and implications for the transport of pyroclastic flows.* Sedimentology **23**: 147-188.

Sparks, R.S.J. & Wright, J.V., 1979. *Welded air-fall tuffs.* Geological Society of America Special Paper **180**: 155-166.

Sparks, R.S.J., Bursik, M.I., Carey, S.N., Gilbert, J.E., Glaze, L., Sigurdsson, H. & Woods, A.W. (Eds), 1997. *Volcanic Plumes.* John Wiley

Torsvik, T.H., Briden, J.C. & Smethurst, M.A., 2000. Super-IAPD (Interactive Analysis of Palaeomagnetic Data).

Uyeda, S., 1955. *Magnetic interaction between ferromagnetic materials contained in rocks.* Journal of Geomagnetism and Geoelectricty **7**: 9-36

Uyeda, S., 1958. *Thermo-remanent magnetism as a medium of palaeomagnetism, with special reference to reverse thermo-remanent magnetism.* Japanese Journal of Geophysics **2**:1-123.

Van Bemmelen, R.W., 1949. *The Geology of Indonesia*. Government Printing Office, The Hague, 1A, 1-732.

Walker, G.P.L., 1974. *Volcanic hazards and the prediction of volcanic eruptions.* In: Prediction of Geological Hazards (Ed: Funnell, B.M.). Geological Society of London, Miscellaneous Paper **3**: 23-41.

Watson, G.S., 1956. *A test for randomness of directions.* Monthly Notices of the Royal Astronomical Society **7**: 160-161

Zijderveld, J.D.A., 1967. *Analysis of results*. In: *Methods in palaeomagnetism* (Eds. Collinson, D.W., Creer, K.M. & Runcorn, S.K.), Elsevier, Amsterdam, pp 254-286.

0m

Rooted horizon

Coarse ash with cm-sized lithics

Dm-sized lithics

Lithic-rich in places (30-40%)
with cm-dm sized blocks

4m

Marker horizon

Pale fine ash

Relatively fine ash with lenses of lithics
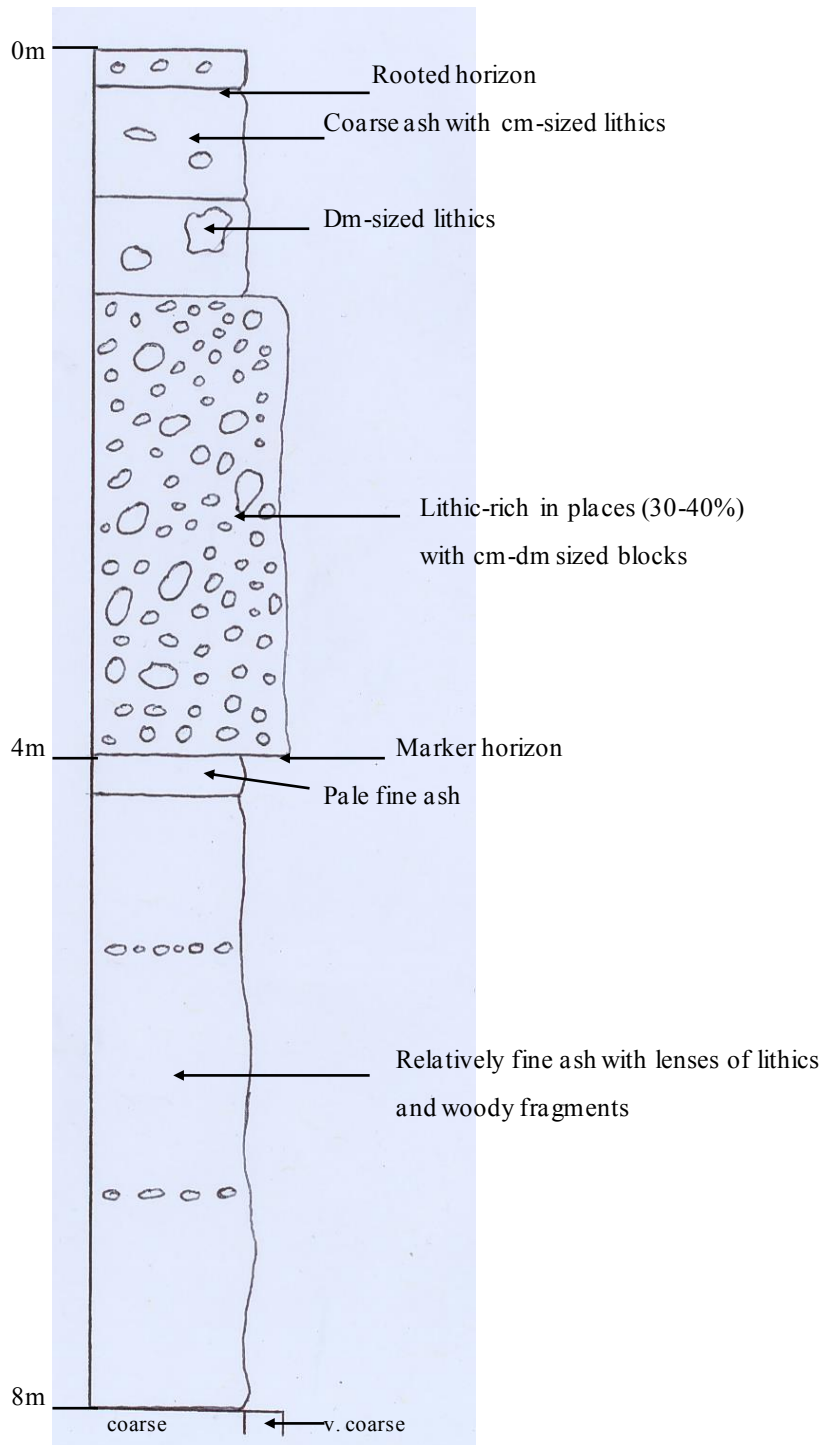and woody fragments

8m

coarse   v. coarse

Figure A1 Sketch graphic log of deposit at site 1

VC1 samples collected along here

Marker horizon

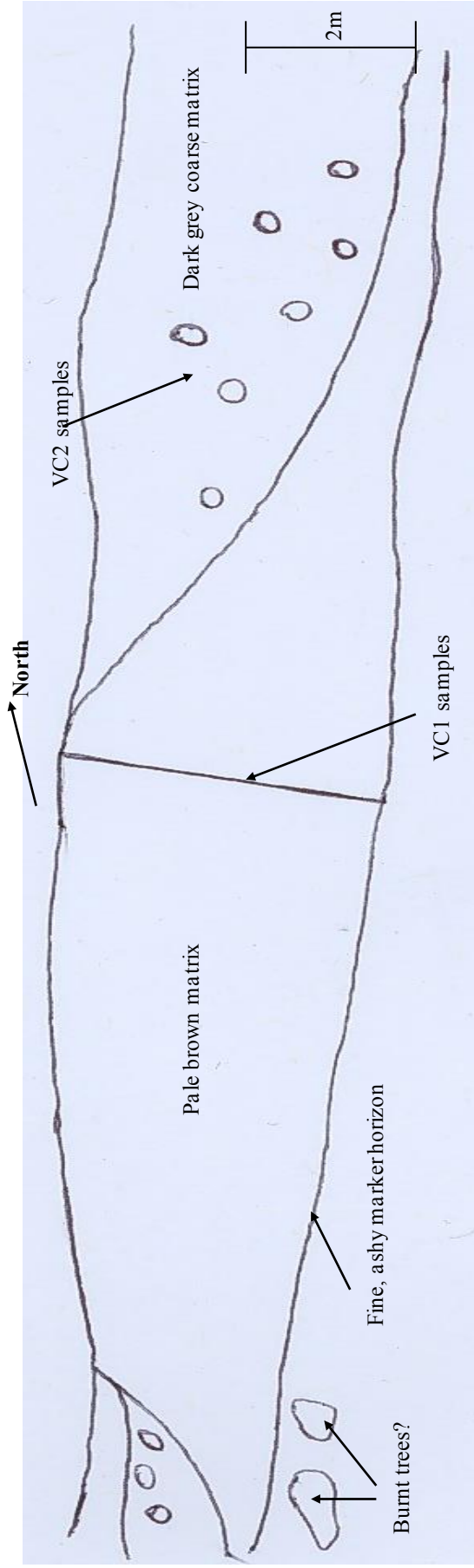**Figure A2: Site 1**
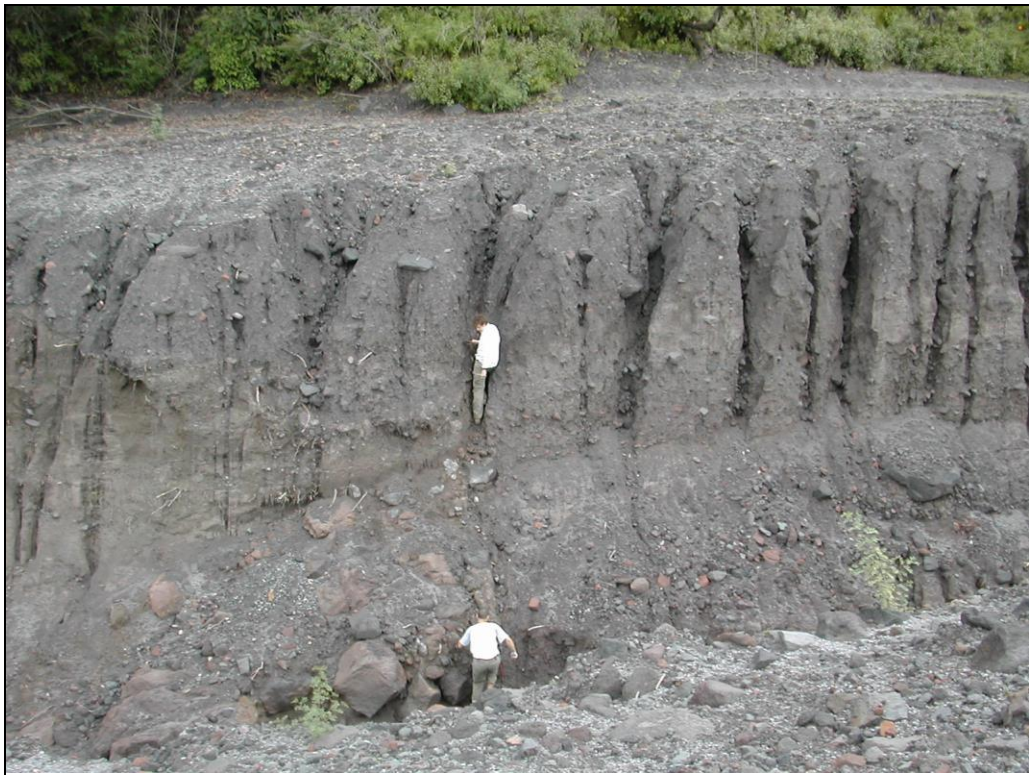
Figure A3: Site 2

Figure A4 Sketch of locality displaying sites 1 and 2

Figure A5: Site 4 with a blackened tree stump.

Figure A6: Site 5

Figure A7: Site 8. Deposit is about 3m thick. Predominantly coarse granules with lithic clasts. Does not appear particularly hot.

Figure A8: Site 9

Figure A9: Site 10

Figure A10: Site 11

APPENDIX B – FIELD DATA

Sample	Strike (°)	Dip (°)	Depth in Deposit (m)	Total deposit thickness (m)	Sample	Strike (°)	Dip (°)	Depth in Deposit (m)	Total deposit thickness (m)
VC1A	347	36	4.25	8.75	VC6A	276	41	0.68	-
VC1B	052	02	4.25	8.75	VC6B	279	56	0.54	-
VC1C	079	69	4.35	8.75	VC6C	231	87	0.13	-
VC1D	339	61	4.95	8.75	VC6D	284	47	0.10	-
VC1E	037	46	4.80	8.75	VC6E	263	41	0.89	-
VC1F	053	40	4.75	8.75	VC6F	229	60	0.72	-
VC1G	004	50	4.45	8.75	VC6G	207	44	0.52	-
VC1H	065	35	4.70	8.75	VC6H	259	35	0.68	-
VC1K	057	51	4.40	8.75	VC6K	271	55	0.98	-
VC1L	340	78	5.20	8.75	VC6L	273	61	0.41	-
VC2A	316	57	0.00	8.75	VC6M	271	81	0.30	-
VC2B	357	63	2.30	8.75	VC7A	253	79	1.00	-
VC2C	061	63	1.90	8.75	VC7B	238	60	1.10	-
VC2D	331	89	0.50	8.75	VC7C	256	61	1.20	-
VC2E	055	71	0.50	8.75	VC7D	285	59	1.40	-
VC2F	046	81	1.0	8.75	VC7E	245	58	1.40	--
VC2G	044	72	0.50	8.75	VC7F	271	58	1.60	-
VC2H	007	71	0.80	8.75	VC7G	321	38	1.10	-
VC2K	030	61	0.25	8.75	VC7H	262	16	1.30	-
VC2L	036	42	0.40	8.75	VC7K	287	86	0.20	-
VC3A	237	85	2.30	-	VC7L	307	79	0.30	-
VC3B	291	70	2.45	-	VC8A	175	82	1.80	3.00
VC3C	281	68	3.00	-	VC8B	189	72	1.95	3.00
VC3D	310	62	3.25	-	VC8C	201	89	1.85	3.00
VC3E	300	63	3.35	-	VC8D	167	38	1.80	3.00
VC3F	184	66	1.75	-	VC8E	164	62	0.85	3.00
VC3G	346	70	0.15	-	VC8F	146	38	2.25	3.00
VC3H	023	66	0.30	-	VC8G	234	60	0.60	3.00
VC3K	342	71	1.10	-	VC8H	163	55	1.40	3.00
VC3L	348	50	0.50	-	VC8K	204	70	1.65	3.00
VC4A	060	65	0.52	-	VC8L	188	80	0.70	3.00
VC4B	080	38	0.34	-	VC8M	249	50	0.30	3.00
VC4C	091	43	0.54	-	VC9A	046	66	0.30	3.00
VC4D	033	47	0.48	-	VC9B	071	90	0.25	3.00
VC4E	074	58	0.81	-	VC9C	107	24	0.10	3.00
VC4F	036	44	1.08	-	VC9D	018	74	0.85	3.00
VC4G	034	59	1.55	-	VC9E	132	64	0.20	3.00
VC4H	072	49	2.32	-	VC9F	053	36	0.40	3.00
VC4K	077	48	2.57	-	VC9G	112	67	0.30	3.00
VC4L	048	28	0.00	-	VC9H	108	75	1.25	3.00
VC5A	256	18	0.50	-	VC9K	097	75	1.20	3.00
VC5B	258	32	0.65	-	VC9L	081	66	0.80	3.00
VC5C	271	46	0.30	-	VC9M	354	64	1.45	3.00
VC5D	245	17	0.40	-	VC10A	163	25	0.30	3.00
VC5E	272	32	0.05	-	VC10B	206	38	0.50	3.00
VC5F	304	86	0.25	-	VC10C	191	64	0.40	3.00
VC5G	239	70	0.55	-	VC10D	202	74	0.15	3.00
VC5H	222	78	0.70	-	VC10E	283	60	0.20	3.00
VC5K	192	80	0.45	-	VC10F	218	89	0.70	3.00
VC5L	240	64	0.20	-	VC10G	221	57	0.40	3.00

Sample	Strike (°)	Dip (°)	Depth in Deposit (m)	Total deposit thickness (m)	Sample	Strike (°)	Dip (°)	Depth in Deposit (m)	Total deposit thickness (m)
VC10H	200	51	0.50	3.00	VC11E	307	43	0.15	3.00
VC10K	186	50	0.30	3.00	VC11F	304	52	0.15	3.00
VC10L	199	51	0.20	3.00	VC11G	022	19	0.10	3.00
VC11A	015	14	0.10	3.00	VC11H	001	52	0.20	3.00
VC11B	349	34	0.15	3.00	VC11K	018	41	0.20	3.00
VC11C	344	76	0.15	3.00	VC11L	010	51	0.25	3.00
VC11D	018	57	0.15	3.00					

Table B1 Shows the strike, depth and depth within the deposit of each lithic clast collected

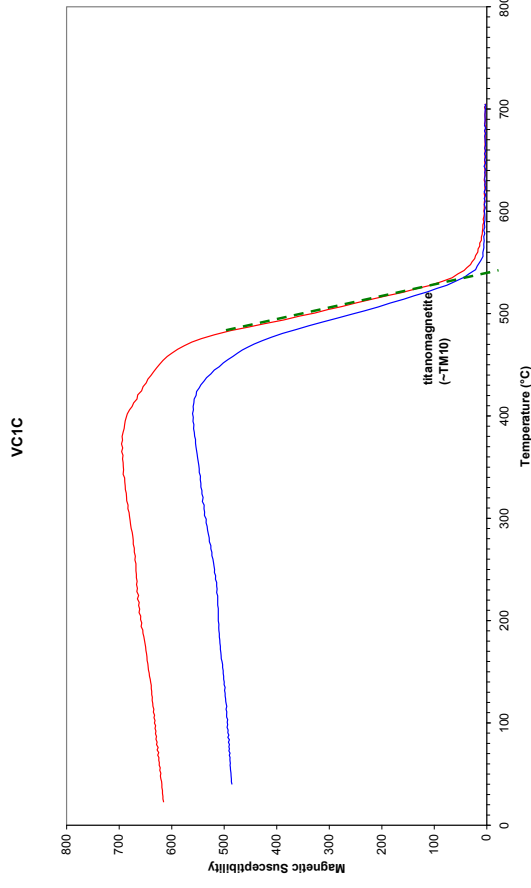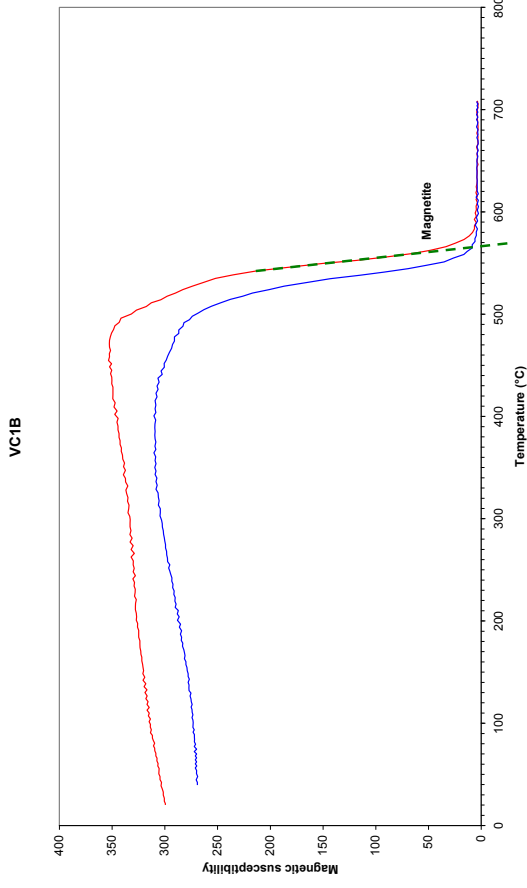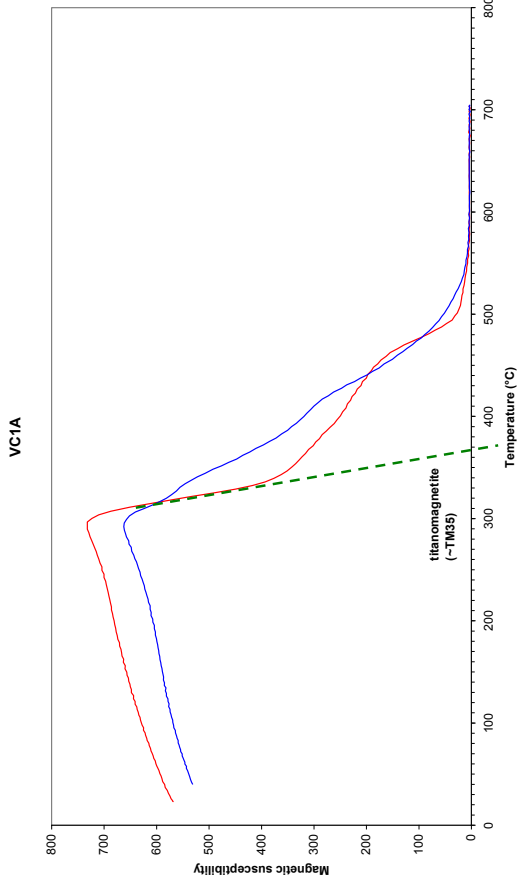# APPENDIX C – THERMAL DEMAGNETISATION DATA

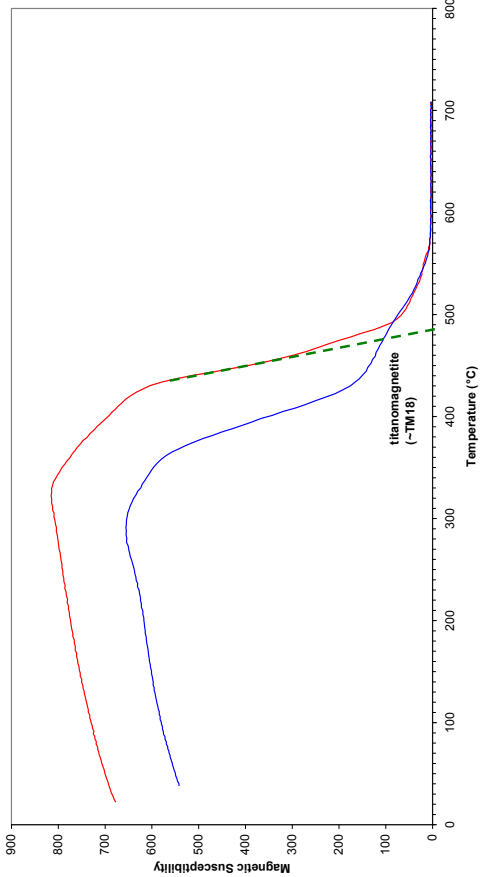| Site No.	Sample	Run No.	Low-T$_B$ component declination (°)	Low-T$_B$ component inclination(°)	Low-T$_B$ component α (°)	High-T$_B$ component declination (°)	High-T$_B$ component inclination (°)	High-T$_B$ component α (°)
1	VC1A1	-	-	-	-	-	-	-
1	VC1A2	-	-	-	-	-	-	-
1	VC1B	2	144.7	-38.1	5.1	-	-	-
1	VC1C1	1	-	-	-	228.0	48.4	7.7
1	VC1C2	-	-	-	-	-	-	-
1	VC1D1A	-	-	-	-	-	-	-
1	VC1D2	2	-	-	-	10.3	29.4	7.6
1	VC1E1	-	-	-	-	-	-	-
1	VC1E2	-	-	-	-	-	-	-
1	VC1E3	1	100.6	-31.2	15.3	97.2	-3.4	6.8
1	VC1E4	-	-	-	-	-	-	-
1	VC1E5	-	-	-	-	-	-	-
1	VC1E6	1	106.9	-37.7	12.2	96.1	-15.4	4.9
1	VC1F1	1	136.5	-42.1	14.6	76.2	-29.7	9.8
1	VC1F2	-	-	-	-	-	-	-
1	VC1G1	-	-	-	-	-	-	-
1	VC1G2	-	-	-	-	-	-	-
1	VC1H1	2	-	-	-	-	-	-
1	VC1H2	-	-	-	-	-	-	-
1	VC1K1	-	-	-	-	-	-	-
1	VC1K2A	-	-	-	-	-	-	-
1	VC1K2B	1	144.2	-36.7	8.2	121.8	30.2	11.6
1	VC1L	2	63.5	12.3	12.9	106.2	18.6	6.6
2	VC2A	-	-	-	-	-	-	-
2	VC2B1	1	-	-	-	-	-	-
2	VC2B2	2	-	-	-	-	-	-
2	VC2C	2	-	-	-	91.5	32.5	4.0
2	VC2D	-	-	-	-	-	-	-
2	VC2E1	2	143.7	-26.8	6.4	-	-	-
2	VC2E2	1	154.3	-28.9	3.1	-	-	-
2	VC2F	-	-	-	-	-	-	-
2	VC2G1	2	124.7	8.1	14.2	120.6	25.4	6.6
2	VC2G2	1	-	-	-	81.1	20.4	6.3
2	VC2H	2	-	-	-	153.3	4.1	6.1
2	VC2K	2	125.0	-25.3	6.8	181.5	22.6	10.3
2	VC2L1	1	131.1	-41.7	13.4	30.8	74.7	7.9
2	VC2L2	1	-	-	-	14.1	41.5	6.3
2	VC2L3	-	-	-	-	-	-	-
3	VC3A1	1	20.1	-1.7	8.1	3.0	7.1	2.3
3	VC3A2	-	-	-	-	-	-	-
3	VC3B1	-	-	-	-	-	-	-
3	VC3B2	-	-	-	-	-	-	-
3	VC3C	2	19.8	-12.2	11.7	7.8	16.1	3.7
3	VC3D1	1	-	-	-	-	-	-
3	VC3D2	-	-	-	-	-	-	-
3	VC3E1	-	-	-	-	-	-	-
3	VC3E2	2	39.6	-20.5	5.4	30.4	-7.1	5.0
3	VC3F1	1	-	-	-	34.5	-43.8	2.8
3	VC3F2	-	-	-	-	-	-	-
3	VC3G1	-	-	-	-	-	-	
3	VC3G2	1	-	-	-	93.0	59.4	12.3

Site No.	Sample	Run No.	Low-T$_B$ component declination (°)	Low-T$_B$ component inclination(°)	Low-T$_B$ component α (°)	High-T$_B$ component declination (°)	High-T$_B$ component inclination (°)	High-T$_B$ component α (°)
3	VC3H1	-	-	-	-	-	-	-
3	VC3H2	2	-	-	-	267.8	-13.6	3.8
3	VC3K1A	-	-	-	-	-	-	-
3	VC3K1B	-	-	-	-	-	-	-
3	VC3K2A	-	-	-	-	-	-	-
3	VC3K2B	-	-	-	-	-	-	-
3	VC3K3A	-	-	-	-	-	-	-
3	VC3K3B	-	-	-	-	-	-	-
3	VC3K4A	-	-	-	-	-	-	-
3	VC3K4B	1	78.0	-9.9	5.5	287.0	46.2	8.5
3	VC3K5A	1	74.5	-17.6	5.1	-	-	-
3	VC3K5B	-	-	-	-	-	-	-
3	VC3L1	-	-	-	-	-	-	-
3	VC3L2	-	-	-	-	-	-	-
3	VC3L3	2	84.8	-36.0	8.3	104.3	-11.1	5.8
4	VC4A	2	-	-	-	238.2	-37.5	6.3
4	VC4B1	-	-	-	-	-	-	-
4	VC4B2	-	-	-	-	-	-	-
4	VC4B3A	1	194.4	-49.4	13.0	220.6	-26.7	13.7
4	VC4B3B	-	-	-	-	-	-	-
4	VC4B4	1	174.2	-44.1	18.6	239.3	-44.3	4.8
4	VC4B5	-	-	-	-	-	-	-
4	VC4C	-	191.2	-48.7	3.4	160.3	-33.4	7.4
4	VC4D	-	-	-	-	-	-	-
4	VC4E	2	169.0	-25.0	7.8	205.0	-33.5	12.4
4	VC4F	-	-	-	-	-	-	-
4	VC4G	2	134.1	-27.1	7.1	173.7	-22.1	3.9
4	VC4H1	1	124.1	11.9	29.2	197.6	2.9	0.4
4	VC4H2A	-	-	-	-	-	-	-
4	VC4H2B	-	-	-	-	-	-	-
4	VC4K1	-	-	-	-	-	-	-
4	VC4K2	-	-	-	-	-	-	-
4	VC4K3	1	170.4	-35.3	5.5	355.4	36.7	0.7
4	VC4L	2	-	-	-	-	-	-
5	VC5A1	-	-	-	-	-	-	-
5	VC5A2	1	356.5	-59.1	4.7	-	-	-
5	VC5A3	-	-	-	-	-	-	-
5	VC5A4	1	336.3	-57.3	15.6	17.9	-54.1	2.2
5	VC5A5	-	-	-	-	-	-	-
5	VC5A6	-	-	-	-	-	-	-
5	VC5B1	2	34.6	-52.1	2.8	-	-	-
5	VC5B2	-	-	-	-	-	-	-
5	VC5C	-	-	-	-	-	-	-
5	VC5D1	-	-	-	-	-	-	-
5	VC5D2	-	-	-	-	-	-	-
5	VC5D3	1	91.0	37.6	7.5	-	-	-
5	VC5D4	-	-	-	-	-	-	-
5	VC5D5	-	-	-	-	-	-	-
5	VC5D6	1	95.1	-39.2	15.3	110.8	-42.1	12.5
5	VC5D7	-	-	-	-	-	-	-
5	VC5E1A	-	-	-	-	-	-	-
5	VC5E1B	-	183.8	-48.8	7.5	-	-	-
5	VC5E2A	-	-	-	-	-	-	-

Site No.	Sample	Run No.	Low-T$_B$ component declination (°)	Low-T$_B$ component inclination(°)	Low-T$_B$ component α (°)	High-T$_B$ component declination (°)	High-T$_B$ component inclination (°)	High-T$_B$ component α (°)
5	VC5E2B	-	-	-	-	-	-	-
5	VC5E3	2	184.2	-48.3	15.6	-	-	-
5	VC5E4	1	172.4	-40.0	19.1	-	-	-
5	VC5F1	-	-	-	-	126.1	-21.6	1.8
5	VC5F2	1	122.0	42.7	12.4	-	-	-
5	VC5F3	-	-	-	-	-	-	-
5	VC5G	-	-	-	-	-	-	-
5	VC5H	2	-	-	-	43.7	-27.8	7.4
5	VC5K1	-	-	-	-	-	-	-
5	VC5K2	1	291.1	-10.2	5.6	83.5	26.2	5.7
5	VC5L	2	331.2	-14.2	3.3	-	-	-
6	VC6A1	1	33.6	-29.2	13.0	-	-	-
6	VC6A2	-	-	-	-	-	-	-
6	VC6B	2	358.9	-38.9	9.1	345.4	-9.5	4.9
6	VC6C	2	-	-	-	17.7	35.3	11.8
6	VC6D1	1	33.4	-41.5	8.8	35.8	37.0	7.5
6	VC6D2	-	-	-	-	-	-	-
6	VC6E1	1	-	-	-	205.9	13.4	6.1
6	VC6E2	-	-	-	-	-	-	-
6	VC6F	2	319.8	-24.9	7.6	335.6	-8.0	2.1
6	VC6G	-	-	-	-	-	-	-
6	VC6H	-	6.5	-48.7	9.1	136.2	-56.2	6.9
6	VC6K1	1	17.1	-20.1	11.9	173.6	47.1	6.9
6	VC6K2	-	-	-	-	-	-	-
6	VC6K3	1	-	-	-	-	-	-
6	VC6L	-	-	-	-	-	-	-
6	VC6M	-	-	-	-	-	-	-
7	VC7A1	-	-	-	-	-	-	-
7	VC7A2	1	6.6	-20.9	14.6	14.0	28.7	8.4
7	VC7A3	1	347.1	-7.6	13.6	334.0	32.8	8.0
7	VC7B1	1	-	-	-	263.1	74.6	6.2
7	VC7B2	-	-	-	-	-	-	-
7	VC7C1	1	-	-	-	125.9	-8.3	0.5
7	VC7C2	-	-	-	-	-	-	-
7	VC7D1	-	-	-	-	-	-	-
7	VC7D2A	-	-	-	-	-	-	-
7	VC7D2B	1	25.1	-10.7	9.5	14.6	-9.9	5.1
7	VC7D3A	-	-	-	-	-	-	-
7	VC7D3B	1	25.5	-19.0	10.2	17.8	-19.3	7.4
7	VC7D4	-	-	-	-	-	-	-
7	VC7E1	-	-	-	-	-	-	-
7	VC7E2	1	350.5	-27.3	6.2	6.0	-10.7	3.9
7	VC7F	2	357.1	-19.6	6.6	118.1	21.5	7.2
7	VC7G	2	43.6	-39.2	10.0	49.9	-6.6	4.0
7	VC7H	2	160.3	17.2	20.8	179.7	27.6	6.2
7	VC7K	2	22.8	-10.1	4.3	359.6	-26.8	6.5
7	VC7L	-	-	-	-	-	-	-
8	VC8A1	-	-	-	-	-	-	-
8	VC8A2	2	294.3	-39.4	20.3	218.4	-28.4	7.0
8	VC8B1	-	-	-	-	-	-	-
8	VC8B2	1	304.7	-13.5	12.1	325.2	-49.8	6.0
8	VC8C1	-	-	-	-	-	-	-
8	VC8C2	2	335.6	10.3	14.1	7.5	-49.5	14.3

Site No.	Sample	Run No.	Low-T$_B$ component declination (°)	Low-T$_B$ component inclination(°)	Low-T$_B$ component α (°)	High-T$_B$ component declination (°)	High-T$_B$ component inclination (°)	High-T$_B$ component α (°)
8	VC8D1	-	-	-	-	-	-	-
8	VC8D2	1	-	-	-	-	-	-
8	VC8D3	2	-	-	-	-	-	-
8	VC8E	-	-	-	-	-	-	-
8	VC8F	2	277.8	-50.2	11.5	74.0	-48.3	14.7
8	VC8G1	-	-	-	-	-	-	-
8	VC8G2	2	349.6	-33.3	9.9	124.2	-38.7	12.3
8	VC8H	-	-	-	-	-	-	-
8	VC8K	-	-	-	-	-	-	-
8	VC8L	2	281.8	-11.8	9.9	242.5	-27.7	10.6
8	VC8M	2	332.2	-16.6	10.8	26.4	7.6	13.5
9	VC9A1	1	-	-	-	27.2	62.3	6.3
9	VC9A2	-	-	-	-	-	-	-
9	VC9B1	1	-	-	-	-	-	-
9	VC9B2	-	-	-	-	-	-	-
9	VC9C	-	-	-	-	-	-	-
9	VC9D1	-	-	-	-	-	-	-
9	VC9D2A	1	104.1	-16.9	13.1	192.1	-19.3	5.7
9	VC9D2B	-	-	-	-	-	-	-
9	VC9D3A	-	-	-	-	-	-	-
9	VC9D3B	-	-	-	-	-	-	-
9	VC9D4A	1	-	-	-	199.5	-25.0	7.1
9	VC9D4B	-	-	-	-	-	-	-
9	VC9E	-	-	-	-	-	-	-
9	VC9F1	-	-	-	-	-	-	-
9	VC9F2	1	254.6	-9.0	8.3	214.1	76.4	7.2
9	VC9F3	2	-	-	-	233.1	70.7	3.5
9	VC9G	-	-	-	-	-	-	-
9	VC9H1	-	-	-	-	-	-	-
9	VC9H2	1	-	-	-	252.2	37.7	5.7
9	VC9K	2	180.5	-3.4	8.3	169.7	-21.0	3.6
9	VC9L	2	193.2	-26.9	10.3	199.6	-15.2	2.3
9	VC9M1A	-	-	-	-	-	-	-
9	VC9M1B	-	-	-	-	-	-	-
9	VC9M2A	1	139.1	-10.0	11.1	158.1	-23.9	13.0
9	VC9M2B	-	-	-	-	-	-	-
9	VC9M3	-	-	-	-	-	-	-
9	VC9M4	1	115.3	18.0	7.1	-	-	-
10	VC10A1	1	219.2	-66.7	8.2	87.4	-35.0	13.7
10	VC10A2	-	-	-	-	-	-	-
10	VC10A3	-	-	-	-	-	-	-
10	VC10A4	1	-	-	-	41.5	-33.7	11.7
10	VC10B1	1	107.5	-39.5	9.3	52.3	32.3	5.0
10	VC10B2	-	-	-	-	-	-	-
10	VC10C	2	278.6	-27.4	12.9	255.6	-8.8	13.6
10	VC10D	2	295.1	-8.3	11.3	171.8	6.5	5.8
10	VC10E1	1	286.3	-57.4	14.7	98.8	-39.8	8.3
10	VC10E2A	1	-	-	-	126.2	-74.8	4.2
10	VC10E2B	-	-	-	-	-	-	-
10	VC10F1	1	323.7	12.8	10.5	338.1	13.5	4.6
10	VC10F2	-	-	-	-	-	-	-
10	VC10G	-	-	-	-	-	-	-
10	VC10H	2	-	-	-	184.6	2.8	2.8

Site No.	Sample	Run No.	Low-T$_B$ component declination (°)	Low-T$_B$ component inclination(°)	Low-T$_B$ component α (°)	High-T$_B$ component declination (°)	High-T$_B$ component inclination (°)	High-T$_B$ component α (°)
10	VC10K	-	-	-	-	-	-	-
10	VC10L1	-	-	-	-	-	-	-
10	VC10L2	1	168.0	-40.0	13.7	215.9	37.7	8.0
10	VC10L3	1	238.9	25.0	4.7	158.4	-23.1	4.9
11	VC11A1	1	271.9	-68.4	11.7	-	-	-
11	VC11A2	-	-	-	-	-	-	-
11	VC11B	2	-	-	-	26.8	28.2	3.4
11	VC11C	-	-	-	-	-	-	-
11	VC11D	-	-	-	-	-	-	-
11	VC11E1A	-	-	-	-	-	-	-
11	VC11E1B	1	-	-	-	123.6	19.6	10.9
11	VC11F1	1	-	-	-	73.6	29.6	5.1
11	VC11F2	-	-	-	-	-	-	-
11	VC11G1	1	117.2	-81.8	12.7	266.9	31.4	7.1
11	VC11G2	-	-	-	-	-	-	-
11	VC11H1	2	149.9	3.8	11.8	173.0	-49.6	4.6
11	VC11H2	-	-	-	-	-	-	-
11	VC11K1	1	134.5	-44.5	7.0	-	-	-
11	VC11K2	-	-	-	-	-	-	-
11	VC11K3	-	-	-	-	-	-	-
11	VC11K4	1	133.7	-55.8	4.8	-	-	-
11	VC11L1	-	-	-	-	-	-	-
11	VC11L2	2	110.7	-41.2	12.6	37.5	-45.9	7.0

APPENDIX D – REMAINING HIGH-TEMPERATURE SUSCEPTIBILITY RESULTS
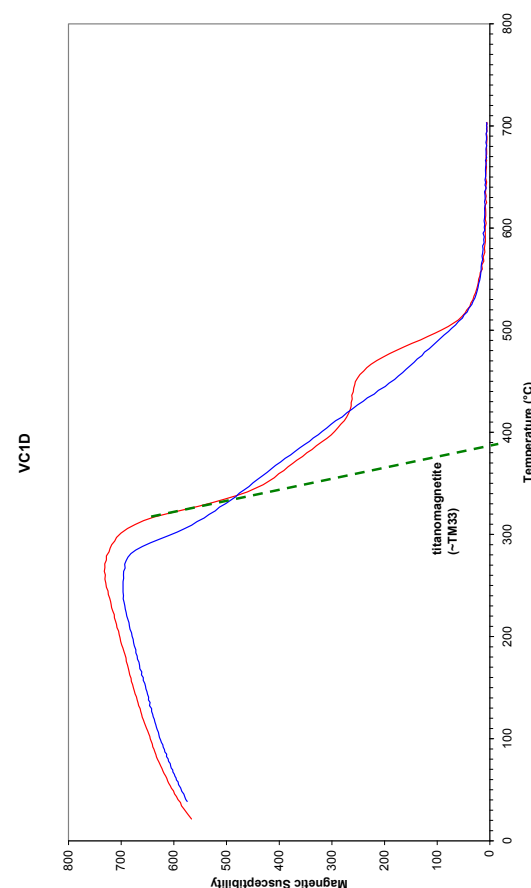
VC1F
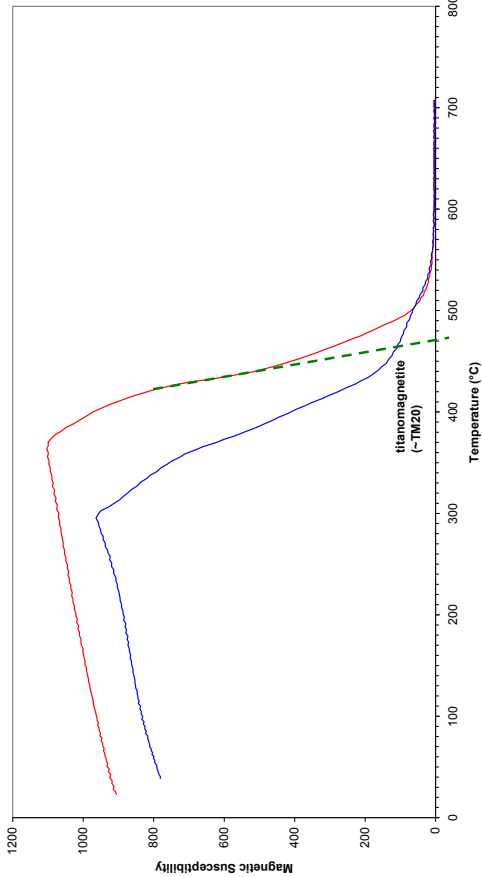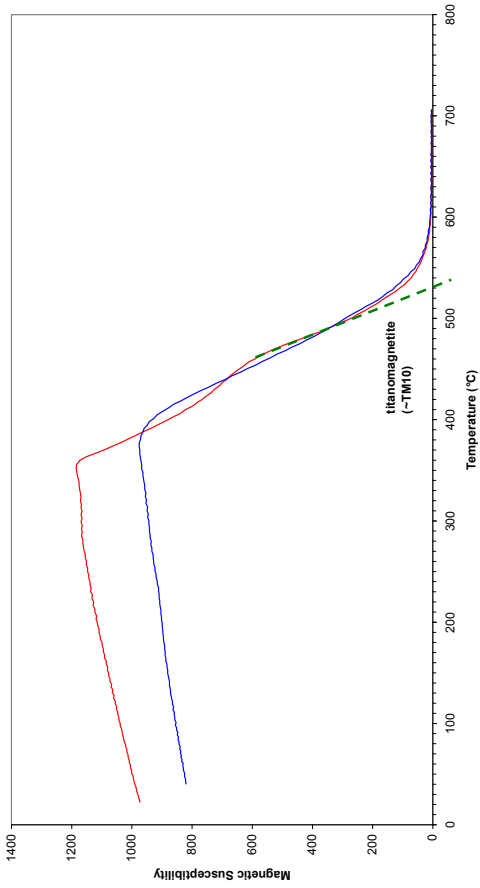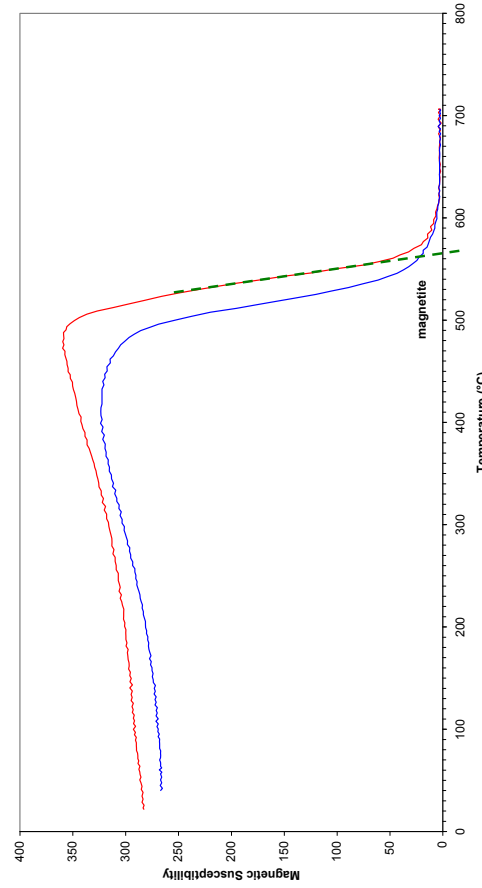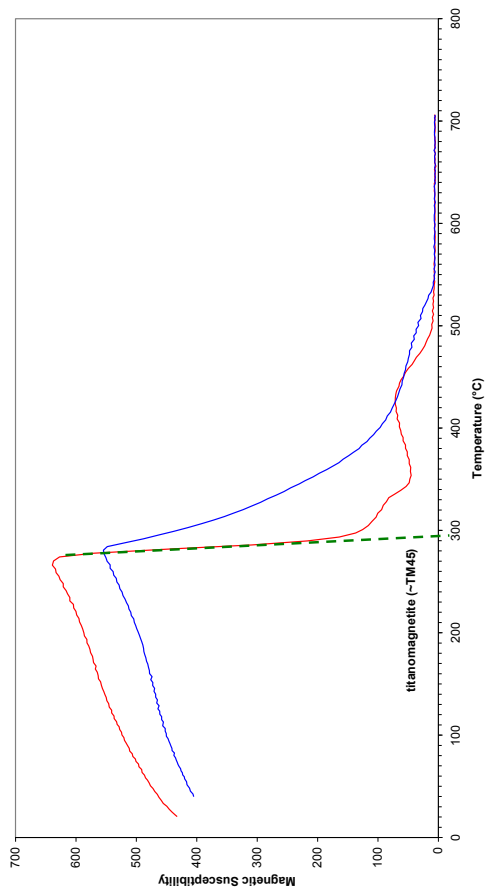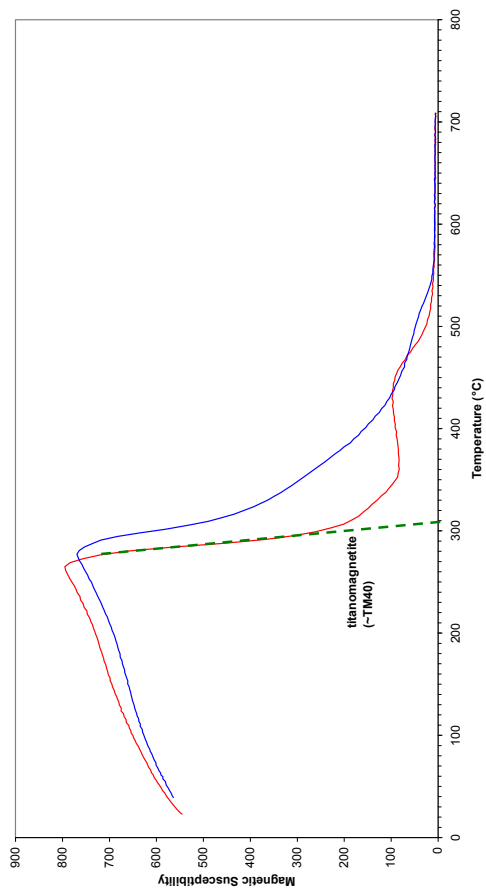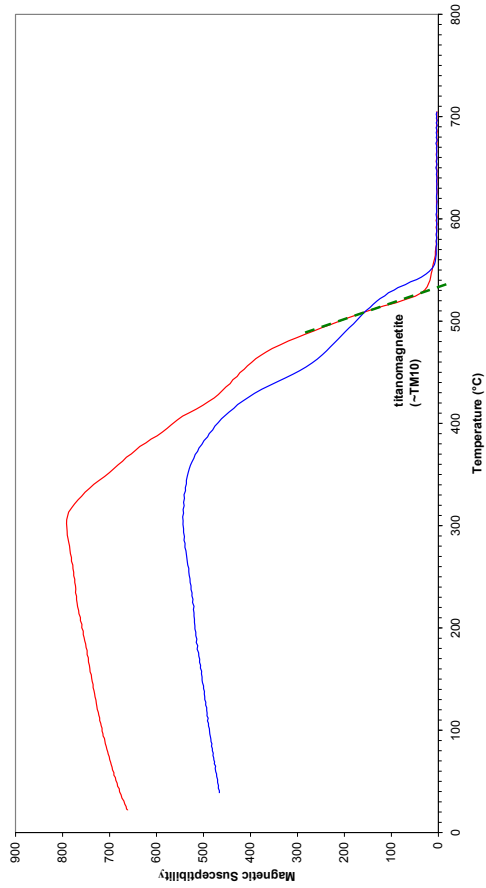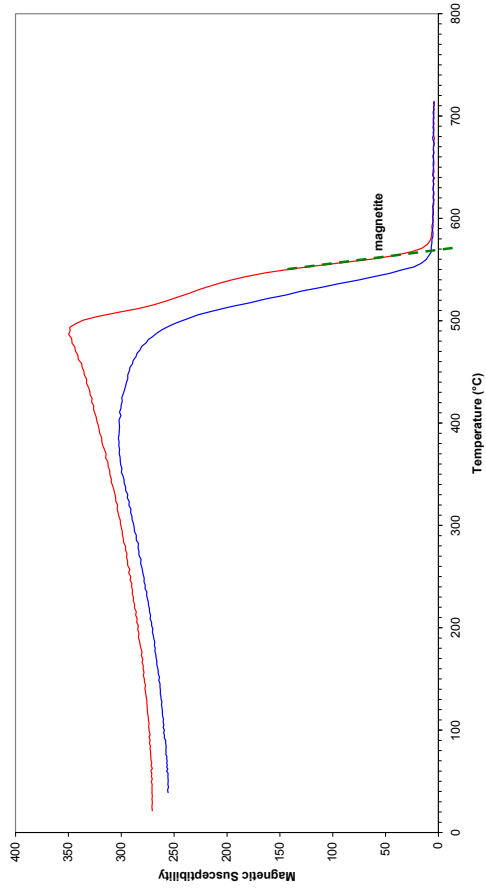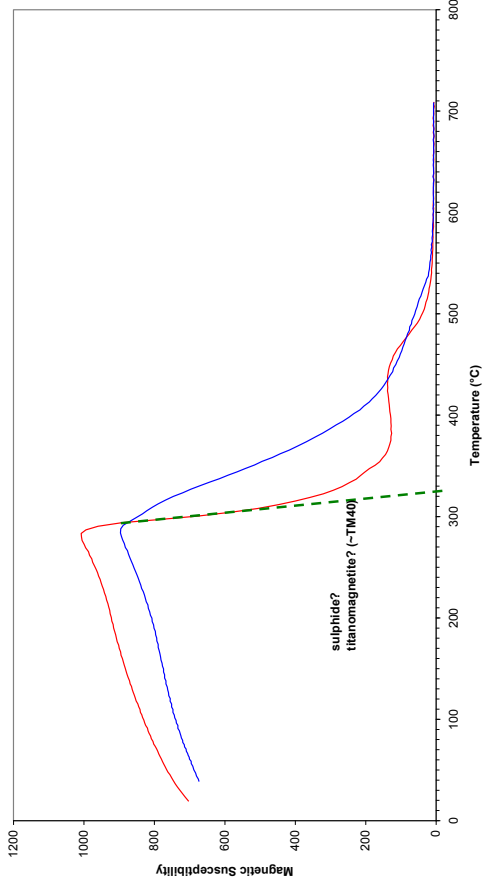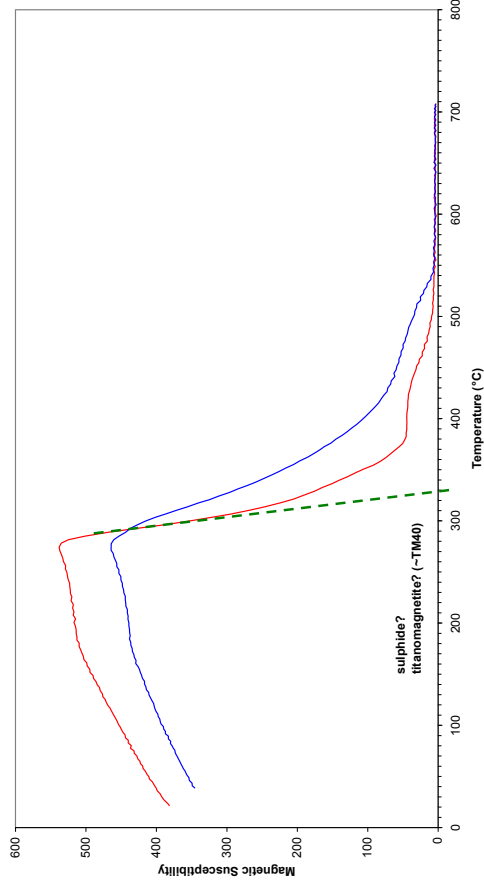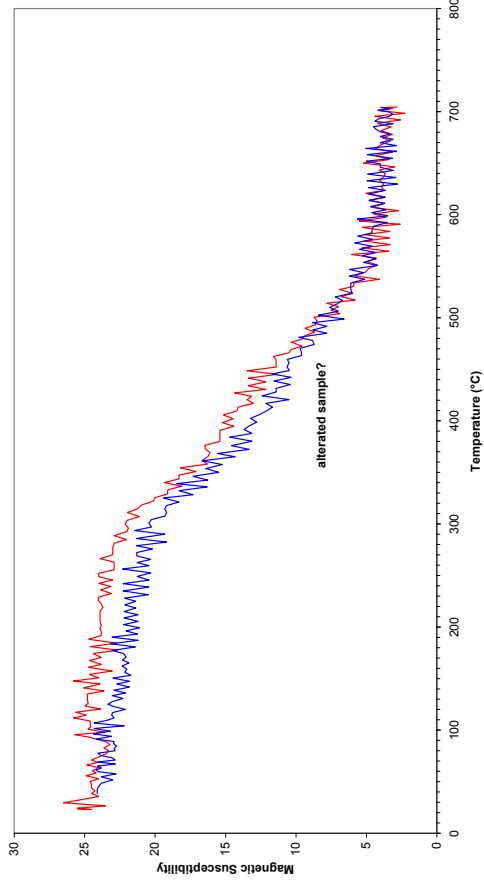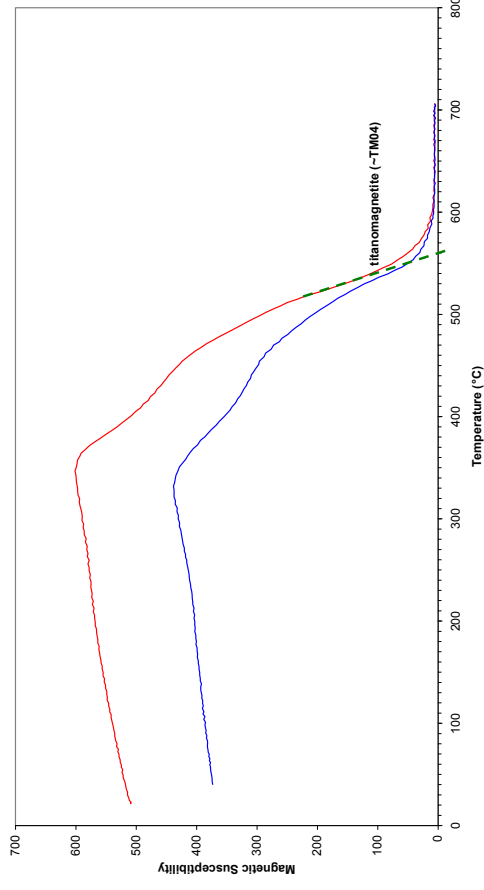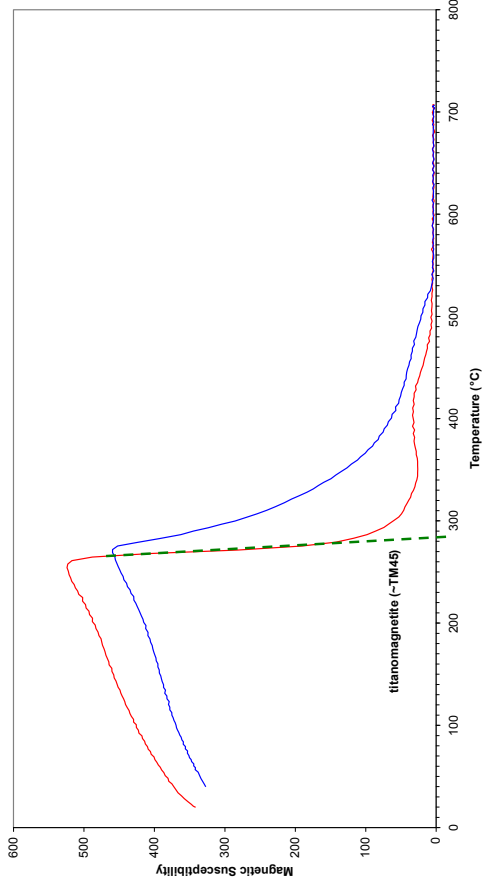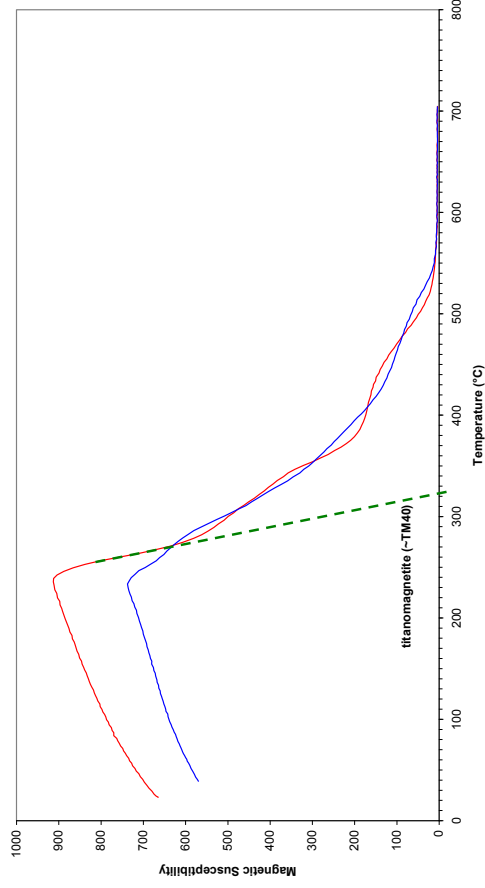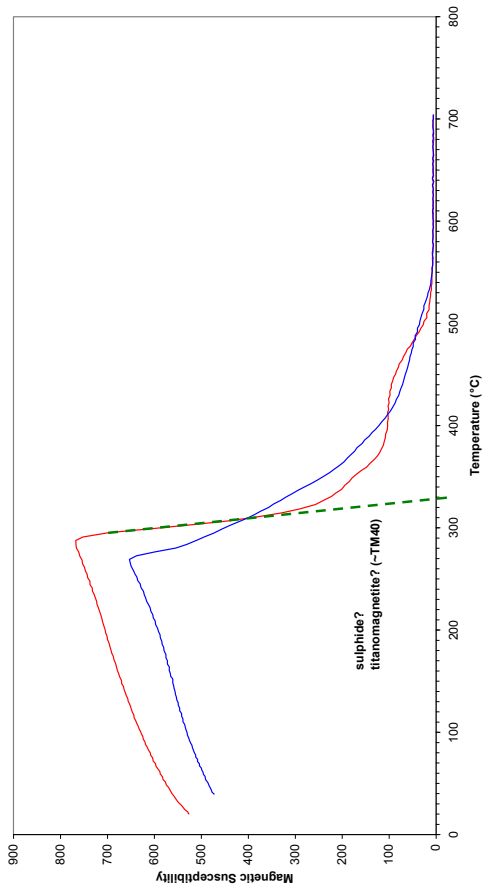
titanomagnetite
(~TM10)

Temperature (°C)

Magnetic Susceptibility

VC1G

titanomagnetite
(~TM18)

Temperature (°C)

Magnetic Susceptibility

VC1H

magnetite

Temperature (°C)

Magnetic Susceptibility

VC1K

titanomagnetite
(~TM20)

Temperature (°C)

Magnetic Susceptibility

VC5D

VC5E

magnetite

titanomagnetite (~TM05)

VC5F

VC5H

titanomagnetite (~TM04)

titanomagnetite (~TM18)

maghaemite

VC10E

titanomagnetite (~TM04)

VC11A

titanomagnetite (~TM20)

VC11F

magnetite

VC11K

titanomagnetite (~TM08)
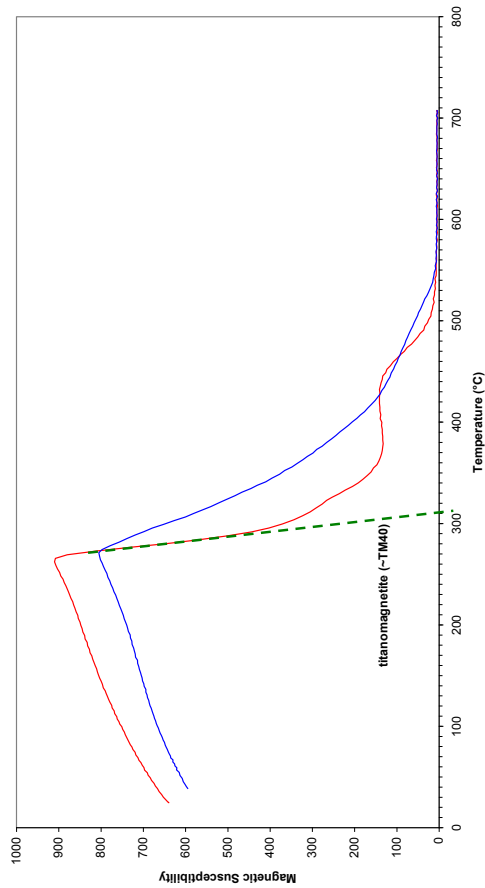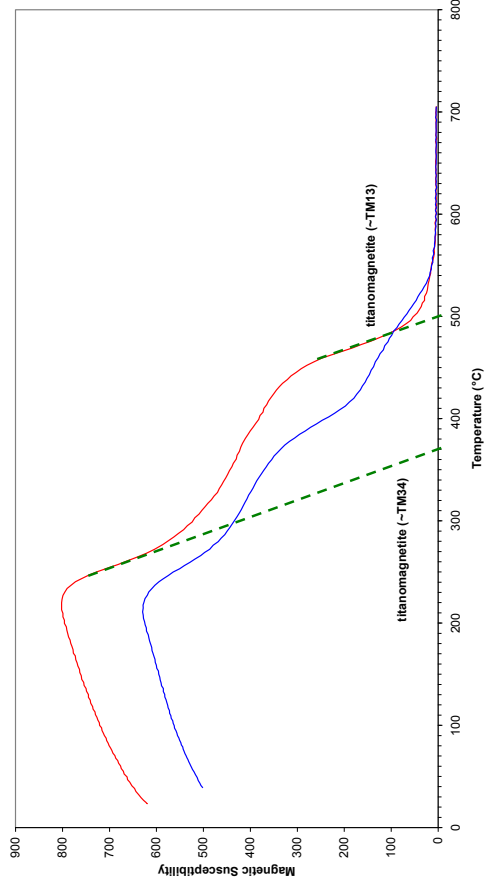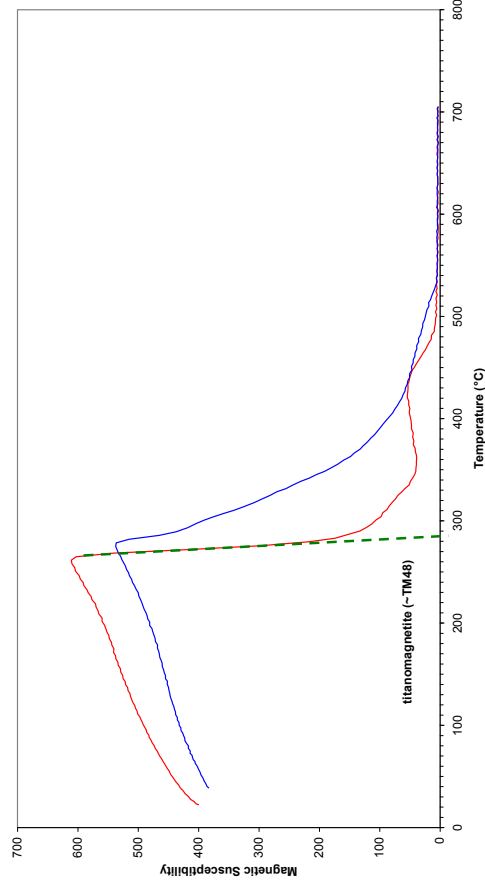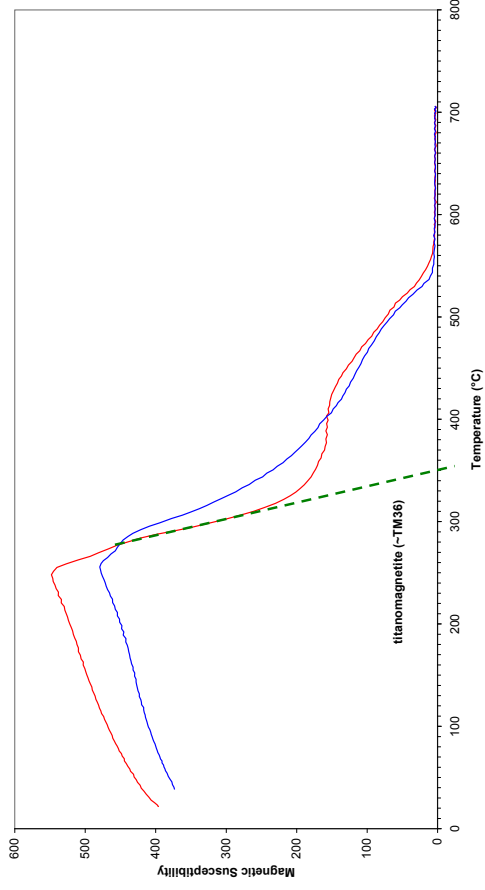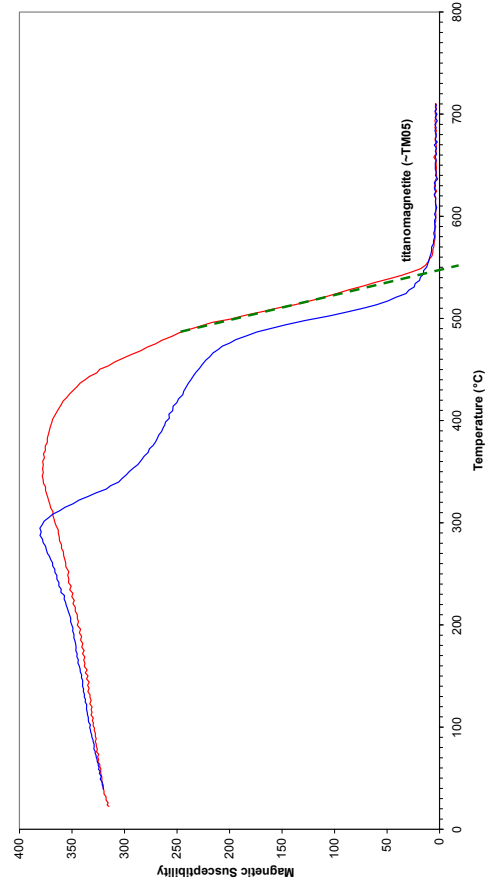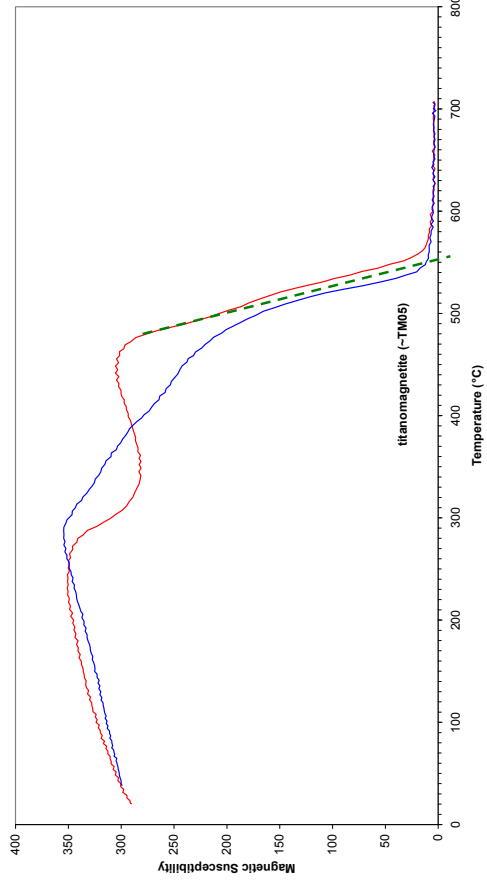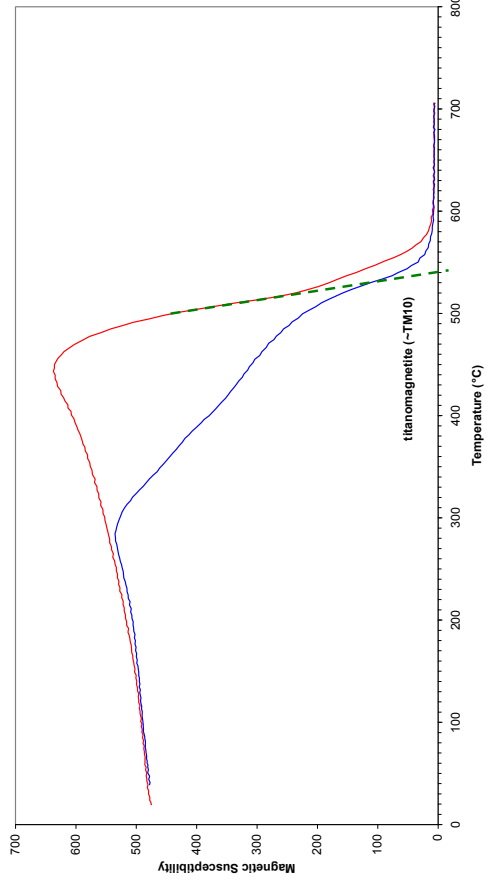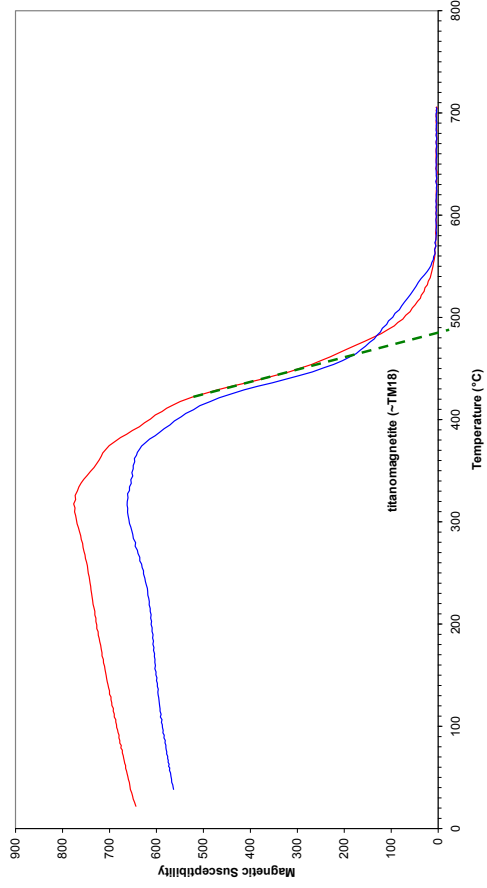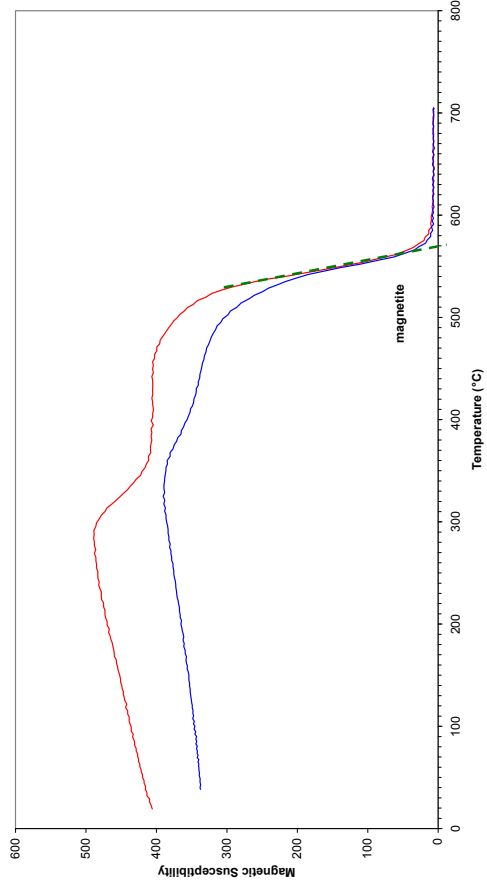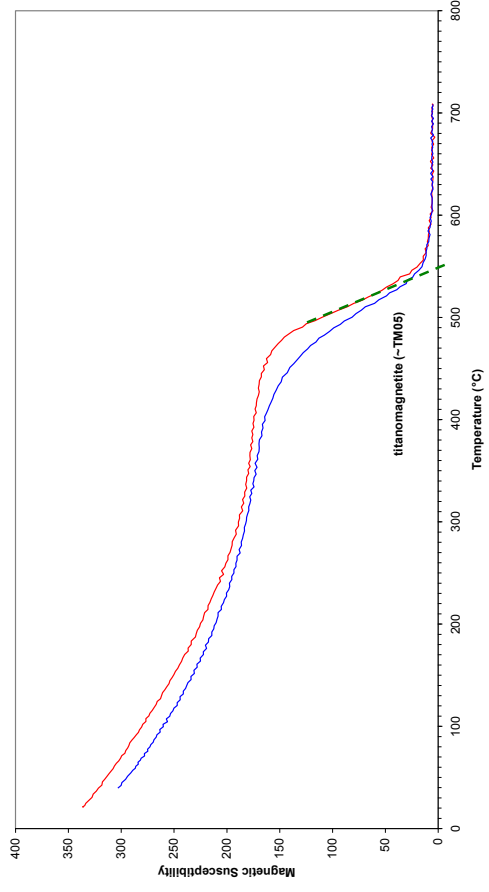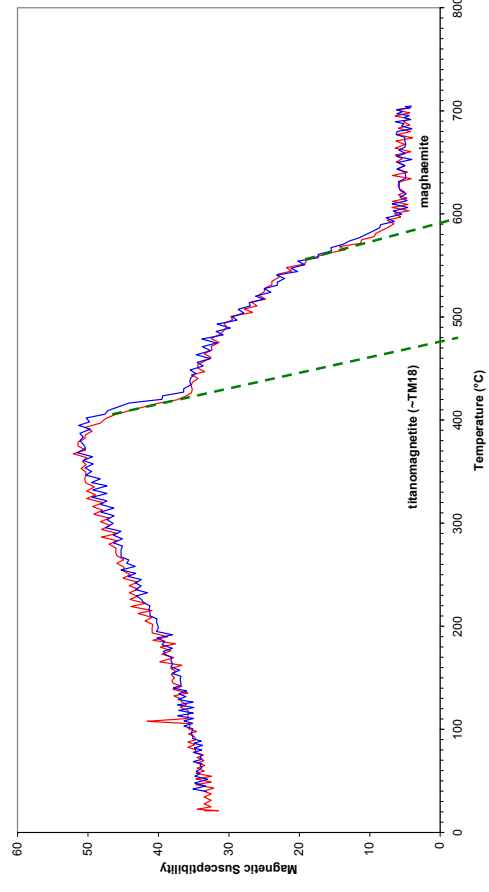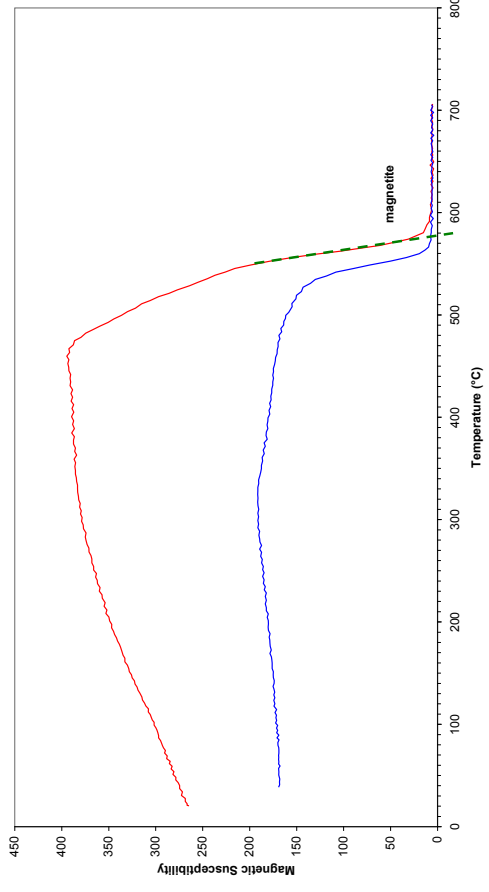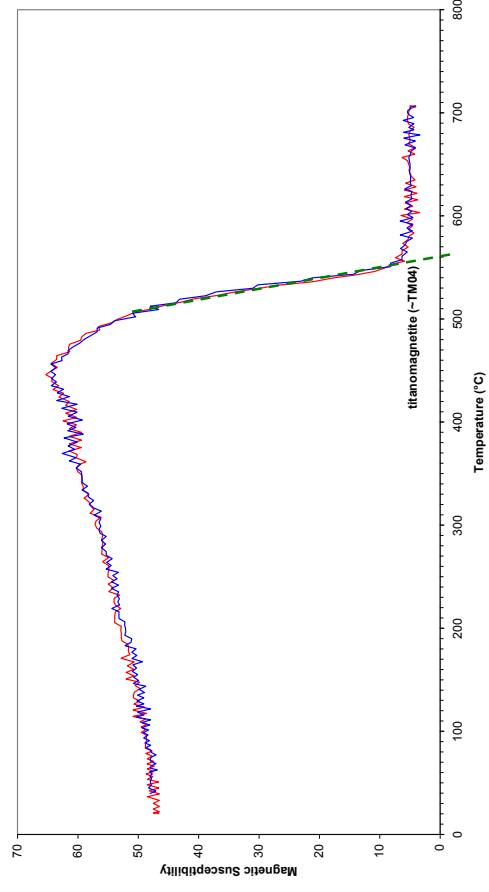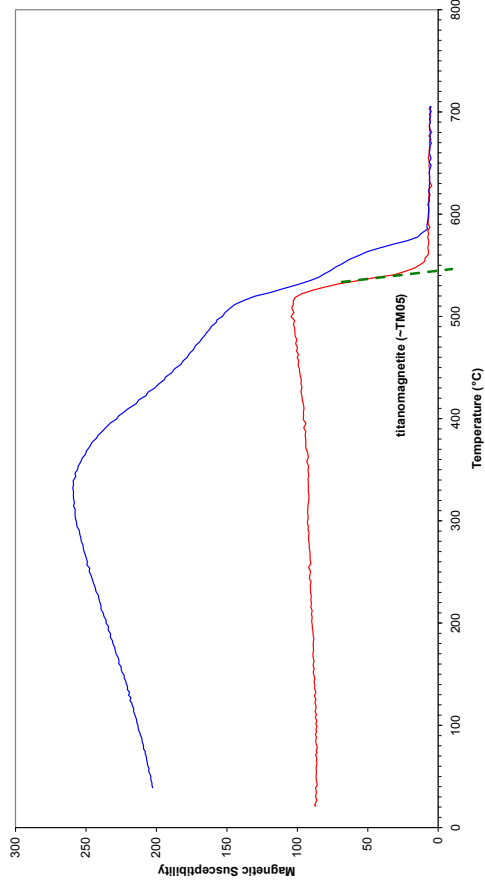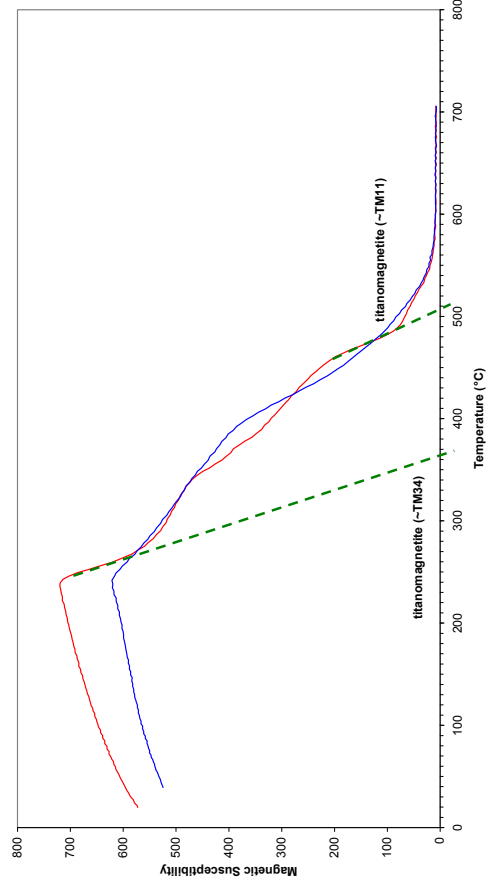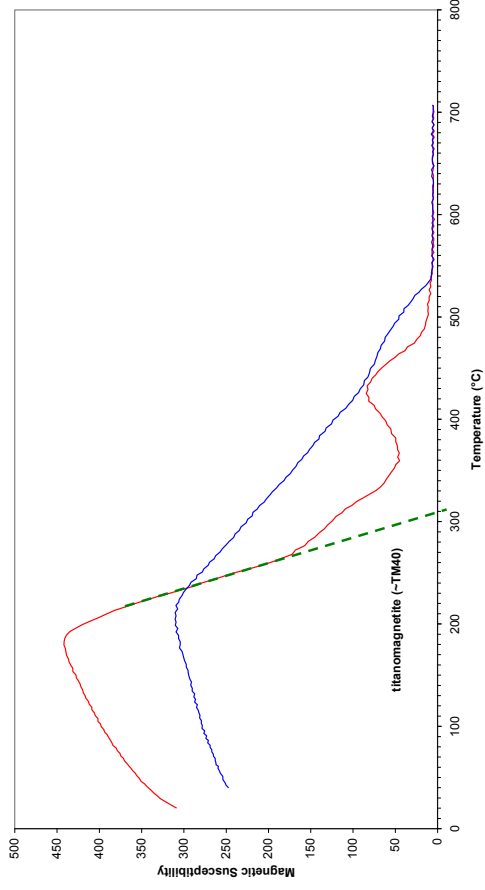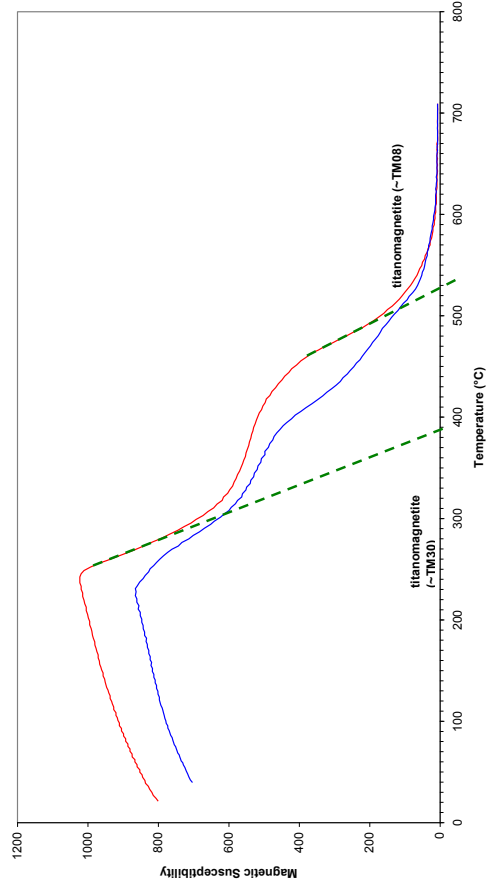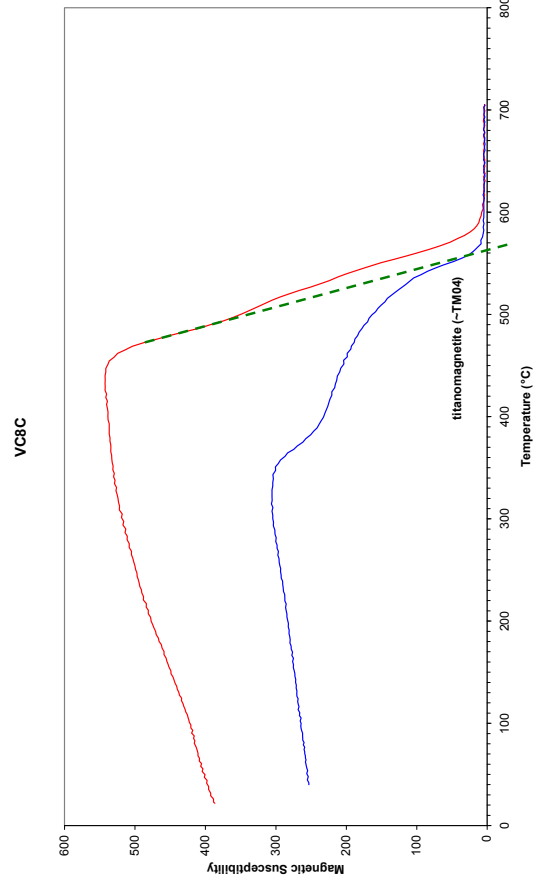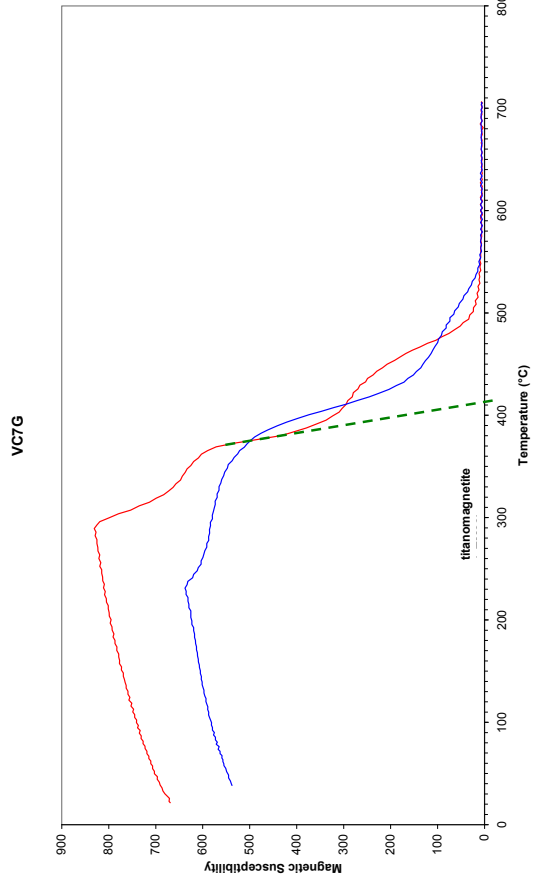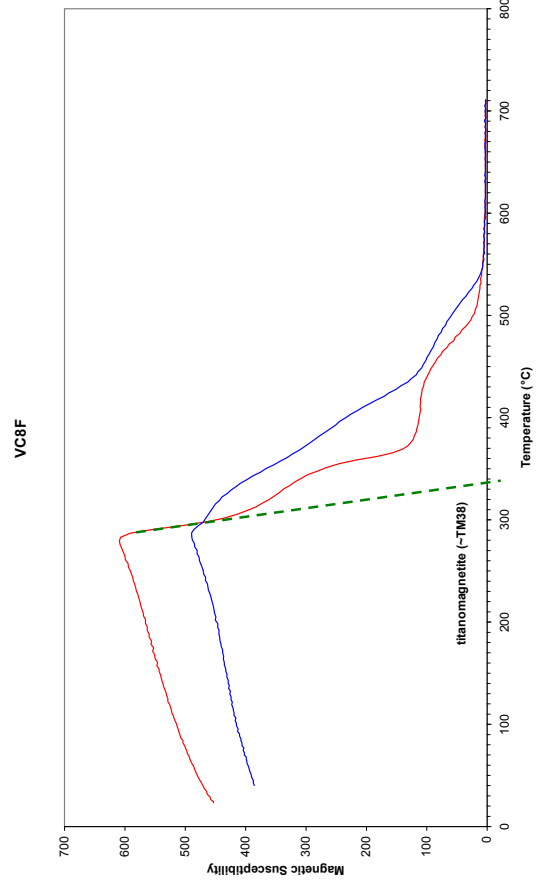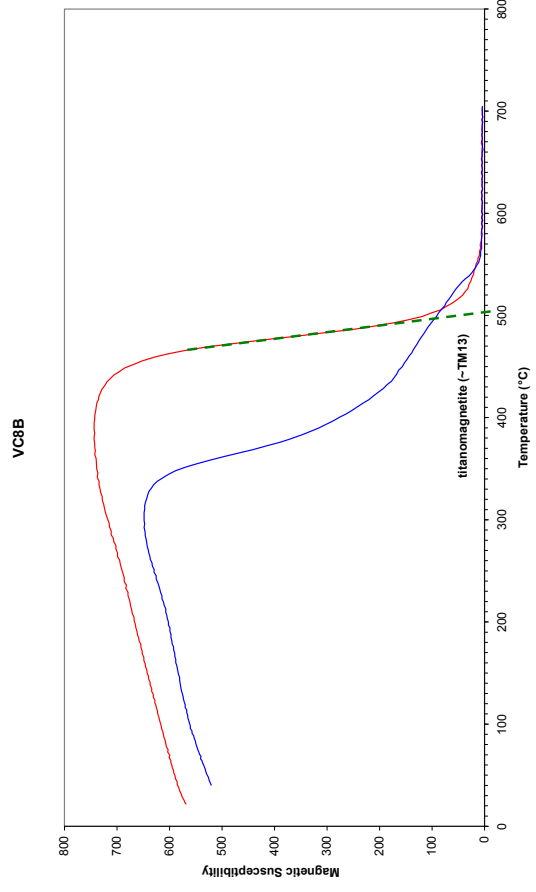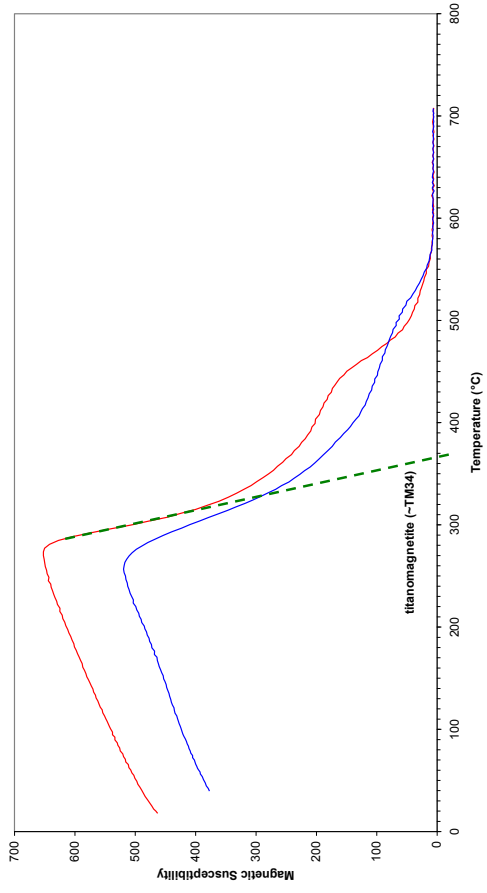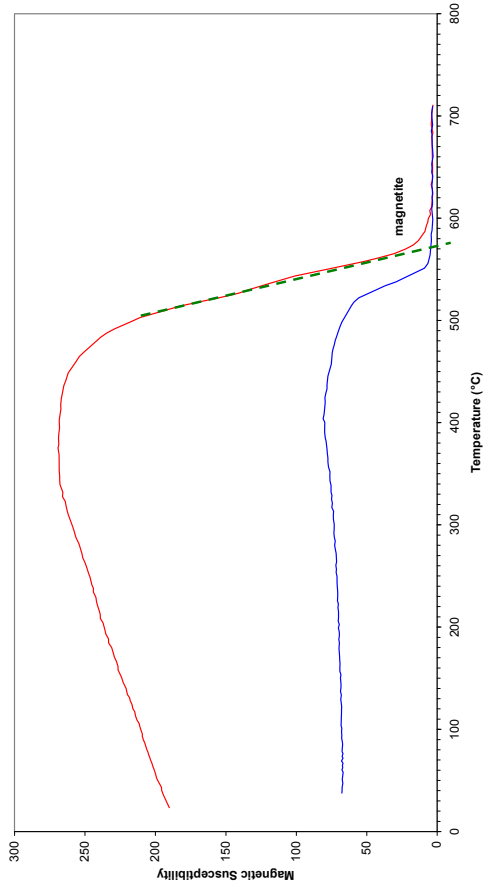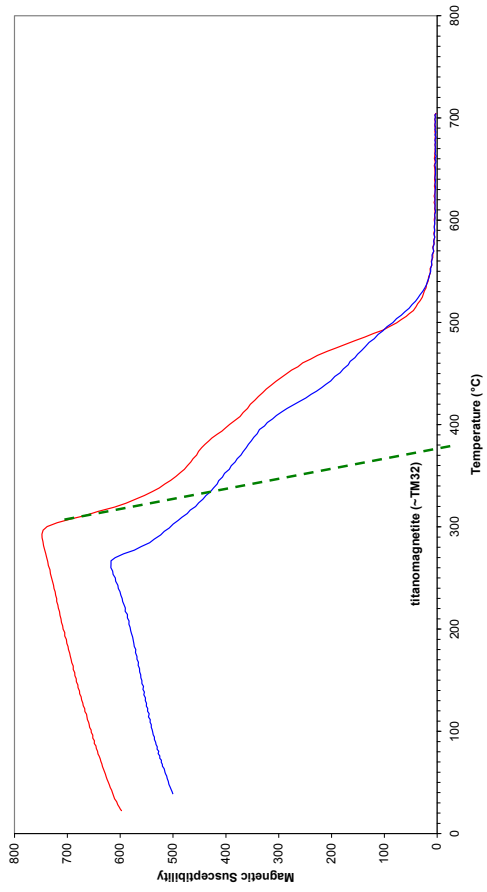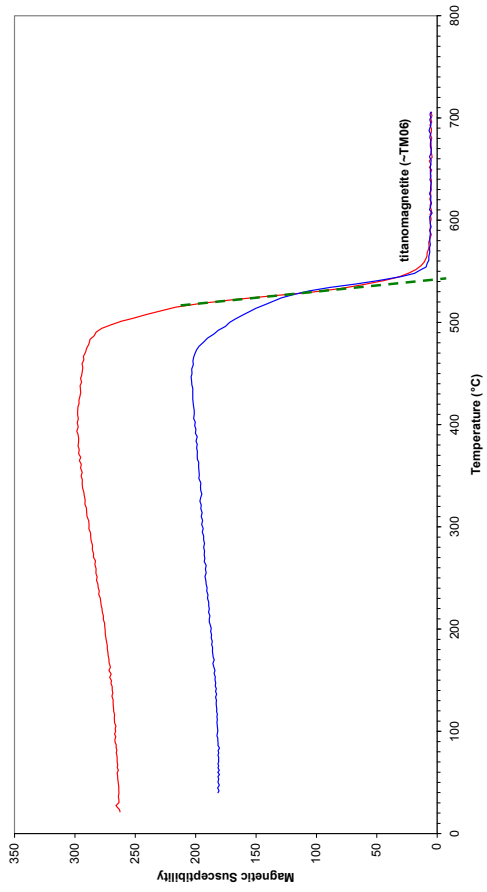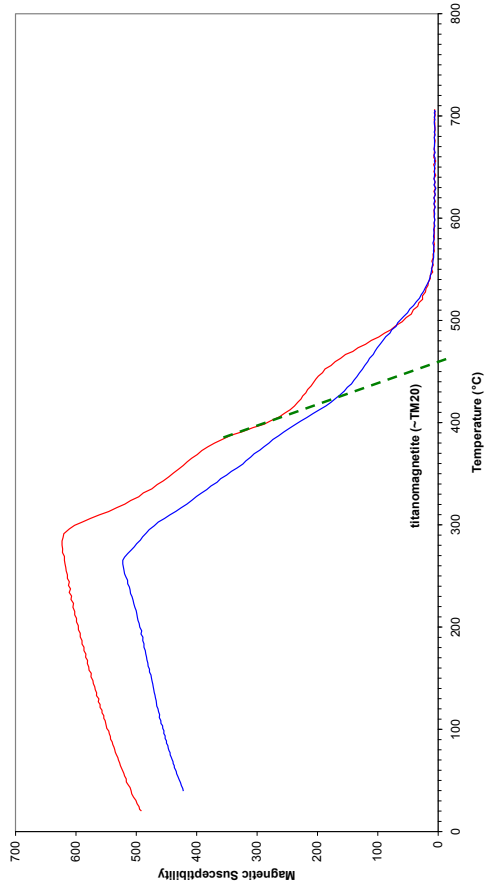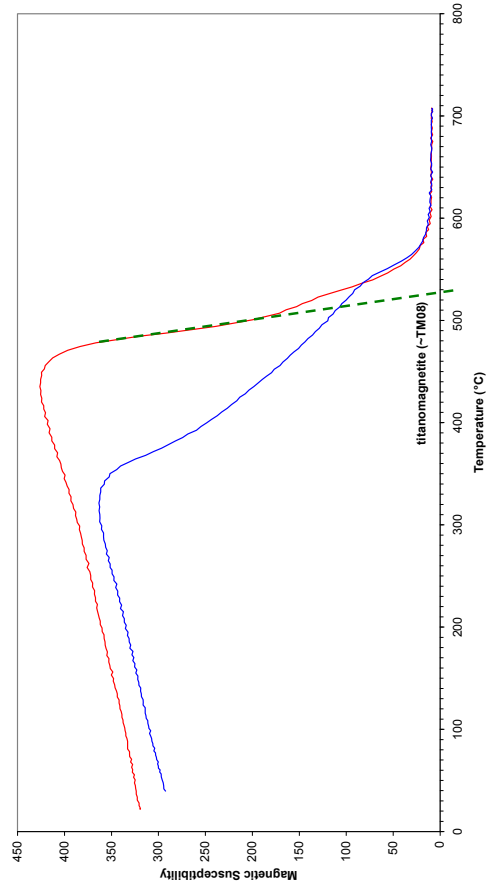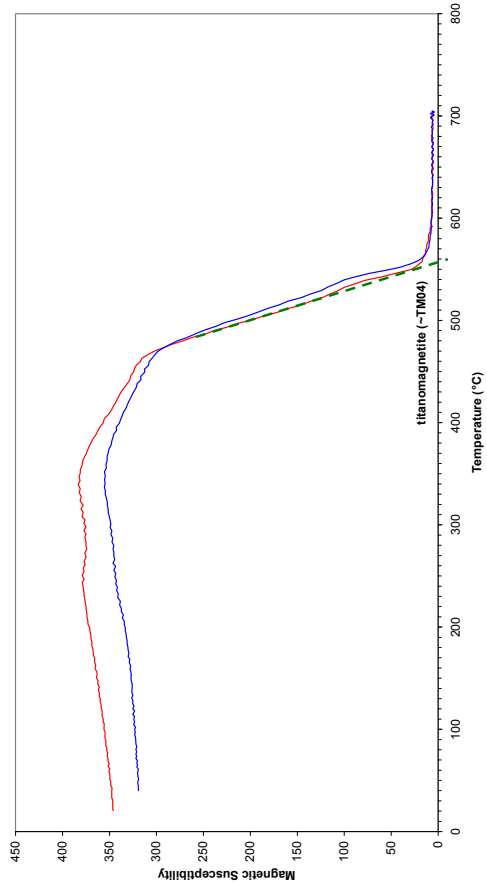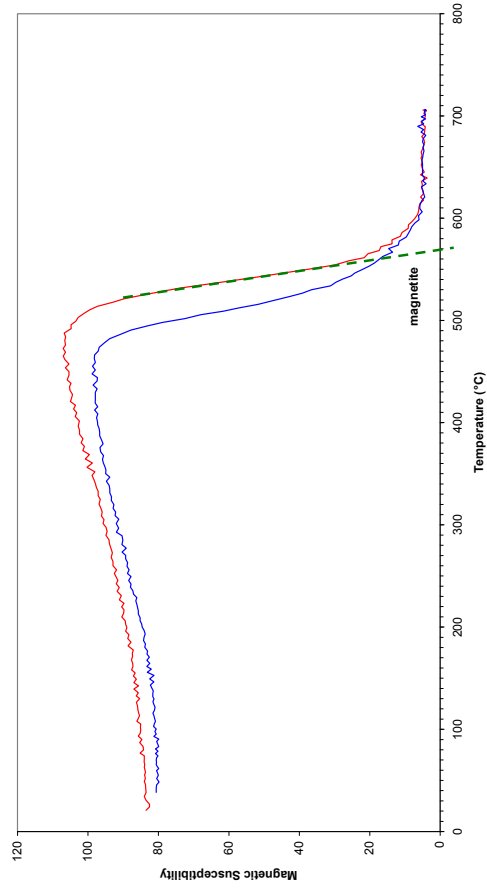
APPENDIX E – REMAINING IRM RESULTS

VC4B3B

Intensity (mA/m)

Applied field (mT)

VC4D1

Intensity (mA/m)

Applied field (mT)

VC9D3A
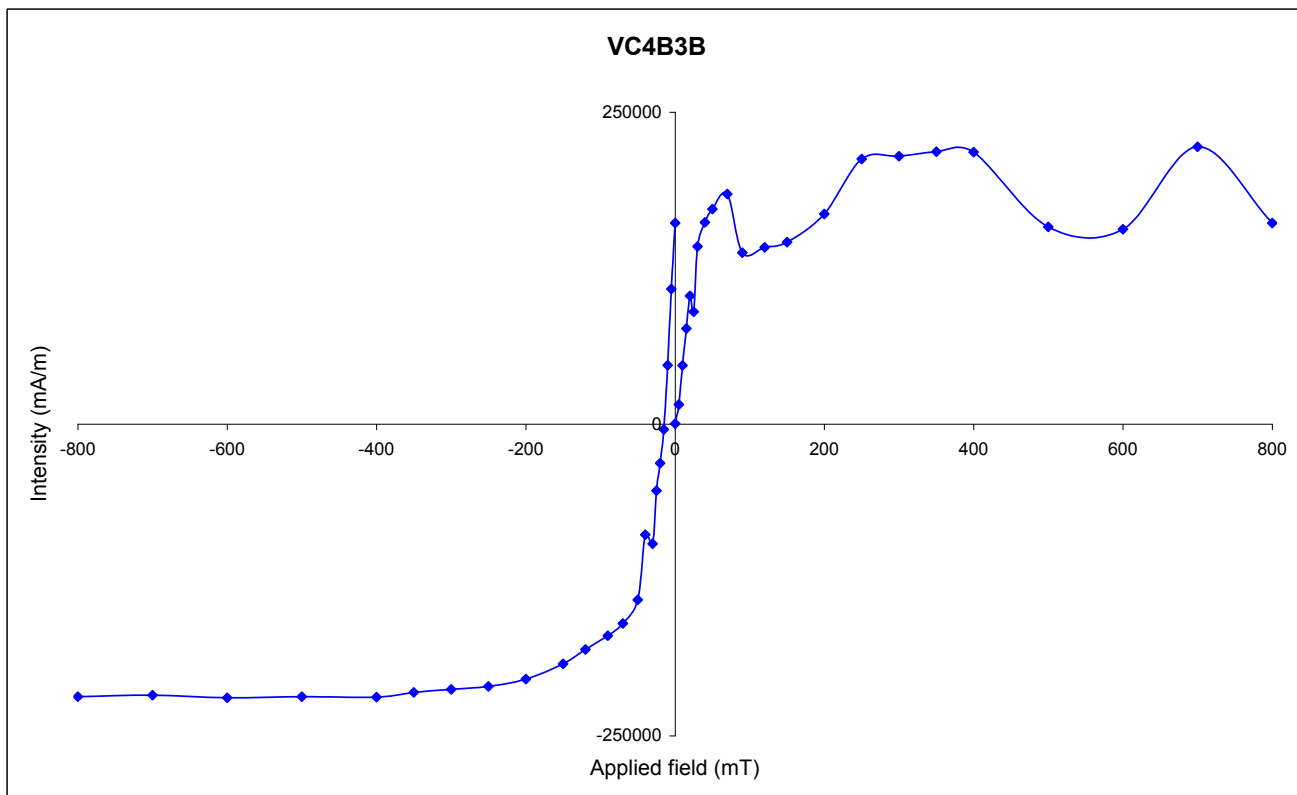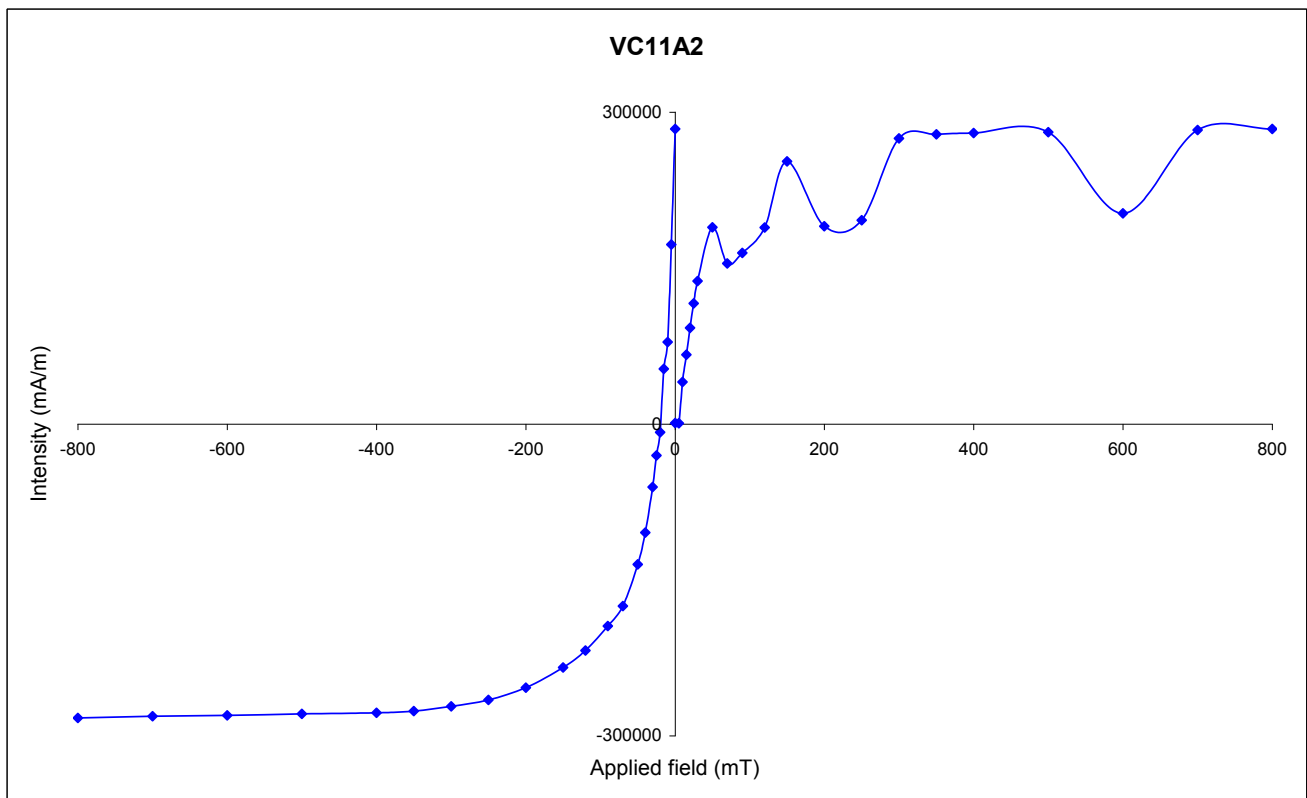
Intensity (mA/m) vs Applied field (mT)

VC11A2

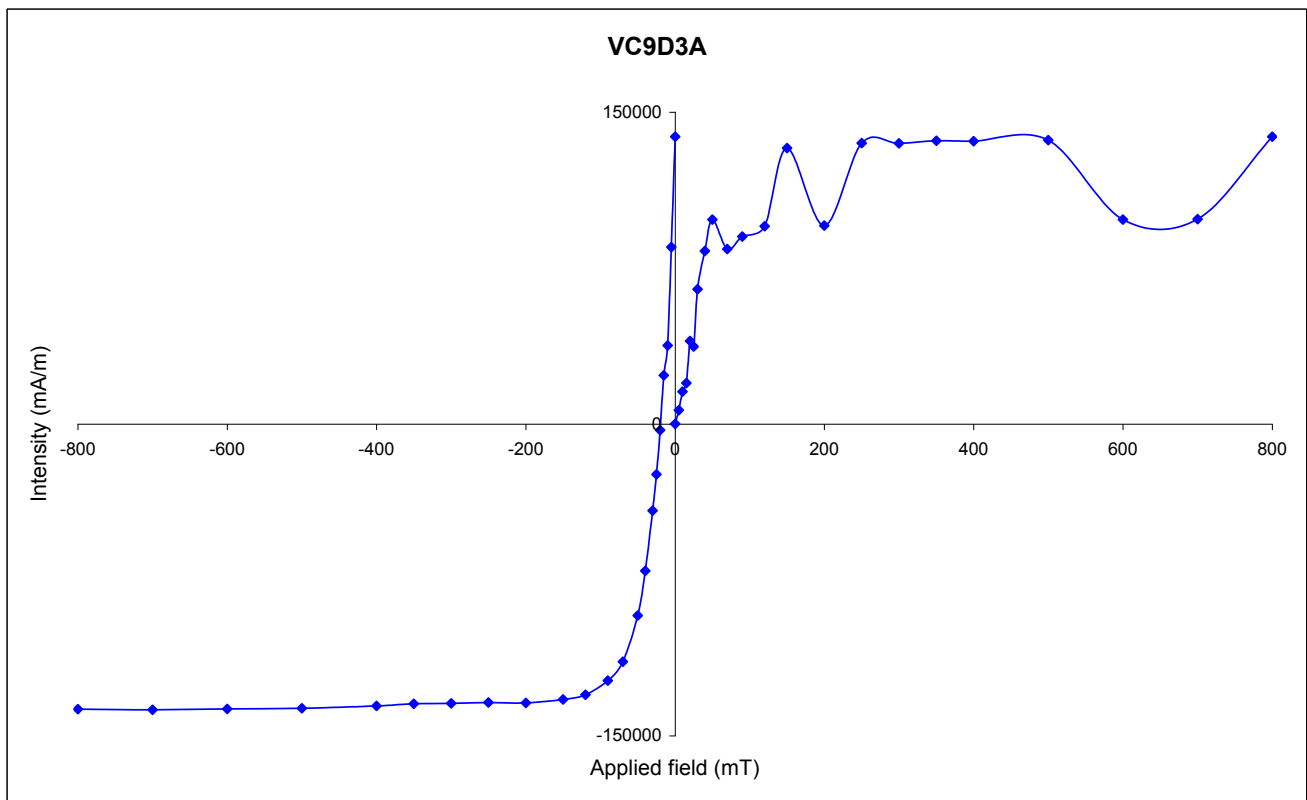Intensity (mA/m) vs Applied field (mT)
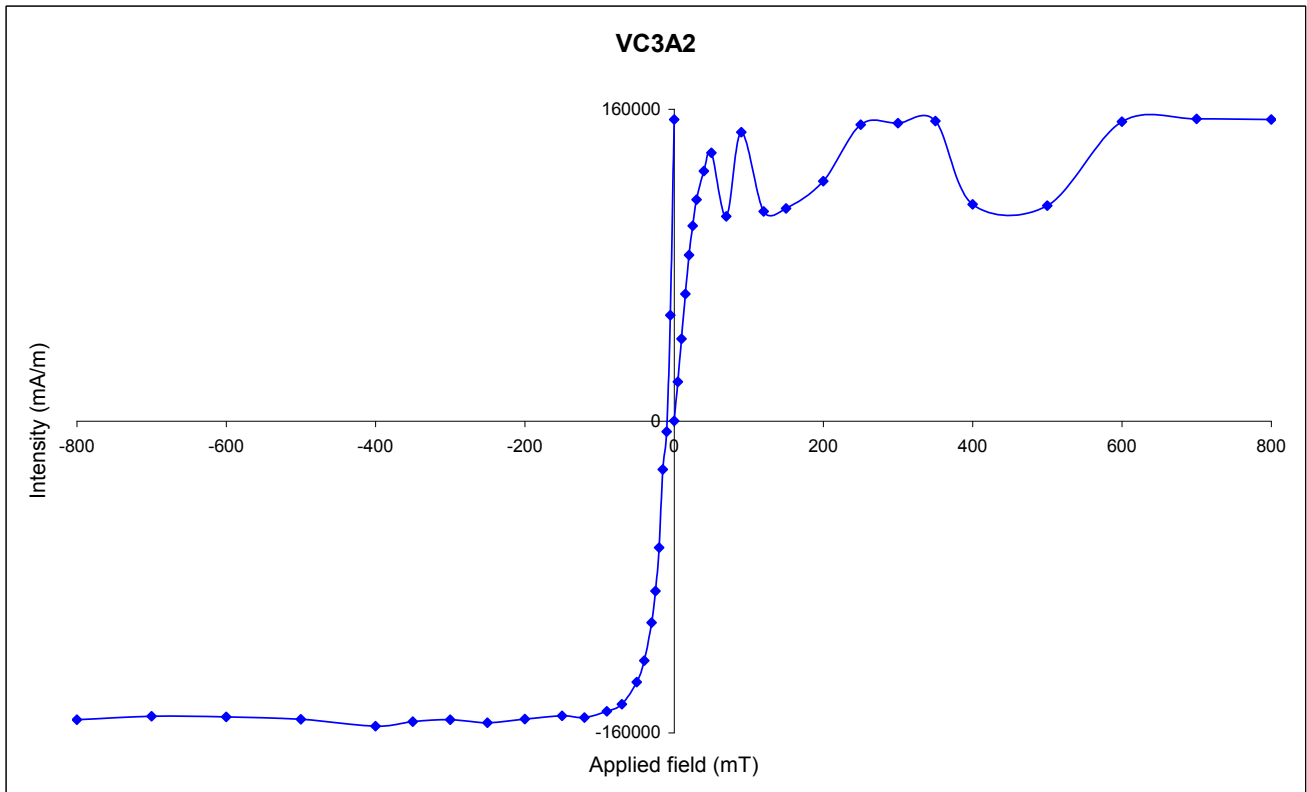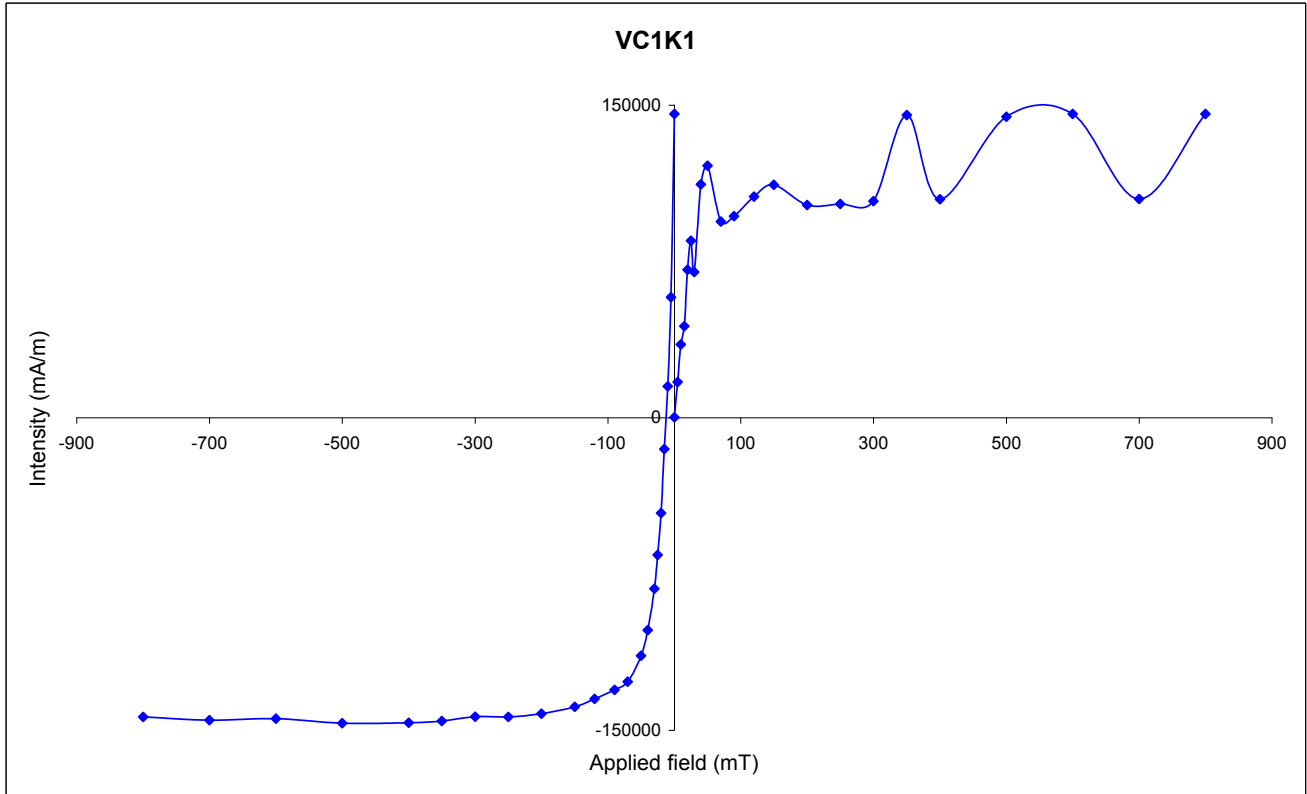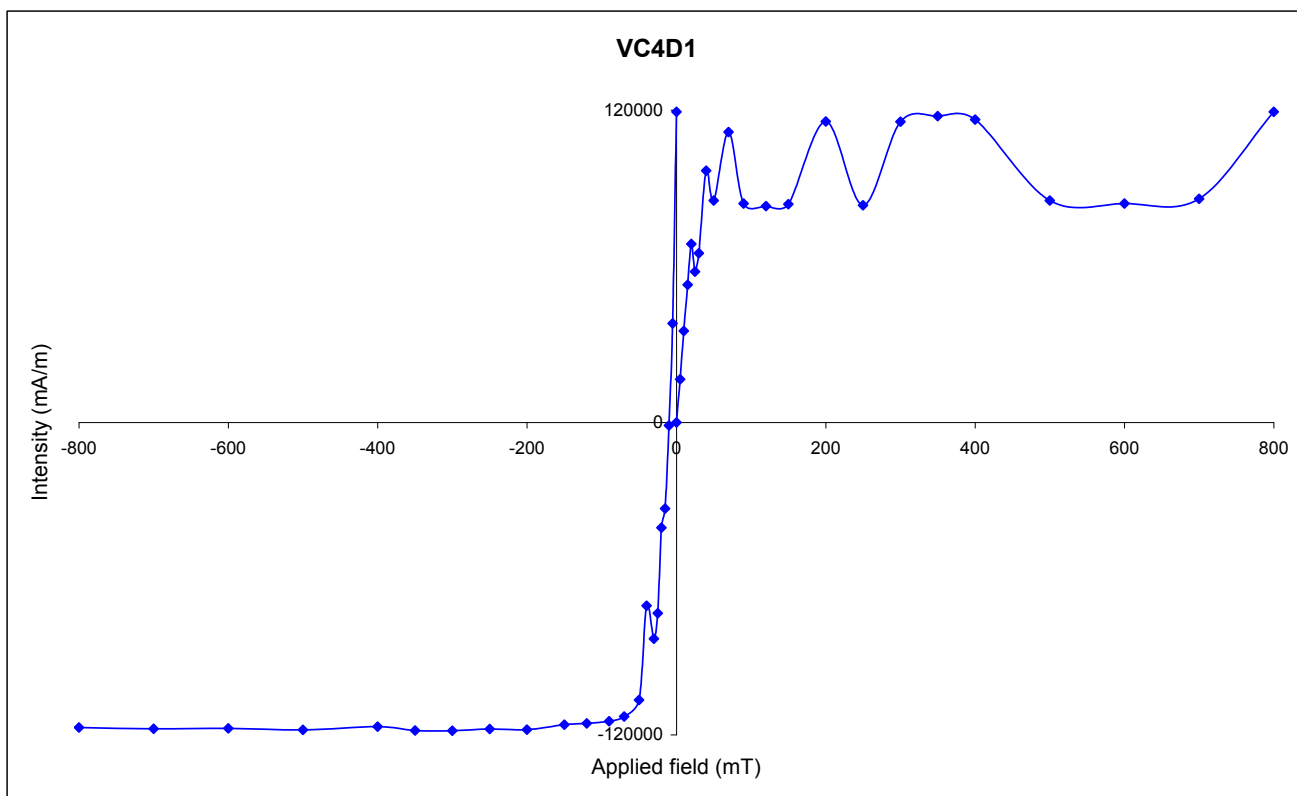
APPENDIX F – CALCULATION OF FISHER STATISTICS

This assumes a GAD model (geocentric axial dipole) for the geomagnetic field.

First, direction cosines are calculated:

$l = \cos D \cos I$

$m = \sin D \cos I$

$n = \sin I$ where D and I are the declination and the inclination.

R is the resultant vector: $R^2 = (\Sigma\, l_i)^2 + (\Sigma\, m_i)^2 + (\Sigma\, n_i)^2$

The dispersion of the data around the mean is given by two parameters: k (measure of the dispersion of the vector directions) and α_{95} (the semi-angle of the cone of 95% confidence about the mean).

$$k = \frac{(N-1)}{(N-R)}$$

$$\alpha_{95} = 1 - \frac{N-R}{R}\,[(20)^{(1/N-1)} - 1]$$

                                                 N is the number of samples.

For large sample sets k generally reaches a plateau, and its rate of increase slows dramatically when N is 6 or more. α_{95} is more dependent on N and it is possible to get an artificially low estimate of scatter by increasing the number of samples.

The randomness in a group of directional data shows how well those directions are grouped. Watson (1956) developed a test for randomness. Randomly oriented vectors will have small values of **R**, and with an increased clustering of directions **R** will approach N. Watson defined a parameter **R₀** as an estimate for randomness:

$$R_0 = \sqrt{7.815\, \frac{N}{3}}$$

If **R** is greater than **R₀** the hypothesis of randomness can be rejected at the appropriate confidence level.